UNIVERSITY OF OKLAHOMA

GRADUATE COLLEGE

CHARACTERIZATION AND ORIGIN OF FRACTURE PATTERNS IN THE WOODFORD SHALE IN SOUTHEASTERN OKLAHOMA FOR APPLICATION TO EXPLORATION AND DEVELOPMENT

A THESIS

SUBMITTED TO THE GRADUATE FACULTY

In partial fulfillment of the requirements for the

Degree of

MASTER OF SCIENCE

By

ROMINA MARISA PORTAS ARROYAL
Norman, Oklahoma
2009

Downloaded from SHAREOK. Persistent Handle URL: https://hdl.handle.net/11244/323459
UNIVERSITY OF OKLAHOMA LIBRARIES

1
HESIS
'OR
op.2

CHARACTERIZATION AND ORIGIN OF FRACTURE PATTERNS IN THE WOODFORD SHALE IN SOUTHEASTERN OKLAHOMA FOR APPLICATION TO EXPLORATION AND DEVELOPMENT

A THESIS APPROVED FOR THE
CONOCOPHILLIPS SCHOOL OF GEOLOGY AND GEOPHYSICS

BY



© Copyright by ROMINA MARISA PORTAS ARROYAL 2009
All Rights Reserved.

ACKNOWLEDGEMENTS

I would like to thank my dear and special advisor Dr. Roger M. Slatt for all his support from the beginning when I was an exchange student and all throughout my Master's, for always believing in me and providing me with great experiences and opportunities, including the fact that I wanted to work on a thesis with field experience. To my committee, Dr. Kurt J. Marfurt and Dr. James M. Forgotson, for giving me advise and dedicate time into this research.

Acknowledgements to Devon Energy for proving the funds to make this thesis. To the Wyche Shale Pit owners. To Dr. Tim Wawrzyniec from UNM, who acquired and processed the LIDAR data. To Erik Kitt and the company 3D Geophysics, who acquired and processed the seismic data. To Dr. Bob Davis and Schlumberger for providing log suites in the well. To the creators of the software packages Stereonet v1.2.0, Splift-FX v2.0, Polyworks, Petrel, and Hampson-Russell.

Thanks to Nichole Bucker and Ashley Merritt who helped me in those warm days in the field. Thanks to the school staff: Donna, Niki, Nancy, Teresa and Addriane. Thanks to Dr. Pigott, for passing on all his knowledge.

To my good, old friends who will always be present even though we do not see each other very often: Mane, Giu, Carlos, Juan, Andre. To all my friends here at the school: Xavier Refunjol, Byron, Santacruz, Aliya, Inyene, Russian, Grant, and Fabricio.

Thanks to my family for always being there for me: my brothers Alejandro and Xavier; my parents Luis and Marissa, the most dedicated, interesting and educated people I know. Thank you God for taking care of me in different ways and bringing all these wonderful people into my life.

TABLE OF CONTENT

ACKNOWLEDGEMENTS.....iv

TABLE OF CONTENT.....v

LIST OF FIGURES.....vii

LIST OF TABLES.....xiv

LIST OF APPENDICES.....xiv

ABSTRACT.....xv

1. INTRODUCTION.....1

1.1 Objectives.....1

1.2 Area of Study.....2

1.3 Geology of the Study Area.....2

1.3.1 Stratigraphic Summary.....2

1.3.2 Structural History.....7

1.4 Fractures.....13

2. METHODOLOGY.....17

2.1 Available Data.....17

2.1.1 Outcrop Study.....17

2.1.1.1 Global Positioning System (GPS) and Photomosaics of quarry walls.....17

2.1.1.3 Fracture measurements on quarry floor.....21

2.1.2 Behind-outcrop Coring and Logging.....21

2.1.3 2D Seismic Lines.....24

2.1.4 Laser Imaging Detection and Ranging (LIDAR) data.....31

2.2 Workflow.....36

3. RESULTS.....37

3.1 Fracture measurements on quarry floor.....37

3.2 Laser Imaging Detection and Ranging (LIDAR) data.....40

3.3 Behind-outcrop Coring and Logging.....50

3.4 2D Seismic Lines.....54

4. DISCUSSION.....59

5. CONCLUSIONS.....69

6. RECOMMENDATIONS.....71

REFERENCES.....74

APPENDICES.....81

LIST OF FIGURES

Figure 1. Location of Wyche Shale Pit, identifying the different walls, the location of the Wyche #1 well, and the 2D seismic lines (white lines). 3

Figure 2. (A) Photo of the west wall, (B) Photo of the north wall, showing the Woodford Shale exposure. Red dashed lines in A outline fractures. Approximate height 16m (50ft). 4

Figure 3. Arkoma Basin Stratigraphic column (modified from Perry, 1995). 6

Figure 4. Woodford Shale members identified by log signatures (Cardott, 2007). 7

Figure 5. Location of the study area (identified with a black dot) within the major geologic provinces of Oklahoma (modified from Northcutt, 1995). 9

Figure 6. Map of the Arbuckle Mountains with principal structural features. Faults are shown by thick lines (thrust faults with sawteeth), folds (anticlines and synclines) are shown by thin lines. The location of study area is between the Ahloso Fault (normal fault with hanging wall to the north, striking east-west), and the Stonewall Fault (normal fault with hanging wall to the southeast, striking southwest-northeast) (modified from Suneson, 1997). 10

Figure 7. Geologic map of the Arbuckle Mountains, with red line showing the approximate location and trend of the cross-section in Figure 8 (modified from Suneson, 1997). 10

Figure 8. Structural development of the Southern Oklahoma aulacogen. (A) Middle Cambrian extension, faulting, rifting, and filling of the rift with volcanic rocks, (B) Late Cambrian to Early Devonian subsidence and accumulation of mostly marine limestone and lesser sandstone and shale, (C) Continued subsidence in Late Devonian to Late Mississippian and deposition of mostly marine shale and minor sandstone and limestone, and (D) Folding, faulting, and formation of the Arbuckle mountains (modified from Suneson, 1997). 11

Figure 9. (A) Structure map of the Hunton Group. (B) Isopach map of the Hunton Group in eastern Oklahoma, with Pontotoc County highlighted with a black outline and study area with a red square. Structure and isopach contours are in ft drawn on top of Hunton Group. Yellow represents zero isopach of Hunton, and dark blue represents outcrops of this group. 1=Ahloso fault, 2=Stonewall fault, and 3=Franks fault zone (modified from Amsden, 1980). 12

Figure 10. Sketch blocks presenting the models for the different types of fractures: extensional and shear (divided into sliding and tearing) (modified from Van der Pluijm, 2003). 14

Figure 11. Photo from the Wyche Shale Pit Wall #4 showing fracture planes with approximately west-east strike, possibly representing extensional fractures. 15

Figure 12. Relationship between fracture orientation and the orientation of the maximum and minimum principal stresses. The fracture is represented in cyan, while the faults are in red (modified from Lacazette, 2000). 15

Figure 13. Relationship between fracture orientation and regional/local principal stresses. (A) Normal faulting stress regime (B) Reverse faulting stress regime. The fractures are represented in cyan, while the faults are in red. (Lacazette, 2000). 16

Figure 14. (A) Sketch block representing patterns for systematic and nonsystematic fractures (modified from Van der Pluijm, 2003). 16

Figure 15. (A). Major structural elements around Wyche Shale Pit (modified from Northcutt, 1995), with location of cross-section. (B). Sketch cross-section showing structural position of the outcrop (not to scale). 18

Figure 16. Wyche Shale Pit map created with a measuring tape and hand-held GPS receptor. 19

Figure 17. Panoramic view of the quarry, showing the location of the well, walls and benches. 19

Figure 18. (A) Plan view of the Wyche Shale Pit, with wall #3 highlighted in orange and seismic lines in cyan. (B) Photomosaic of wall #3 at Wyche Shale Pit. 20

Figure 19. Orientation of scan lines measured in the quarry floor, lower bench. 22

Figure 20. Sonic (ft/s), Gamma Ray (API), Density (g/cc), Neutron porosity (%), Borehole Image log (static and dynamic) from the Wyche #1 well. The contacts between the Upper and Middle Woodford, as well as the unconformity between the Woodford-Hunton are identified. Notice the different log responses as well as the changes in color in the borehole image log (darker color represents most conductive material, lighter color represents most resistive material) 23

Figure 21. Location of 2D Seismic lines acquired in the Wyche Shale Pit 24

Figure 22. Panoramic view of the quarry, showing the location of the 2D Seismic Lines. 25

Figure 23. (A) 48-channel Bison Series 9000 Digital Instantaneous Floating Point Signal Stacking Seismograph, and (B) Source, automatic sledge hammer striking an aluminum plate. 25

Figure 24. Seismic traces are the convolution of the reflectivity spectrum with the source wavelet, plus noise (modified from Partyka, 1999 and Negrey, 2005). 26

Figure 25. Correlation between seismic data in time and well log data in depth, with a correlation coefficient of 0.97. A time-depth curve was generated, using a wavelet extracted from the well with constant phase. 28

Figure 26. Frequency spectrum of the five seismic lines shot at Wyche Shale Pit..... 29

Figure 27. Seismic Line #5. (A) Before structural smoothing, (B) After structural smoothing. The Upper-Middle Woodford contact is highlighted in green, Woodford-Hunton unconformity in yellow, and a interesting interval below the Hunton in cyan, as well as the position of Wyche #1 well..... 30

Figure 28. Opentech Inc Ilris 3D Terrestrial Lidar Scanner (TLS). Image courtesy of Tim Wawrzyniec, UNM..... 32

Figure 29. View of the Wyche Shale Pit during the Lidar acquisition. Notice the Terrestrial Lidar Scanner..... 32

Figure 30. Wyche Shale Pit plan view created with the lidar data point clouds. Red dots represent the location of the different stations used during the data acquisition. The red box delimits the area shown in Figure 31..... 34

Figure 31. (A) Lateral view of Wall #4 pointing the location of "B" and showing the trend of the fracture planes, (B) Photo of east-west trending Wall #4. (C) View of point cloud from the same areas as "A" loaded into the first software, (D) Mesh of the rock surface from the point cloud generated automatically by a software, (E) Fracture patches identified by software (red outlines are areas within a patch that are not part of the planar patch outlined) (F) Point cloud loaded into the second software that allows fracture planes to be picked manually. 35

Figure 32. Workflow followed to complete the research. 36

Figure 33. Scan lines #1 and 2 with Group 1 fractures being systematic highlighted in red, and Group 2 fractures being not systematic highlighted in blue. 37

Figure 34. Fractures planes measured on Scan Line #1 and 2 (n=357), with group numbers. 38

Figure 35. Histogram of fracture plane strikes measured on both scan lines (n=357). Observe that the majority of the fractures have a strike between 76-90° (ENE orientation), followed by fractures with strikes between 31-45° (NE direction), and fractures with strikes between 106-120° (NW direction). 38

Figure 36. Fracture planes in Scan Lines divided in classes: (A) Fractures with no aperture (n=214), (B) Fractures with open aperture (n=72), and (C) Fractures with filled aperture (n=71). Group numbers are shown. 39

Figure 37. Histogram of fracture plane strikes measured on both scan lines. Blue represents the fractures with no aperture (n= 214) mostly in Group 2 (n=69). Red represents the fractures with open aperture (n=72) mostly in Group 1 (n=56). Green represents the fractures with filled apertures (n=71) mostly in Group 1 (n=37). 40

Figure 38. Fracture planes picked manually (n=131). 41

Figure 39. Histogram of fracture plane strikes picked manually (n=131). The majority of the fractures are in Group 1. 41

Figure 40. Histogram of fracture plane dips picked manually (n=131). Out of the 131 fracture planes, 104 have a near vertical dip. 42

Figure 41. Image of the LIDAR data on Wall #3, with fracture planes highlighted with red lines. Most of the fractures planes interpreted have a vertical dip and a west-east strike, like Group #1. On 20m (65ft) horizontal distance, 15 fracture planes were manually interpreted. Average distance between fractures is 1.5m (4ft). 43

Figure 42. Image of the LIDAR data on Wall #2 and 1, with fracture planes highlighted with red lines. Most of the fractures interpreted have a vertical dip and a west-east strike, like Group #1. On 14m (45ft) horizontal distance, 11 fracture planes were manually interpreted. Average distance between fractures is 1.5m (4ft). 44

Figure 43. Image of the LIDAR data on Wall #4, with fracture planes highlighted with red planes. Most of the fractures interpreted have a vertical dip and a west-east strike, like Group #1. On 14m (45ft) horizontal distance, 11 fracture planes were manually interpreted. For further understanding refer to figure 31. 45

Figure 44. Histogram of fracture plane strikes picked automatically by a software (n=5008). Observe the difficulty to discriminate a dominant strike direction. 47

Figure 45. Histogram of fracture dips picked automatically by a software (n=5008). The greatest amounts of planes have dips between 31 to 70°. 47

Figure 46. Fracture planes picked automatically by a software with dips between 76-90° (n=280). 48

Figure 47. Histogram of fracture plane strikes picked automatically by a software, with dips between 70-90° (n=280). Most of the fracture planes are in Group 1 (strike between 76-90°), followed by Group 2 (strikes between 31-45°). 48

Figure 48. Fracture strikes picked automatically using interpretation software with dips between 70-90° and roughness between 0.8-1 (n=93). 49

Figure 49. Histogram of fracture planes strikes picked automatically by a software with dips between 70-90° and roughness between 0.8-1 (n=93). Most of the fracture planes strike between 76-90, followed by 31-45. 49

Figure 50. Fractures measured in the borehole image log. (A) Poles representing the fractures strike and dip magnitudes, (B) Fractures strike plotted on a rose diagram (n=14). All fractures appeared to be healed, and none were planar features cutting through the entire wellbore. The mean strike orientation is N50°E-S50°W, with dip magnitudes ranging between 51°-99° (average dip of 77.5° at 140° azimuth) (Buckner, 2009). 50

Figure 51. Features identified in the core and borehole image log, (A) Phosphatic nodules are bright ovals in the borehole image log, (B) Fractures in core and borehole image log (notice how the fractures are healed in the core) (core images modified from Buckner, 2009). 51

Figure 52. Features identified in the core and borehole image log, (C) Pyrite is represented as dark circles with bright halos in the log, and (D) Unconformity between Woodford-Hunton (darker color represents most conductive material, lighter color represents most resistive material) (core images modified from Buckner, 2009). 52

Figure 53. Fracture frequency plot. Blue bars represent fractures in the Borehole image log and red bars represent fractures in the core. The majority of the fractures are in the Upper Woodford member. Data obtained from Buckner, 2009. 53

Figure 54. (A) Line #5 and (B) Line #4. The Upper-Middle Woodford contact is highlighted in green, and the Woodford-Hunton unconformity in yellow, as well as different faults and the position of well Wyche #1. 55

Figure 55. Lateral view of the 2D seismic lines shot at the Wyche Shale Pit, with horizons and faults interpreted. The Upper-Middle Woodford contact is highlighted in green, and the Woodford-Hunton unconformity in yellow, as well as different faults and the position of well Wyche #1. 56

Figure 56. 3D view of the 2D seismic lines shot at the Wyche Shale Pit, with surfaces and faults interpreted. (1) Upper-Middle Woodford contact, (2) Woodford-Hunton unconformity, and (3) Possible contact between the Hunton Group and the Sylvan Shale. 57

Figure 57. Isochron maps for the Upper-Middle Woodford Shale Member contact and Woodford-Hunton unconformity with position of 2D seismic lines, well, and faults that cut through them. Map units are in ms. Contours are every 2ms. Keep in mind that the interpolation may not be precise due to the distance between lines. 58

Figure 58. (A). Major structural elements around Wyche Shale Pit (modified from Northcutt, 1995), with location of cross-section. (B). Sketch cross-section showing structural position of the outcrop (not to scale). (C) Sketch block of Wyche Shale Pit showing systematic and nonsystematic fracture planes. 60

Figure 59. Stress direction in Pontotoc county, southeastern Oklahoma. The average maximum horizontal stress is oriented ENE-WSW, σ2 (error of up to 25°). Data obtained from Heidbach et al, 2008. 61

Figure 60. Relationship between fracture orientation and regional/local principal stresses in a normal faulting stress regime like the one present in the Wyche Shale Pit area. The fractures are represented in cyan, while the faults are in red (modified from Lacazette, 2000). 62

Figure 61. Cross-section perpendicular through the wellbore, showing breakouts, induced tensile fractures, and the maximum and minimum directions of the horizontal principal stresses in the present (modified from Lacazette, 2000). 63

Figure 62. (A) Major structural elements around Wyche Shale Pit (modified from Northcutt, 1995), with location of cross-section. (B) Sketch showing the theory for the origin of the fracturing in the area of study. (B1) Represents the area before deformation, (B2) Beginning of the formation of tensional fractures by uplift, and (B3) Continuation of uplift producing tensional collapse, red rectangle represents Wyche Shale Pit area shown in Figure C (modified from Digg, 1961). (C) Sketch cross-section showing structural position of the outcrop (not to scale). 64

Figure 63. (A) Shaded area around the joints represents a stress shadow. (B) Joints in a thin bed have narrow stress shadows, keeping them closely spaced. (C) Joints in a thick bed have wide stress shadows, keeping them widely spaced. d_m is the average spacing between joints (modified from Van der Pluijm, 2003)..... 65

Figure 64. Example of a cross-sectional diagram representing beds of lithologies with different elasticity. Dolomite (rigid layer) develops more closely spaced joints (modified from Van der Pluijm, 2003)..... 66

Figure 65. Wyche Shale Pit plan view created with the lidar data point clouds and location of 2D seismic lines. Fractures interpreted on LIDAR (red) and seismic data (yellow and green) are correlated. Group 1 fractures have an average strike of N85°E.67

Figure 66. Map of the Arbuckle Mountains with principal structural features and fracture model from the Wyche Shale Pit area. Faults are shown by thick lines (thrust faults with sawteeth), folds (anticlines and synclines) are shown by thin lines. The location of study area is between the Ahloso Fault (normal fault with hanging wall to the north, striking east-west), and the Stonewall Fault (normal fault with hanging wall to the southeast, striking southwest-northeast) (modified from Suneson, 1997). 68

Figure 67. Aerial view of the area of study. Wyche Shale Pit and 2D seismic lines are located. Ryan Shale Pit was the location of study in Miller, 2006 and is west to the area of study in this thesis. The yellow square represents the possible location for a 3D seismic acquisition and the black dashed line represents the direction of drilling for a horizontal well (see Figure 68). 72

Figure 68. Borehole image log for a horizontal well drilled with a NNW-SSE direction perpendicular to the strike of fractures in group 1 and to σ2 (modified from Miller, 2006). 73

LIST OF TABLES

Table 1. Interval velocities for the different formations present in the study area..... 33

LIST OF APPENDICES

Appendix 1. GPS locations for the Wyche Shale Pit..... 82

Appendix 2. Wall #1 Panorama

Appendix 3. Wall #2 Panorama

Appendix 4. Wall #3 Panorama

Appendix 5. Wall #4 Panorama

Appendix 6. Wall #5 Panorama

Appendix 7. Scan line #1 and 2 measurements..... 84

Appendix 8. Wyche #1 Borehole Image Log..... 97

Appendix 9. Wyche #1 Core description..... 98

Appendix 10. Locations and elevations for the 2D seismic lines..... 99

Appendix 11. Number of fractures from scan lines grouped in 15° strike intervals... 109

Appendix 12. Number of fractures from scan lines grouped in 15° strike intervals and classified depending on their apertures..... 109

Appendix 13. Number of fractures picked manually using software B grouped in 15° strike intervals..... 109

Appendix 14. Number of fractures picked automatically by software A grouped in 15° strike intervals..... 110

Appendix 15. Number of fractures picked automatically by software A with dips between 76-90° grouped in 15° strike intervals..... 110

Appendix 16. Number of fractures picked automatically by software A with dips between 76-90° and roughness between 0.8-1, grouped in 15° strike intervals..... 110

ABSTRACT

The Woodford Shale is an important unconventional gas shale in Oklahoma. Production is by artifical fracturing of naturally fractured or unfractured rock. Therefore, understanding natural fracture networks in the Woodford may help in developing fracture stimulation procedure.

This thesis characterizes fractures within an exposed section of the Woodford Shale by integrating outcrop and subsurface data. The main objective of this research is to document and understand the natural fracture patterns within the Woodford Shale by integrating and calibrating fractures and strata in exposed quarry walls using laser imaging detection and ranging (LIDAR) data, 2D seismic lines, and the logs and core acquired in a well drilled behind a quarry wall.

Fracture measurements in the outcrop and LIDAR data revealed two extensional fractures set. Group 1 is a systematic fracture set with parallel orientations, regular spacing and mineral filling, having a median strike direction of N85°E. Group 2 is a nonsystematic fracture set, younger than Group 1, having a median strike direction of N45°E. There is a greater abundance of fractures in the Upper Woodford Shale because of its higher content of quartz. There is no lithology or bedding change laterally within the quarry walls, where the average fracture spacing is about 1.2m (4ft).

The 2D seismic lines imaged the Upper-Middle Woodford contact and the Woodford-Hunton unconformity surface. The faults interpreted on the seismic follow the same trend as the regional faults observed in the quarry.

The present stress field in the area of study has an ENE-WSW direction that generated fractures in Group 2, different from the paleostress that generated fractures in

Group 1. In the area of study, there was no relevant relief on the Woodford-Hunton unconformity surface that could have affected the fracture distribution in a greater way than local tectonics.

This information will be used as a baseline for improved understanding of fractures in the Woodford Shale to facilitate gas production by knowing fracture orientation and in situ stress.

1. INTRODUCTION

Shales have traditionally been considered as source rocks or seals in the petroleum system analysis because of their low permeabilities. However, in the last decade, the petroleum industry has recognized that shales can be treated as unconventional reservoirs if they contain great amounts of organic carbon and a thickness between 92-275m (300-900ft). Also, technological advances have made it viable to extract hydrocarbons from the Woodford Shale, which was considered an important source rock and not a reservoir (Schlumberger, 2005).

Open natural fractures within shale reservoirs help increase production by increasing the permeability and reducing the amount of hydraulic fracturing required to extract hydrocarbons. This thesis quantitatively characterizes fractures within an exposed section of the Woodford Shale by integrating outcrop and subsurface data. The information acquired will be used as a baseline for improved understanding of fractures in prospective subsurface areas.

1.1 Objectives

The main objective of this research is to understand the fracture patterns within the Woodford Shale by integrating and calibrating fractures and strata in exposed quarry walls using laser imaging detection and ranging (LIDAR) data, 2D seismic lines, and the logs and core acquired in a well drilled behind a quarry wall.

Some specific goals are to determine: (1) if the fractures align with the general strike of faulting in the study area; (2) if the fracture distribution is somehow affected by paleotopography on the underlying Hunton Group unconformity surface; and (3) if the fracture sets are confined to the Woodford Shale or extend into the Hunton Group.

Buckner (2009) presents a detailed analysis of the high resolution vertical facies, and lateral continuity of the Woodford shale from exposed quarry walls and behind-outcrop coring and logging that is, in part, incorporated in this thesis.

Miller (2006) presents a fracture characterization of the Woodford Shale in an outcrop next to the area of study for this research.

1.2 Area of Study

The south-central part of Oklahoma is recognized for its petroleum and natural gas resources; approximately 75,000 wells have been drilled in Pauls Valley, Fitts, Cumberland, Eola, Tatums, and Fox-Graham fields that are subsurface extensions of the Arbuckle Mountains, making this area a well studied geological province (Ham, 1973).

The area of study is located in southeastern Pontotoc County, Oklahoma, 12km (7.5mi) south of the city of Ada (Figure 1). The area is the Wyche Shale Pit, a quarry where the Woodford Shale is exposed on vertical walls as high as 16m (50ft) and three-dimensionally positioned, providing the sense as if one is standing on a fluid contact (quarry floor) in the middle of a Woodford reservoir (Figure 2).

1.3 Geology of the Study Area

1.3.1 Stratigraphic Summary

The Woodford Shale is an Upper Devonian to Lower Mississippian formation dominated by a black shale facies with some chert, siltstone, sandstone, dolostone, pyrite, and lighter colored facies (Comer, 2005). It contains Type II kerogen, deposited in marine environments. The Woodford Shale produces oil and gas in the Arkoma, Ardmore, and Anadarko Basins of Oklahoma and Texas, with thermal maturity increasing to the east (Cardott, 2005).

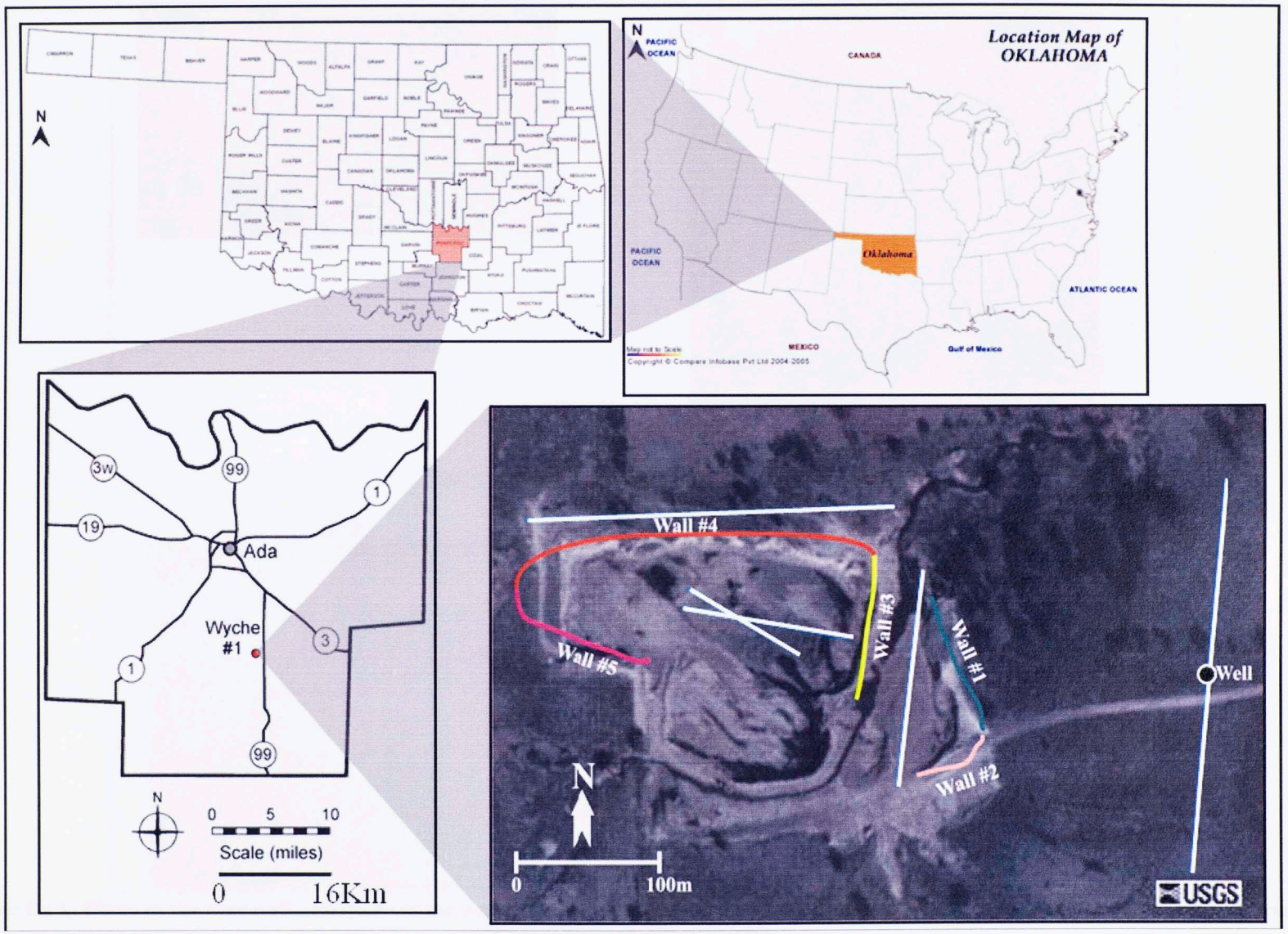

Figure 1. Location of Wyche Shale Pit, identifying the different walls, the location of the Wyche #1 well, and the 2D seismic lines (white lines).

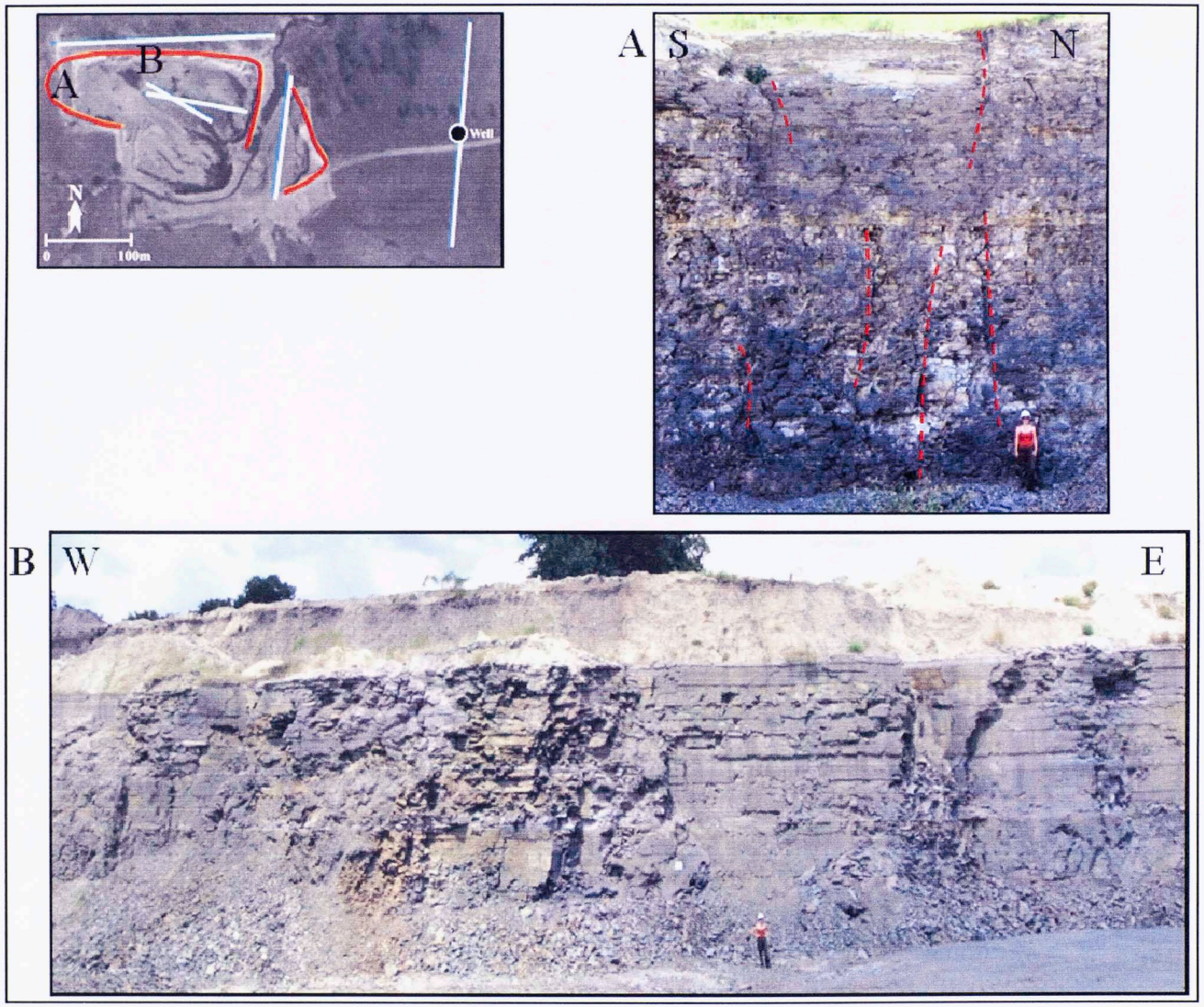

Figure 2. (A) Photo of the west wall, (B) Photo of the north wall, showing the Woodford Shale exposure. Red dashed lines in A outline fractures. Approximate height 16m (50ft).

This shale was deposited in a deep, quiet marine environment. Transgression allowed continuous deposition of the Woodford. An unconformity separates this formation from the older Hunton group (Figure 3).

According to Cardott (2007), the Woodford Shale has three informal members based on palynomorphs, geochemistry, and log signatures (Figure 4):

- The Lower Woodford Shale member has the smallest areal extent of the three members. It is commonly black, and composed of quartz silt and clay. It was deposited close to the shore during transgression.
- The Middle Woodford Shale member has the highest total organic content (TOC) and greatest areal extent of the three members. It is commonly black, radioactive, and contains Type I and II kerogen. It was deposited farther from the shore during a sea level rise.
- The Upper Woodford Shale member has the lowest TOC content of the three members. It is commonly black with Type II kerogen type II and phosphate nodules. It was deposited closer to the shore during a sea level fall.

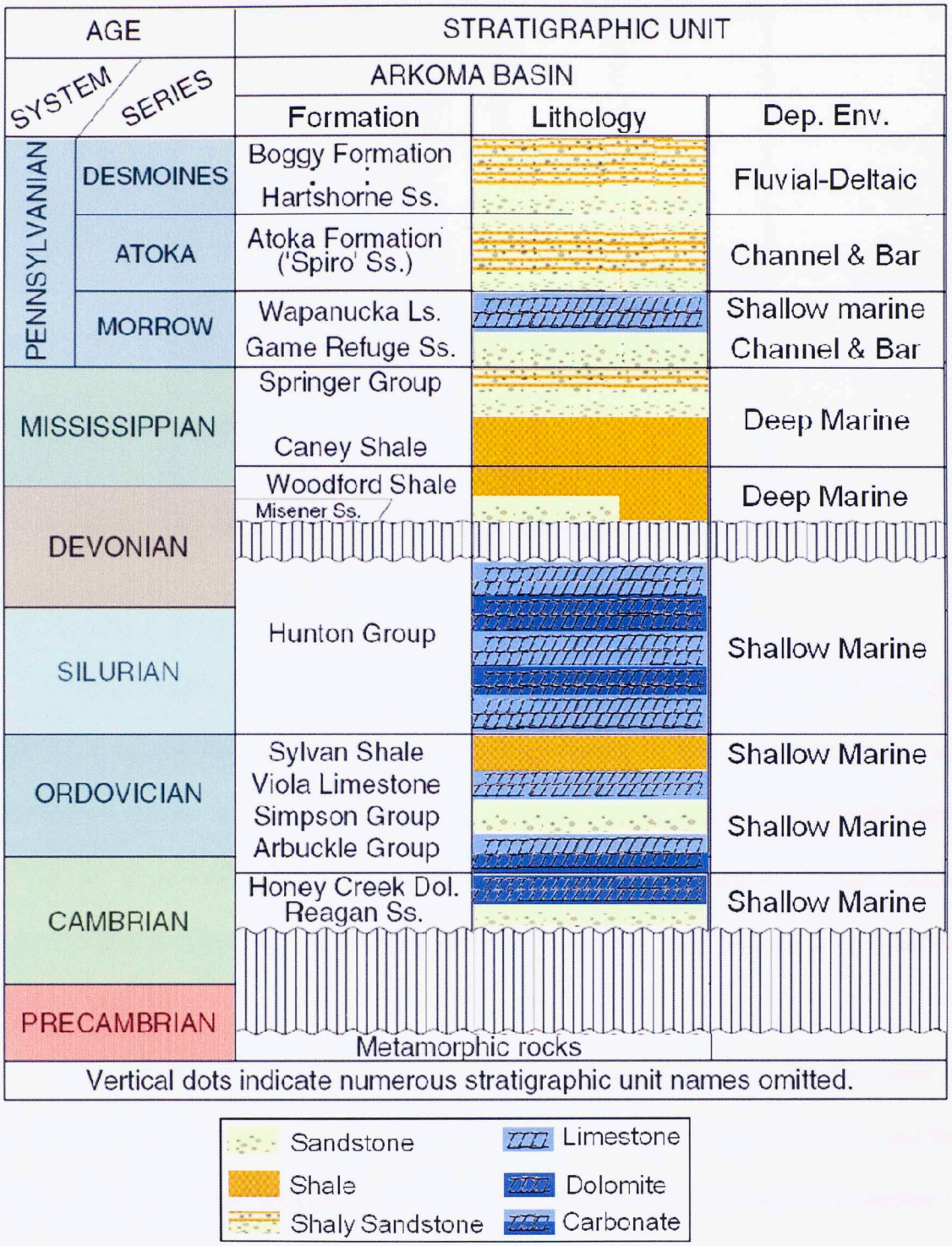

Figure 3. Arkoma Basin Stratigraphic column (modified from Perry, 1995).

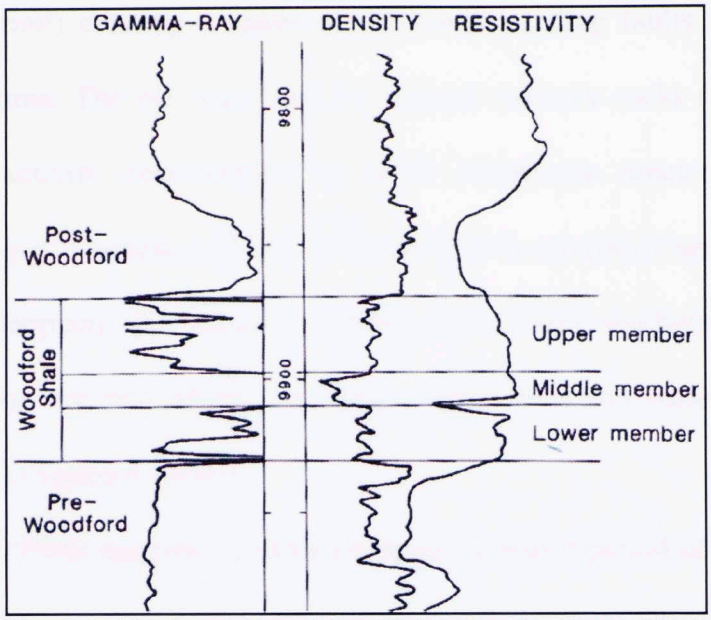

Figure 4. Woodford Shale members identified by log signatures (Cardott, 2007).

1.3.2 Structural History

The geologic map of the Arbuckle Mountains is shown in Figure 5. The Wyche Shale Pit is located east of the Arbuckle Mountains and west of the Arkoma Basin in a subprovince known as the Lawrence Uplift, bounded by the Ahloso Fault to the north and by the Stonewall Fault to the south. Surrounding subprovinces include Franks Graben, Hunton Anticline, Tishomingo-Belton Anticlines, and Wapanucka Syncline (Figure 5 and 6).

The Arkoma basin has a west-east trend. It is bounded by the Arbuckle Uplift in the west, the Cherokee Platform in the northwest, the Ozark Uplift in the north, and the Ouachita Uplift in the south (Figure 5). The geologic map of the Arbuckle Mountains is on Figure 7.

The basement or craton in southern Oklahoma is formed by the Tishomingo and Troy Granites, which are about 1.35 to 1.4 billion years old. The basement of the ancient North American continent began to extend 550Ma ago to 525Ma ago (during

the Cambrian period) creating a series of northwest-trending faults across south and southwest Oklahoma. The rift was filled by erupted volcanic rocks (Figure 8A). This strong igneous activity concentrated in south Oklahoma created the "Southern Oklahoma aulacogen" (Suneson, 1997). At about 520Ma ago (late Cambrian) to 340 Ma ago (late Mississippian), the tectonic activity ceased and southern Oklahoma was covered by a broad sea into which limestones, sandstones, and shales were deposited (Figure 8B and C) (Suneson, 1997).

At about 350Ma ago (middle Mississippian), a major period of folding, faulting, and mountain building, the Ouachita orogeny, began in southern Oklahoma (Figure 8D) (Suneson, 1997).

The area east of the Arbuckle Mountains (where the Wyche Shale Pit is located) was affected by the same orogeny that affected the Arbuckle Mountains and is considered a part of this geologic province. However, it is not considered to be part of the Southern Oklahoma Aulacogen due to the great difference in thicknesses of deposits in the west area. The Lawrence Horst (also known as the Laurence Uplift) was formed during the Pennsylvanian; its western end was uplifted more than its eastern end, exposing older rocks in the west and younger rocks in the east. The Franks Graben is open to the east, merging with the Arkoma Basin. Rocks dip to the west, older rocks are exposed to the east and younger rocks to the west (Figure 5, 6, and 7) (Suneson, 1997).

The Woodford Shale tends to have a similar depositional geometry as the Hunton Group, observed in the seismic interpretation. Therefore, structural and isopach maps of the Hunton Group in southeastern Oklahoma can provide information about the Woodford (Figure 9).

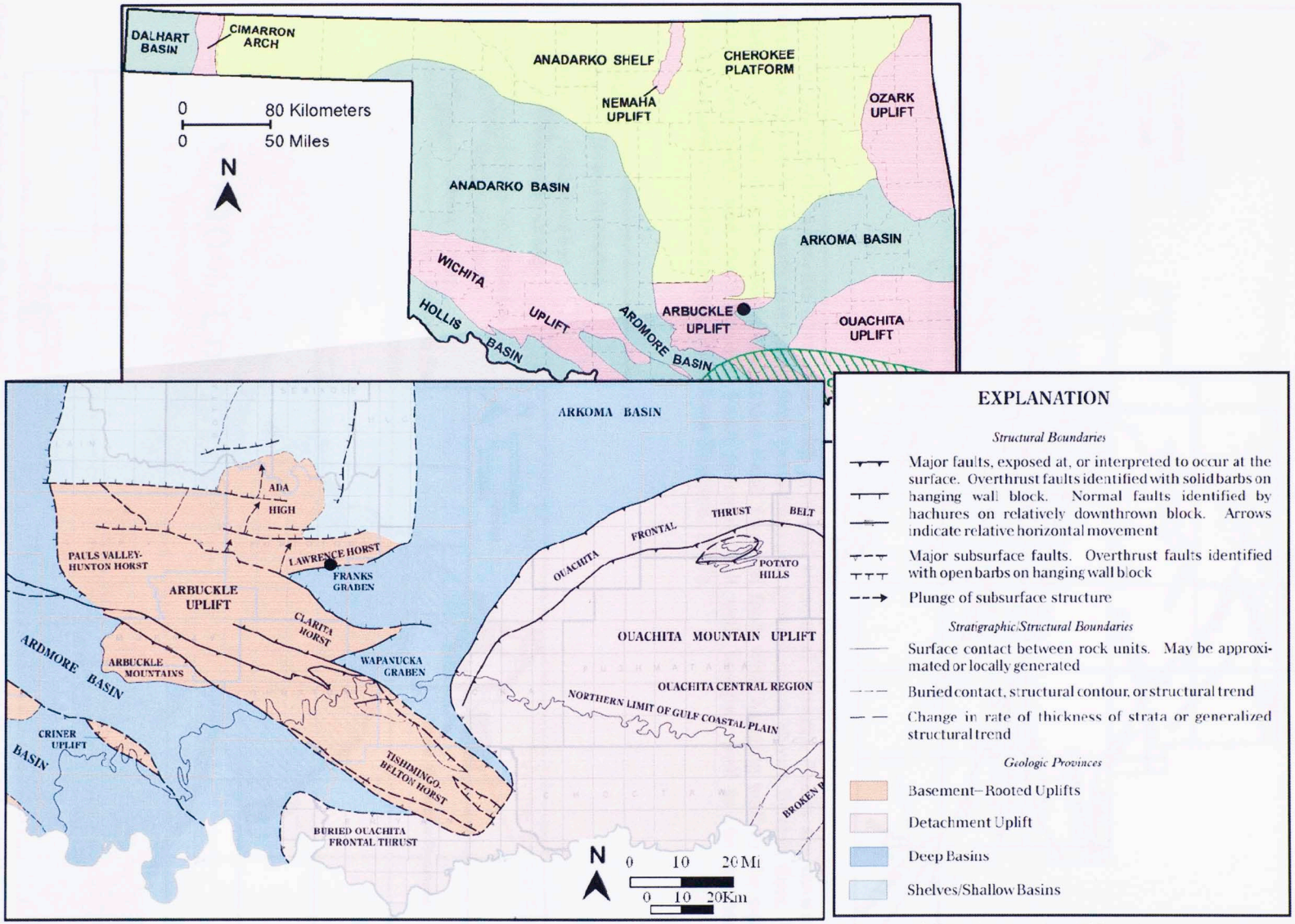

Figure 5. Location of the study area (identified with a black dot) within the major geologic provinces of Oklahoma (modified from Northcutt, 1995).

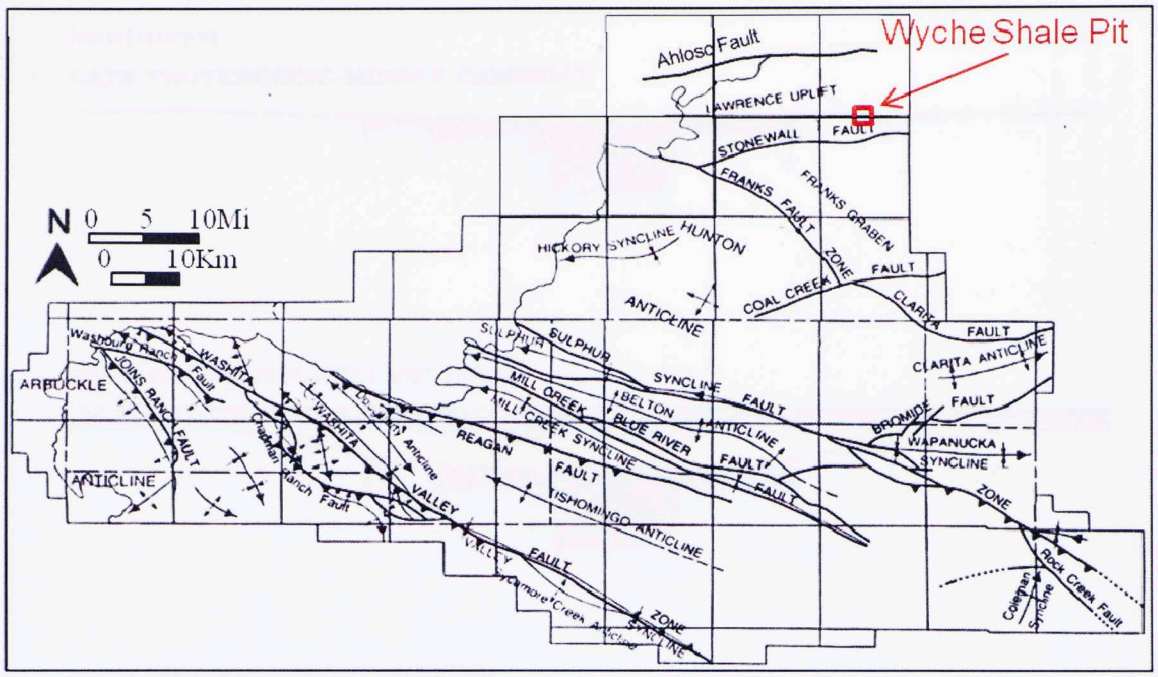

Figure 6. Map of the Arbuckle Mountains with principal structural features. Faults are shown by thick lines (thrust faults with sawteeth), folds (anticlines and synclines) are shown by thin lines. The location of study area is between the Ahloso Fault (normal fault with hanging wall to the north, striking east-west), and the Stonewall Fault (normal fault with hanging wall to the southeast, striking southwest-northeast) (modified from Suneson, 1997).

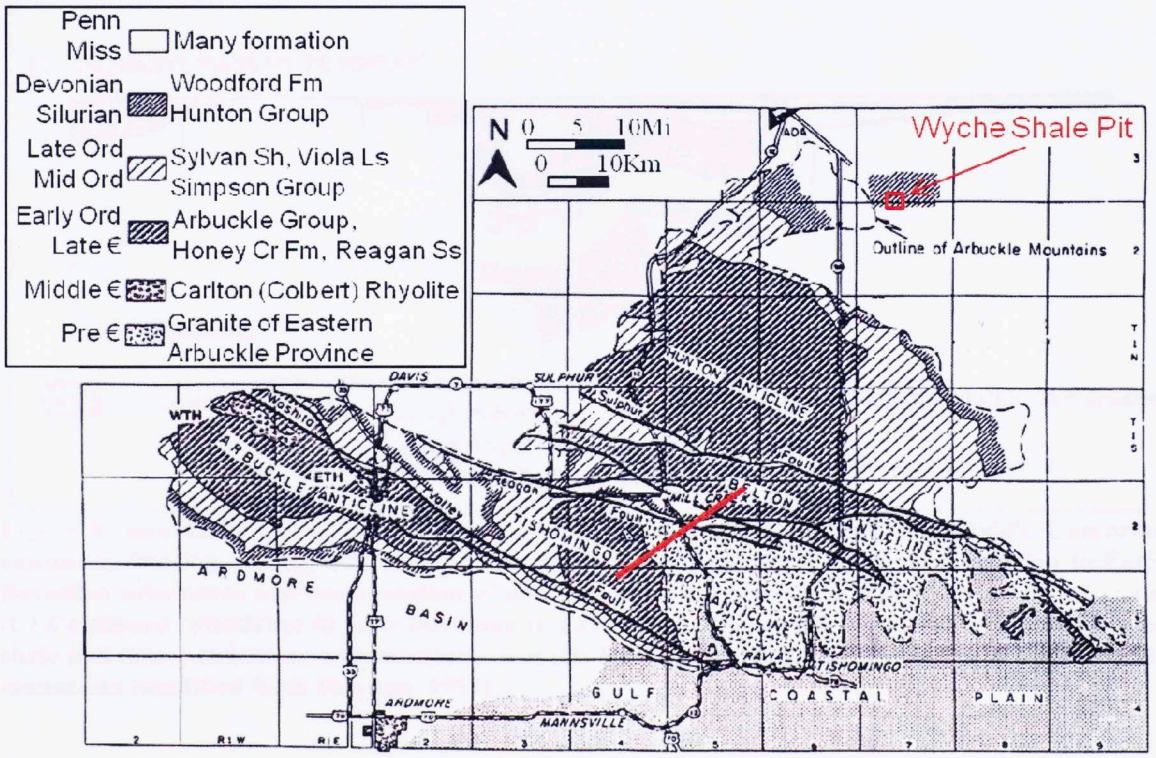

Figure 7. Geologic map of the Arbuckle Mountains, with red line showing the approximate location and trend of the cross-section in Figure 8 (modified from Suneson, 1997).

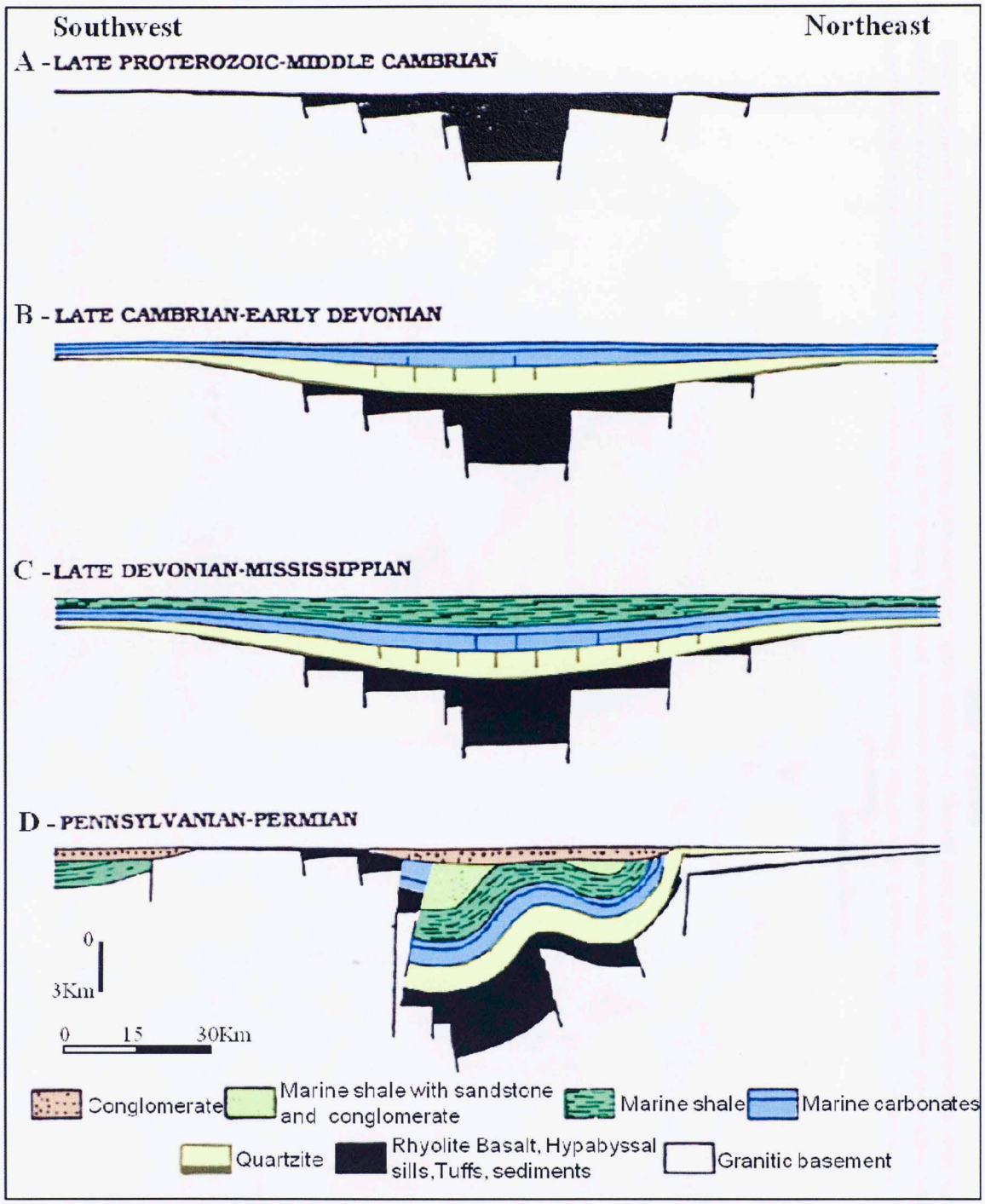

Figure 8. Structural development of the Southern Oklahoma aulacogen. (A) Middle Cambrian extension, faulting, rifting, and filling of the rift with volcanic rocks, (B) Late Cambrian to Early Devonian subsidence and accumulation of mostly marine limestone and lesser sandstone and shale, (C) Continued subsidence in Late Devonian to Late Mississippian and deposition of mostly marine shale and minor sandstone and limestone, and (D) Folding, faulting, and formation of the Arbuckle mountains (modified from Suneson, 1997).

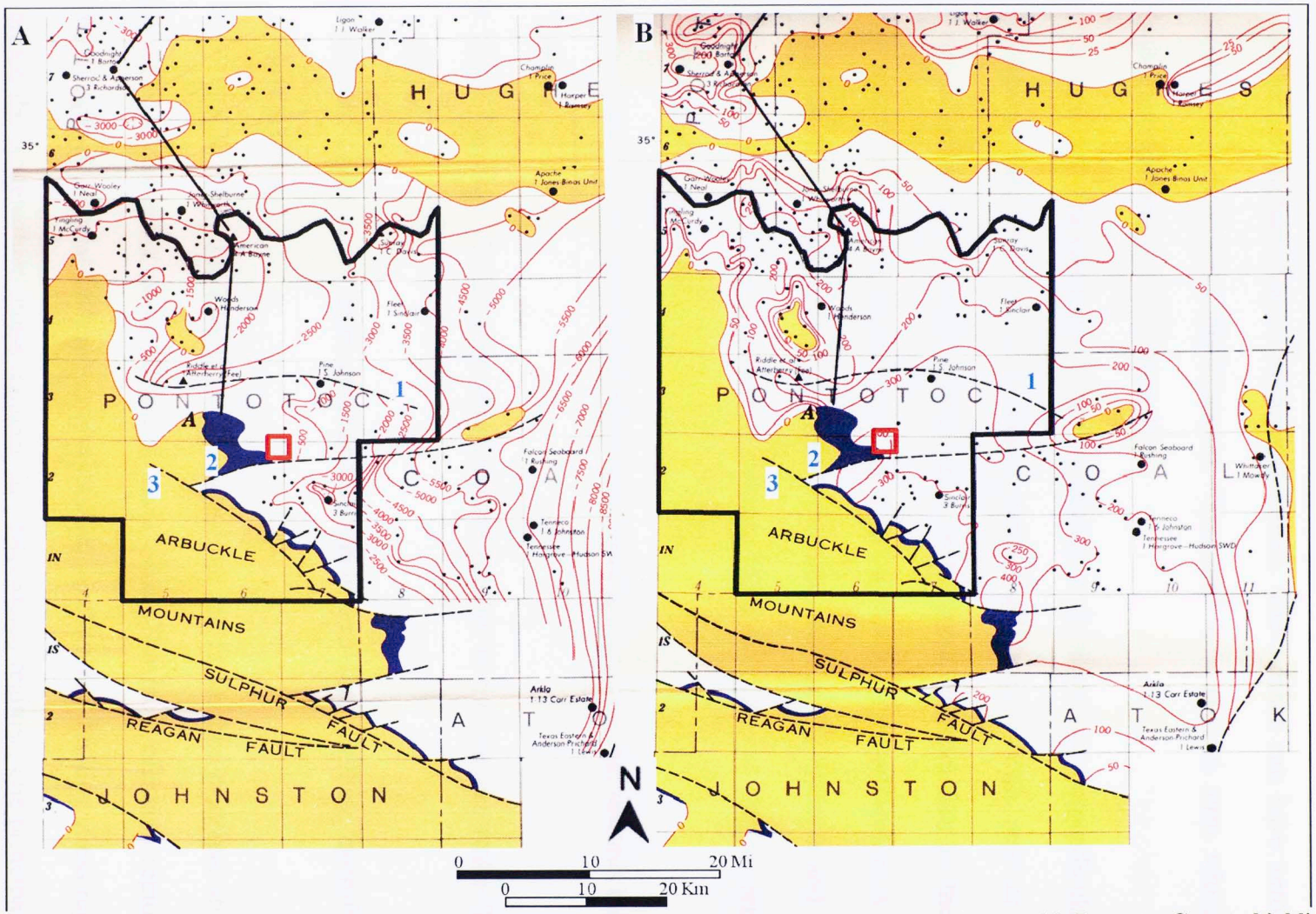

Figure 9. (A) Structure map of the Hunton Group. (B) Isopach map of the Hunton Group in eastern Oklahoma, with Pontotoc County highlighted with a black outline and study area with a red square. Structure and isopach contours are in ft drawn on top of Hunton Group. Yellow represents zero isopach of Hunton, and dark blue represents outcrops of this group. 1=Ahloso fault, 2=Stonewall fault, and 3=Franks fault zone (modified from Amsden, 1980).

1.4 Fractures

A fracture is any non-sedimentary mechanical discontinuity that corresponds to a surface of rupture due to mechanical failure. The surface can have zero to large parallel or perpendicular displacement. "Fracture" is a general term which can be divided into different types (Figure 10):

- Extensional Fractures are Mode I, having a displacement perpendicular to the fracture plane. A joint is a natural extensional fracture with zero or minimal displacement of the walls (movement is extensional perpendicular to the fracture plane) (Figure 11). Unmineralized joints are normally quite permeable. A vein is a fracture filled with mineral precipitate or mud, sealing the fracture and therefore reducing permeability. A dike is a fracture filled with igneous rock or remobilized clastic sedimentary rock.
- Compaction bands are created when movement is compressional towards the fracture plane.
- Shear Fractures (faults) have displacement parallel to the fracture strike (Mitcham, 1963).
- Induced fractures are those generated by human activities (drilling, hydrofracturing, core handling, etc.).

Stress is the force applied on a plane per unit area. The principal stresses are $\sigma 1 > \sigma 2 > \sigma 3$, oriented perpendicular to each other. The most common regional earth stress regimes (normal-faulting, reverse-faulting, and wrench-faulting stress regime) are termed the Andersonian stress regimes. In Andersonian regimes, one principal stress is vertical and the other two are horizontal. In geology, compressional stress is considered

positive. However, extensional fractures (joints) require tensional (negative) stress to be created (Figure 12) (Lacazette, 2000).

There is a close relation between the orientation of fractures and the orientation of the stress field. The plane of an extensional fracture (a joint) is perpendicular to the direction of the minimum principal stress, σ3, during propagation. The plane of a shear fracture (a fault) has an angle ranging from 25-40° with the maximum principal stress, σ1 (Lacazette, 2000).

A fracture set is a group of fractures with similar geometry. They can be systematic (having regular parallel orientations and regular spacing), and nonsystematic (having irregular geometry and terminate in older joints) (Figure 14) (Van der Pluijm, 2003).

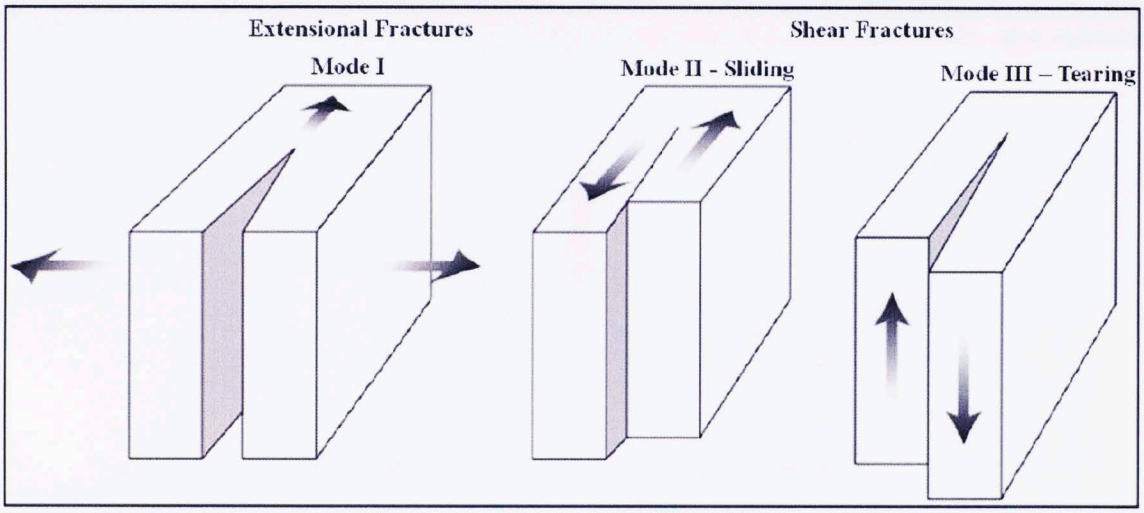

Figure 10. Sketch blocks presenting the models for the different types of fractures: extensional and shear (divided into sliding and tearing) (modified from Van der Pluijm, 2003).



Figure 11. Photo from the Wyche Shale Pit Wall #4 showing fracture planes with approximately west-east strike, possibly representing extensional fractures.

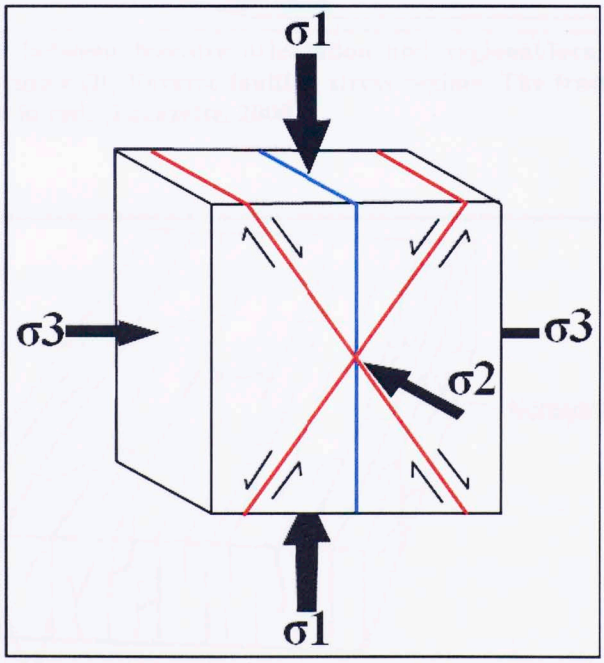

Figure 12. Relationship between fracture orientation and the orientation of the maximum and minimum principal stresses. The fracture is represented in cyan, while the faults are in red (modified from Lacazette, 2000).

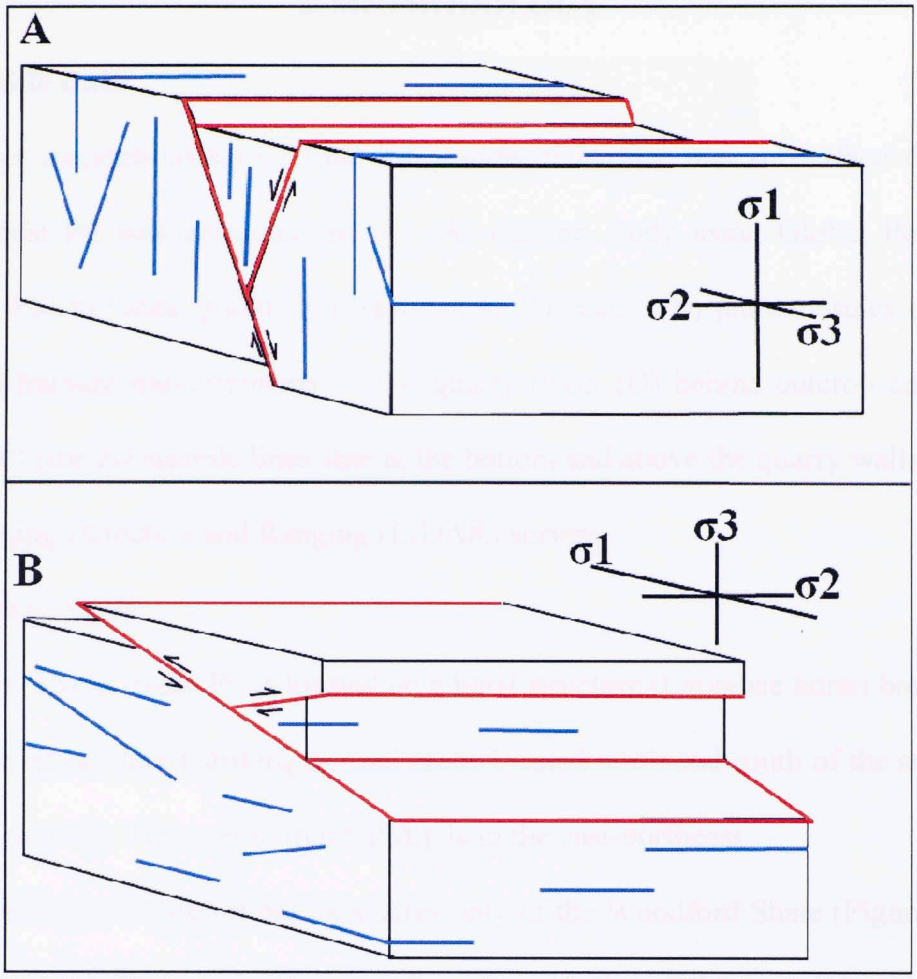

Figure 13. Relationship between fracture orientation and regional/local principal stresses. (A) Normal faulting stress regime (B) Reverse faulting stress regime. The fractures are represented in cyan, while the faults are in red. (Lacazette, 2000).

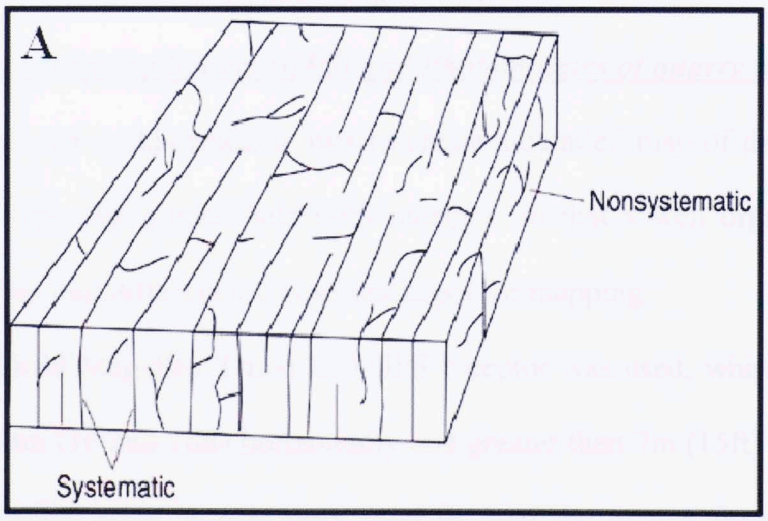

Figure 14. (A) Sketch block representing patterns for systematic and nonsystematic fractures (modified from Van der Pluijm, 2003).

2. METHODOLOGY

2.1 Available Data

This research consists of the integration of surface and subsurface data. The Wyche Shale Pit was characterized by: (A) outcrop study using Global Positioning System (GPS) to locate points and fractures in 3D space, (B) photomosaics of quarry walls, (C) fracture measurements on the quarry floor, (D) behind-outcrop coring and logging, (E) five 2D seismic lines shot at the bottom and above the quarry walls, and (F) Laser Imaging Detection and Ranging (LIDAR) survey.

2.1.1 Outcrop Study

The Wyche Shale Pit is located on a horst structure (Laurence horst) bounded by two southwest-northeast striking normal faults located north and south of the study area (Figures 5 and 15). The overall trend of dip is to the east-northeast.

The Wyche Shale Pit has exposures only of the Woodford Shale (Figures 2, and 11), as laminated shale, with color variations from black to light gray. It is not possible to observe the Hunton Group exposures in this area, nor the unconformity surface that separates the Woodford from the underlying Hunton.

2.1.1.1 Global Positioning System (GPS) and Photomosaics of quarry walls

The first step in this research was to create a detailed map of the area of study using a metric tape and a hand-held GPS receptor, so that a well organized data set could be imported into different software packages for mapping.

A hand-held Magellan Triton 200 GPS receptor was used, which has accuracy between 3 and 5m (10 and 16ft) horizontally and greater than 7m (15ft) vertically. Due to the large vertical error, it was only used to map the quarry floor and the well

locations (Figure 16). Complete GPS locations are provided in Appendix 1.

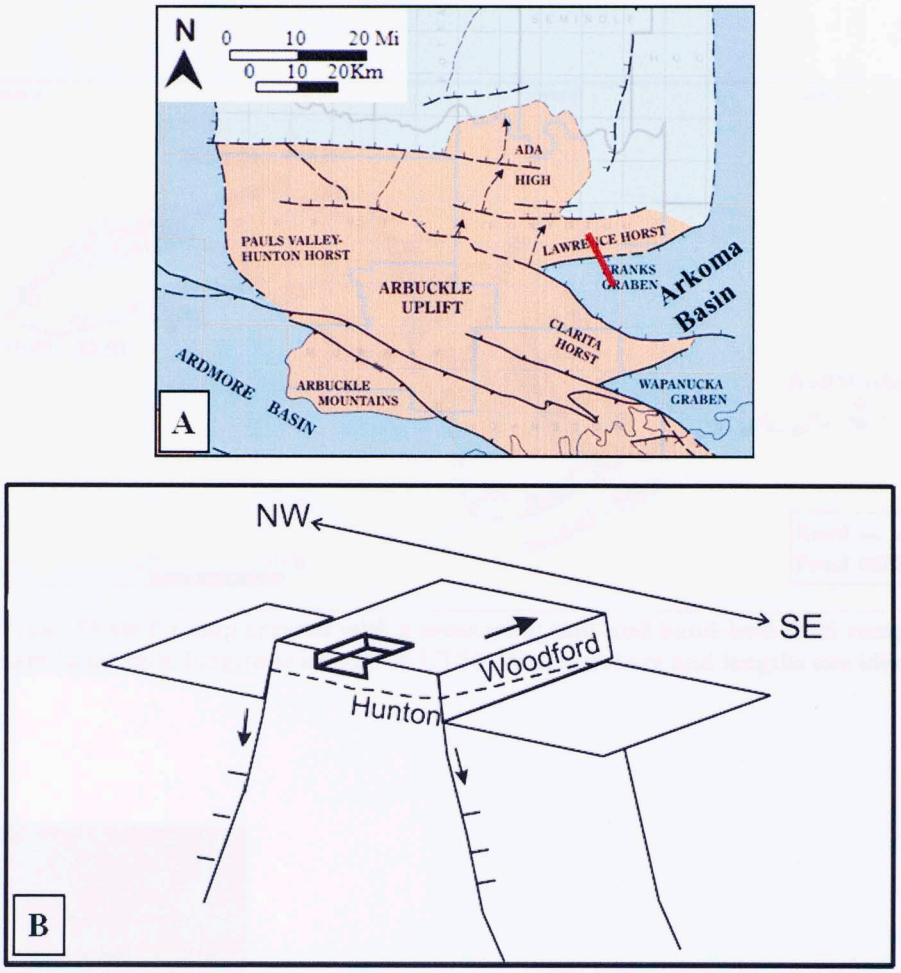

Figure 15. (A). Major structural elements around Wyche Shale Pit (modified from Northcutt, 1995), with location of cross-section. (B). Sketch cross-section showing structural position of the outcrop (not to scale).

The Wyche Shale Pit has five walls. Walls #1 and 2 are located in the upper bench (at higher elevation). Wall #3 is located in a medium bench. Wall #4 is the largest, and the height changes due to extension from the medium bench to the lower bench. Wall #5 is located in the lower bench (Figure 17).

Photomosaics of quarry walls have been assembled using merged digital field photographs (Figure 18). An advantage of creating a digital map was the ability to assign the correct coordinates into interpretation software where the rest of the data is

loaded. Photomosaics for Walls #1-5 are in Appendices 2-6.

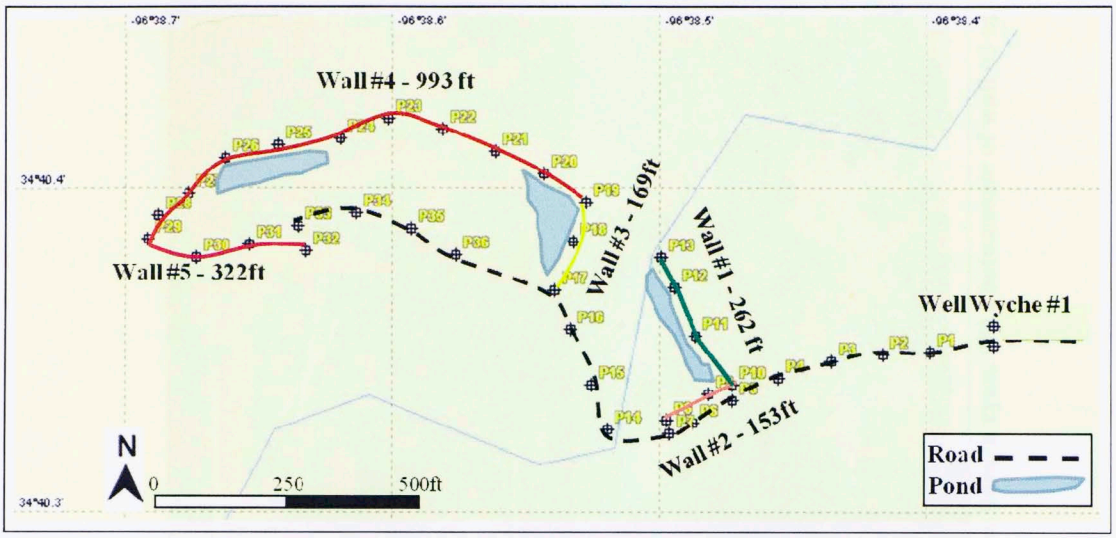

Figure 16. Wyche Shale Pit map created with a measuring tape and hand-held GPS receptor. Coordinates are in latitude/longitude as well as UTM. Wall numbers and lengths are identified.

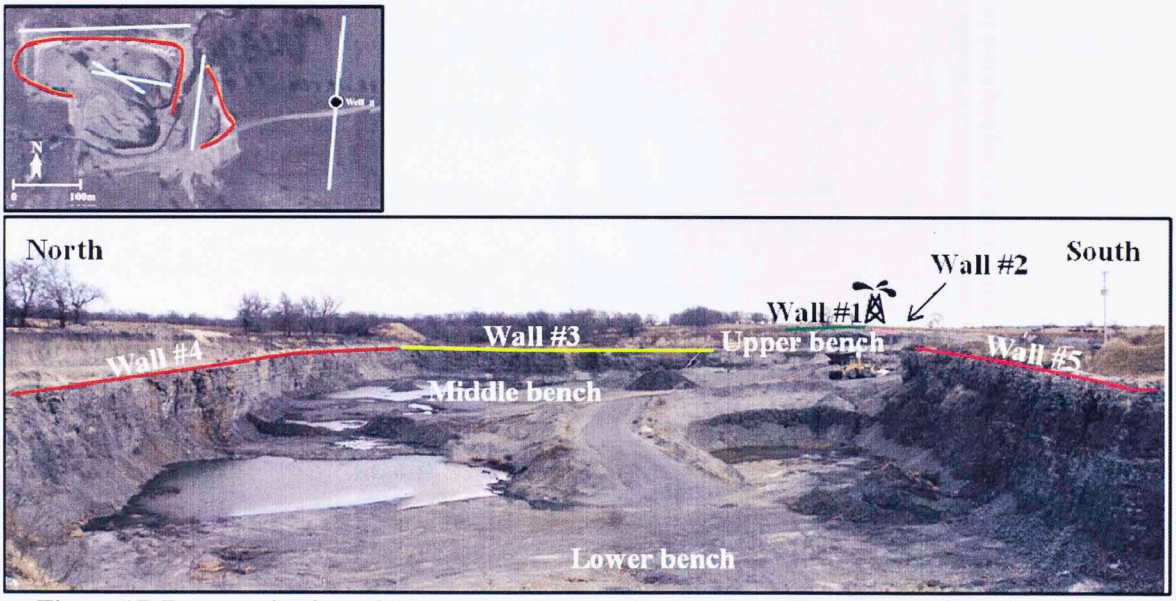

Figure 17. Panoramic view of the quarry, showing the location of the well, walls and benches.

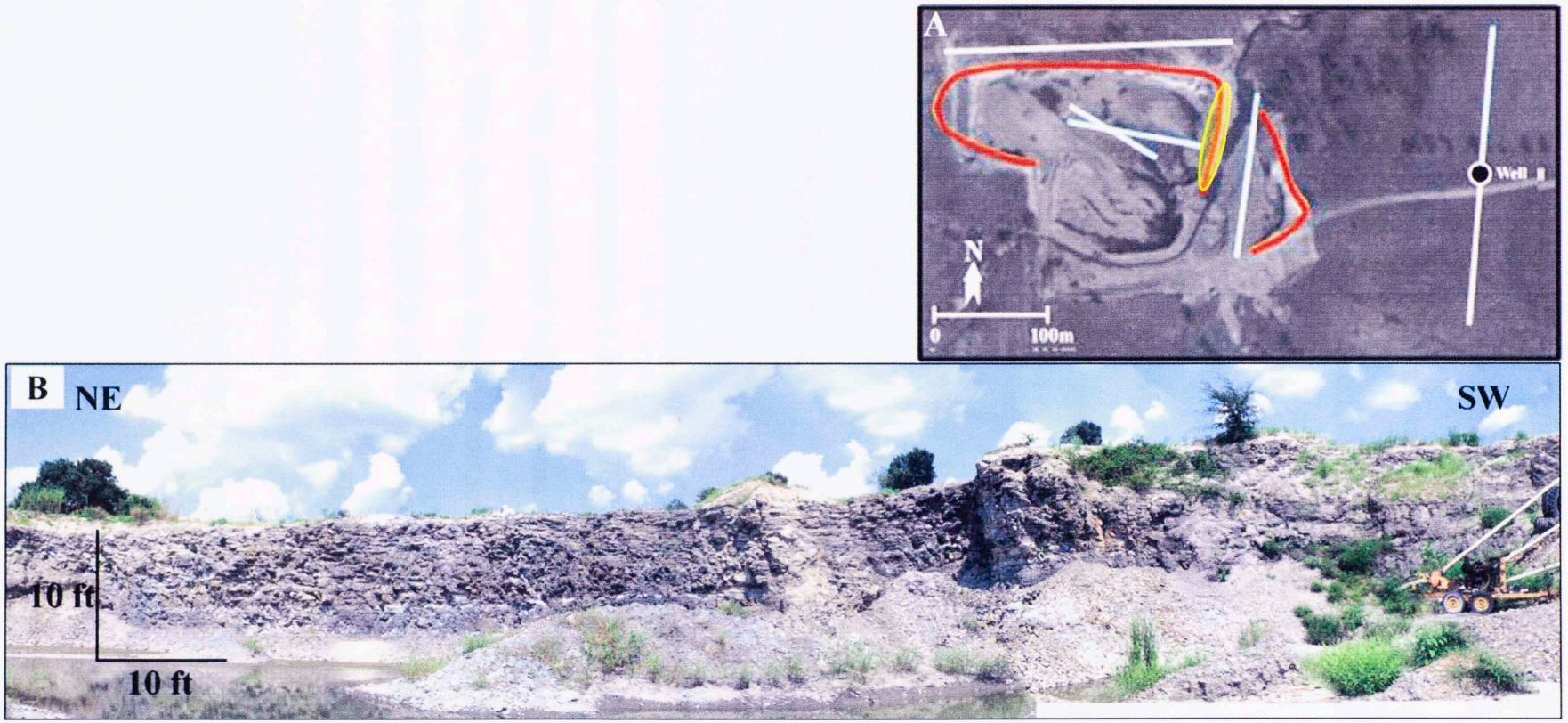

Figure 18. (A) Plan view of the Wyche Shale Pit, with wall #3 highlighted in orange and seismic lines in cyan. (B) Photomosaic of wall #3 at Wyche Shale Pit.

2.1.1.3 Fracture measurements on the quarry floor

Two 6m (20ft) long sections or scan lines were measured for fractures on the quarry floor, specifically in the lower bench between wall #4 and 5 (Figure 19). These lines were used to document the different fracture orientations with a Brunton Compass and also to analyze whether or not the fractures where healed and, if so, with what kind of mineral. In this case, only the strike of the fracture was considered with values represented as azimuth strike (from 0°- 180°), assuming a dip of 90°. The measured values were then plotted using a software designed to accomplish most of the operations and plotting with orientation data. The program plots three-dimensional data on a lower hemisphere projection and saves it as standard graphic files (Allmendinger, 2002). Appendix 7 contains measurements from the scan lines.

2.1.2 Behind-outcrop Coring and Logging

The Wyche #1 well was drilled in 2007 about 150m (500ft) east of the eastern quarry wall (Wall #1) (Figure 1). These data were mainly analyzed by Buckner (2009).

The logs acquired penetrated to a depth of 76.2m (250ft), having a resolution of 7.62cm (3inches). The conventional logs are gamma ray, resistivity, density, and neutron porosity. When viewing the logs, the contact between the upper and middle Woodford at 36.88m (121ft) depth is obvious, as is the unconformity between the Woodford and the Hunton at 64.62m (212ft) depth (Figure 20).

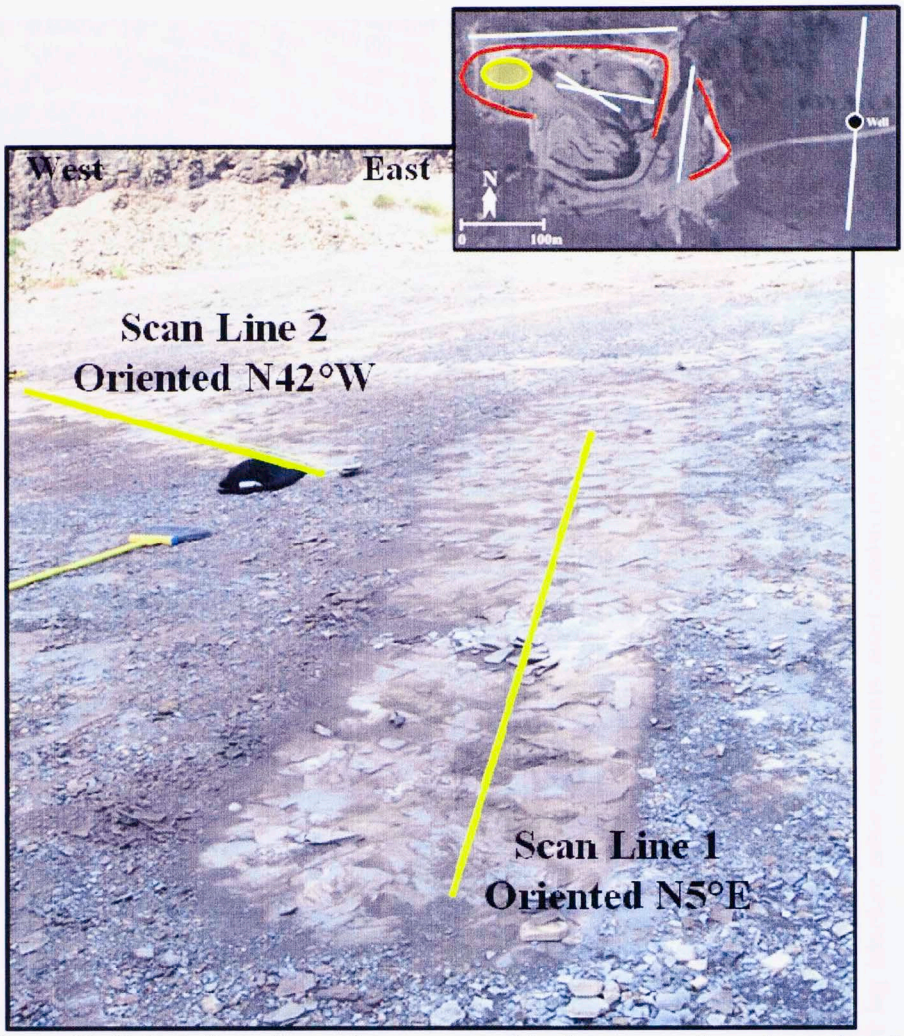

Figure 19. Orientation of scan lines measured in the quarry floor, lower bench.

Unconventional logs were also acquired. However, this thesis only includes analysis of the borehole image log, which plots microresistivity measurements coded with a color scale around the borehole. Bedding, lithology and fluid variations, fractures (open or healed), phosphatic and pyrite nodules, were all imaged with a resolution of 1.27cm (0.5inches). The contact between the upper and middle Woodford and unconformity between the Woodford and the Hunton were also imaged (Figure 20) (Davis et al., 2006). The image log is in Appendix 8.

The core which Buckner described deepens from 3m (10ft) to 64m (210ft), unfortunately missing the Woodford-Hunton unconformity by 0.6m (2ft) (Appendix 9).

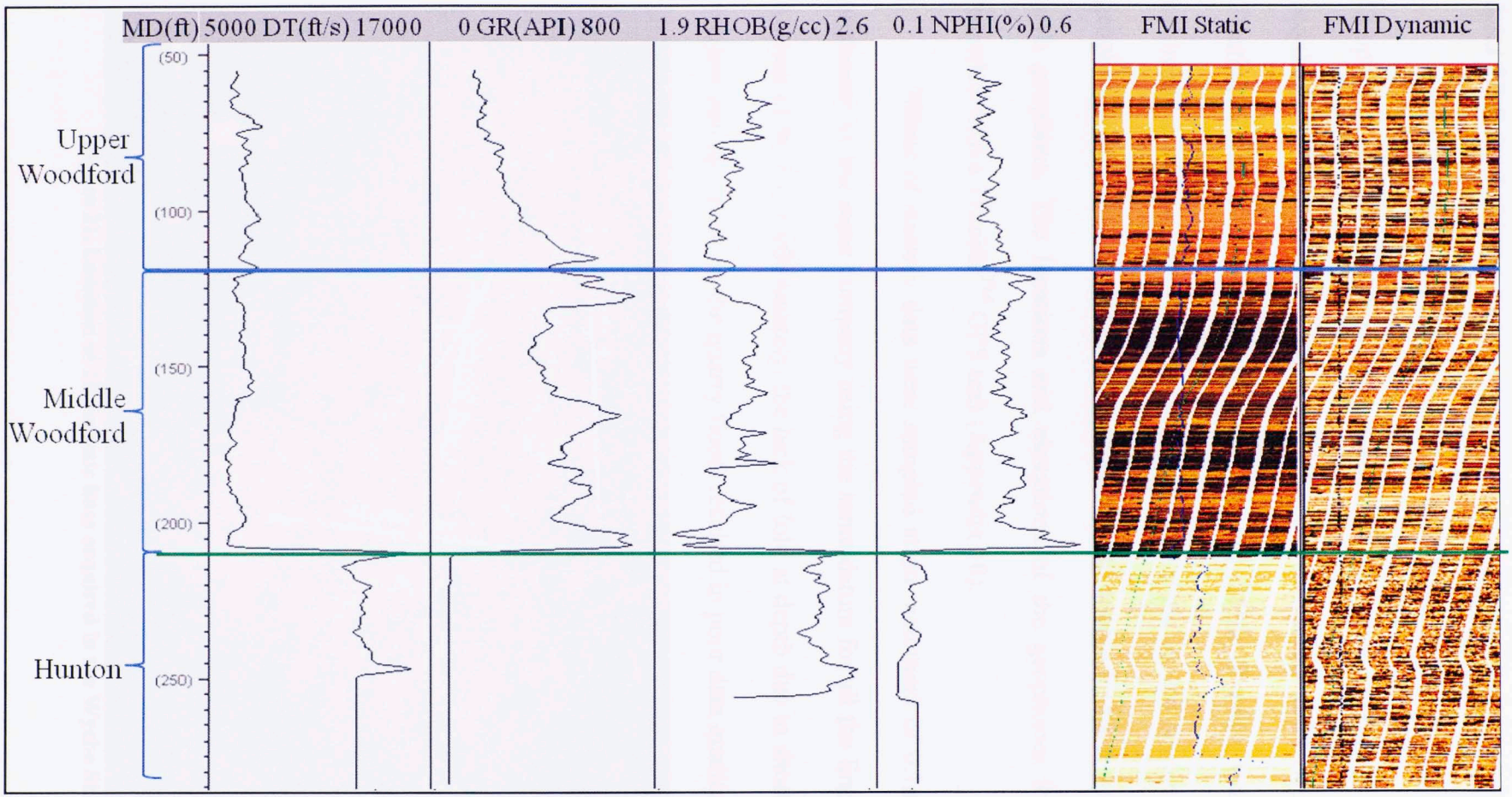

Figure 20. Sonic (ft/s), Gamma Ray (API), Density (g/cc), Neutron porosity (%), Borehole Image log (static and dynamic) from the Wyche #1 well. The contacts between the Upper and Middle Woodford, as well as the unconformity between the Woodford-Hunton are identified. Notice the different log responses as well as the changes in color in the borehole image log (darker color represents most conductive material, lighter color represents most resistive material).

2.1.3 2D Seismic Lines

Five 2D seismic lines were shot at Wyche Shale Pit by the company 3D Geophysics – Three-Dimensional Subsurface Imaging (Figures 21 and 22). The acquisition was conducted with a 48 channel Bison Series 9000 Digital Instantaneous Floating Point Signal Stacking Seismograph, 28Hz P-wave geophones, and an automatic sledge hammer striking an aluminum plate as the source (Figure 23). The geophones were spaced 0.91m (3ft) apart and the source location was moving next to each geophone. The locations and elevations of the geophones for each line were recorded with a Trimble^{TM} GPS unit (Appendix 10).

300ms of seismic data were sampled at an increment of 0.1ms. The data were processed by the same company using the same datum for all the lines and a frequency low-cut of 90 Hz. Unfortunately, the lack of fold at depth due to short line length (there was not enough space on the quarry floor) resulted in poor data quality in lines 1 and 2.

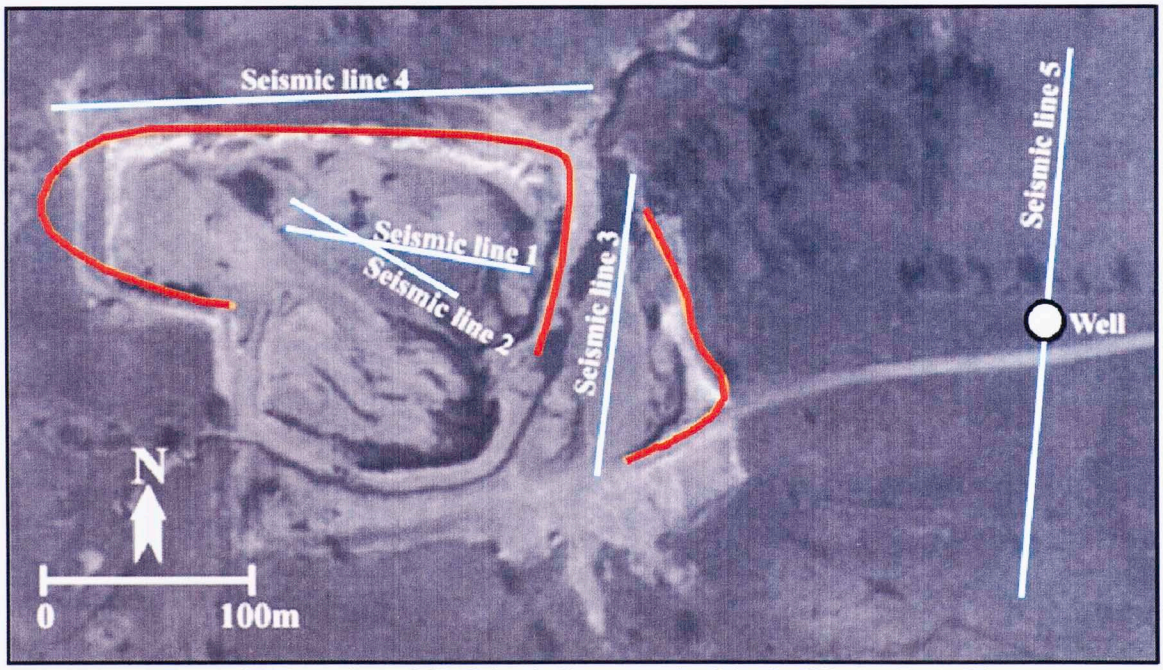

Figure 21. Location of 2D Seismic lines acquired in the Wyche Shale Pit.

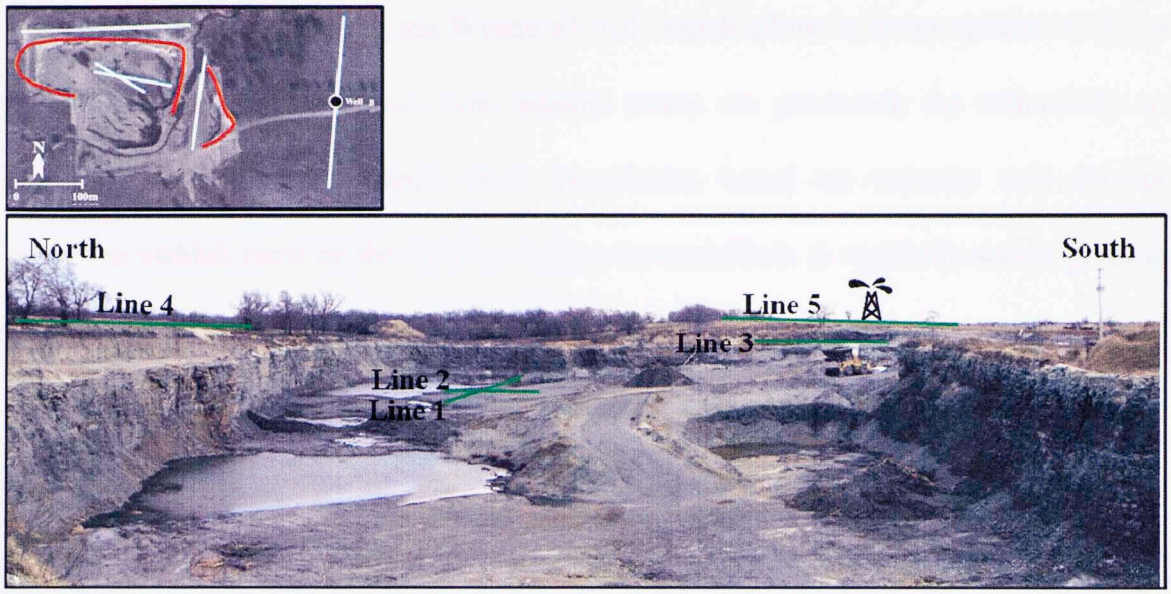

Figure 22. Panoramic view of the quarry, showing the location of the 2D Seismic Lines.

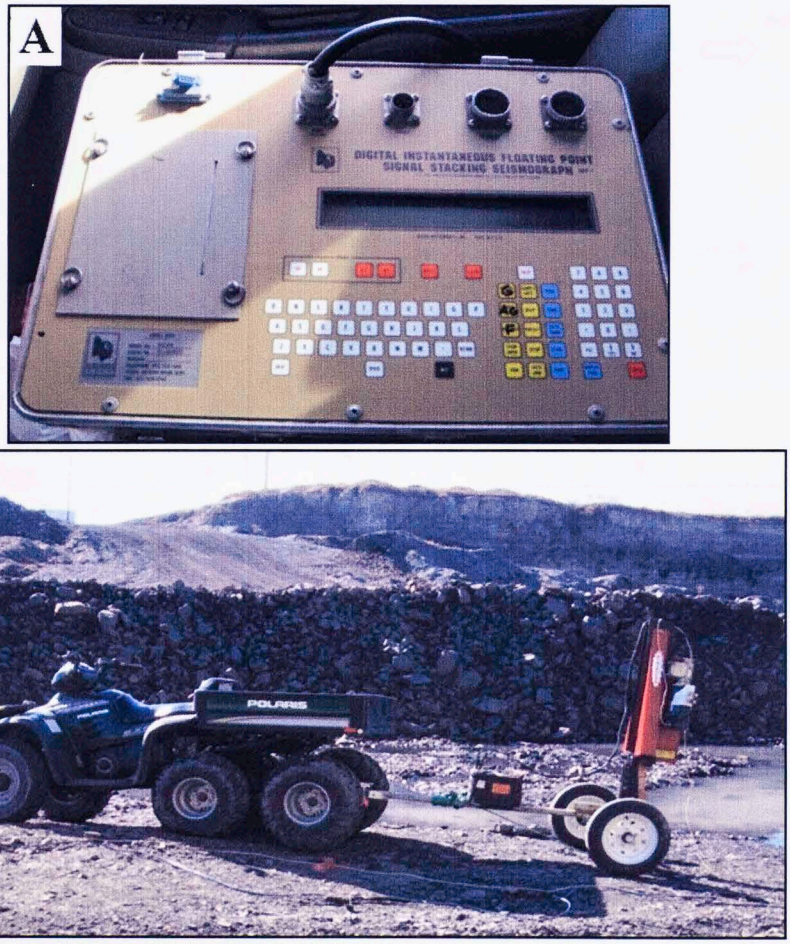

Figure 23. (A) 48-channel Bison Series 9000 Digital Instantaneous Floating Point Signal Stacking Seismograph, and (B) Source, automatic sledge hammer striking an aluminum plate.

Line 5 passes through the Wyche #1 well which allows a better validation of the seismic data. Figure 24 shows how seismic traces are produced; the reflectivity or reflection coefficient represents layer boundaries based on velocity and density variations (which most of the time are unknown variables). A synthetic seismogram is generated in a similar manner by convolving the reflectivity derived from sonic and density logs with a wavelet (that can be theoretical or derived from the seismic data). The advantage is to compare major reflections on the seismic with important tops picked on the well logs to use as reference points and to obtain a better correlation coefficient between the data in depth (logs) and the data in time (seismic).

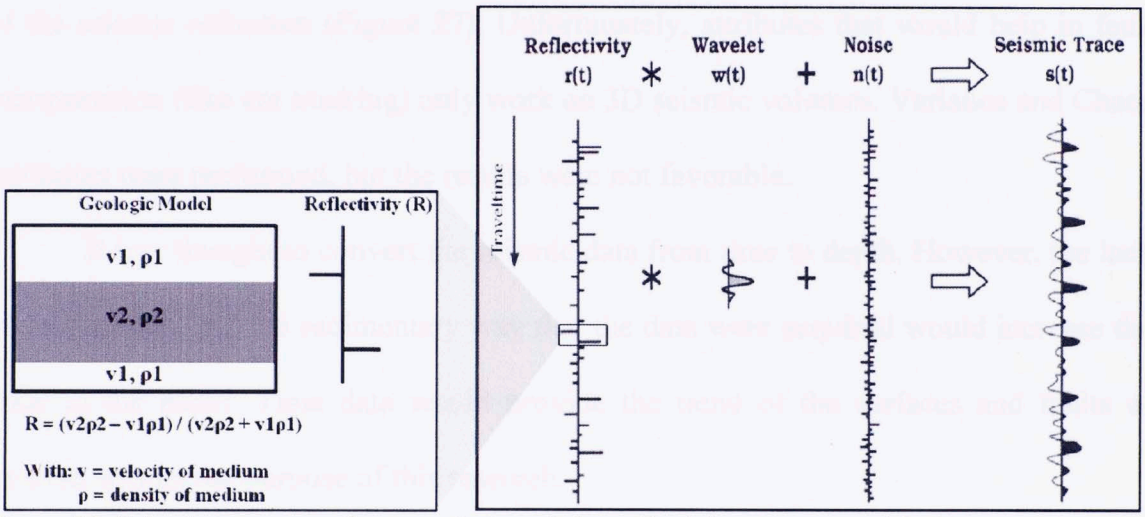

Figure 24. Seismic traces are the convolution of the reflectivity spectrum with the source wavelet, plus noise (modified from Partyka, 1999 and Negrey, 2005).

The formation tops replaced the lack of a checkshot survey (however this method is not as accurate). Different source wavelets were tried, including those statistical and extracted from the well (constant phase and full wavelet). A way to improve the correlation between the seismic and the well is to stretch and squeeze the logs. The synthetic seismogram between the sonic and density logs from the Wyche #1 well and line #5 gave a correlation coefficient of 0.87. A time-depth curve, a new sonic

log, and a new density log were generated based on the correlation performed (Figure 25).

The interval velocities extracted from the sonic log are shown in Table 1. The peak frequency of the data is 105Hz, using an average velocity of 2590m/s (8500ft/sec). For the entire log length, the seismic is able to resolve layers as thin as 5.8m (20ft) (Figure 26).

The five 2D seismic lines and the well log were loaded into a 3D interpretation software package. Because the lines were shallow and there was a lot of external noise, a structural smoothing was applied to the lines in an attempt to increase the continuity of the seismic reflectors (Figure 27). Unfortunately, attributes that would help in fault interpretation (like ant tracking) only work on 3D seismic volumes. Variance and Chaos attributes were performed, but the results were not favorable.

It was thought to convert the seismic data from time to depth. However, the lack of well control and the rudimentary way that the data were acquired would increase the error in the result. Time data would provide the trend of the surfaces and faults of interest, so met the purpose of this research.

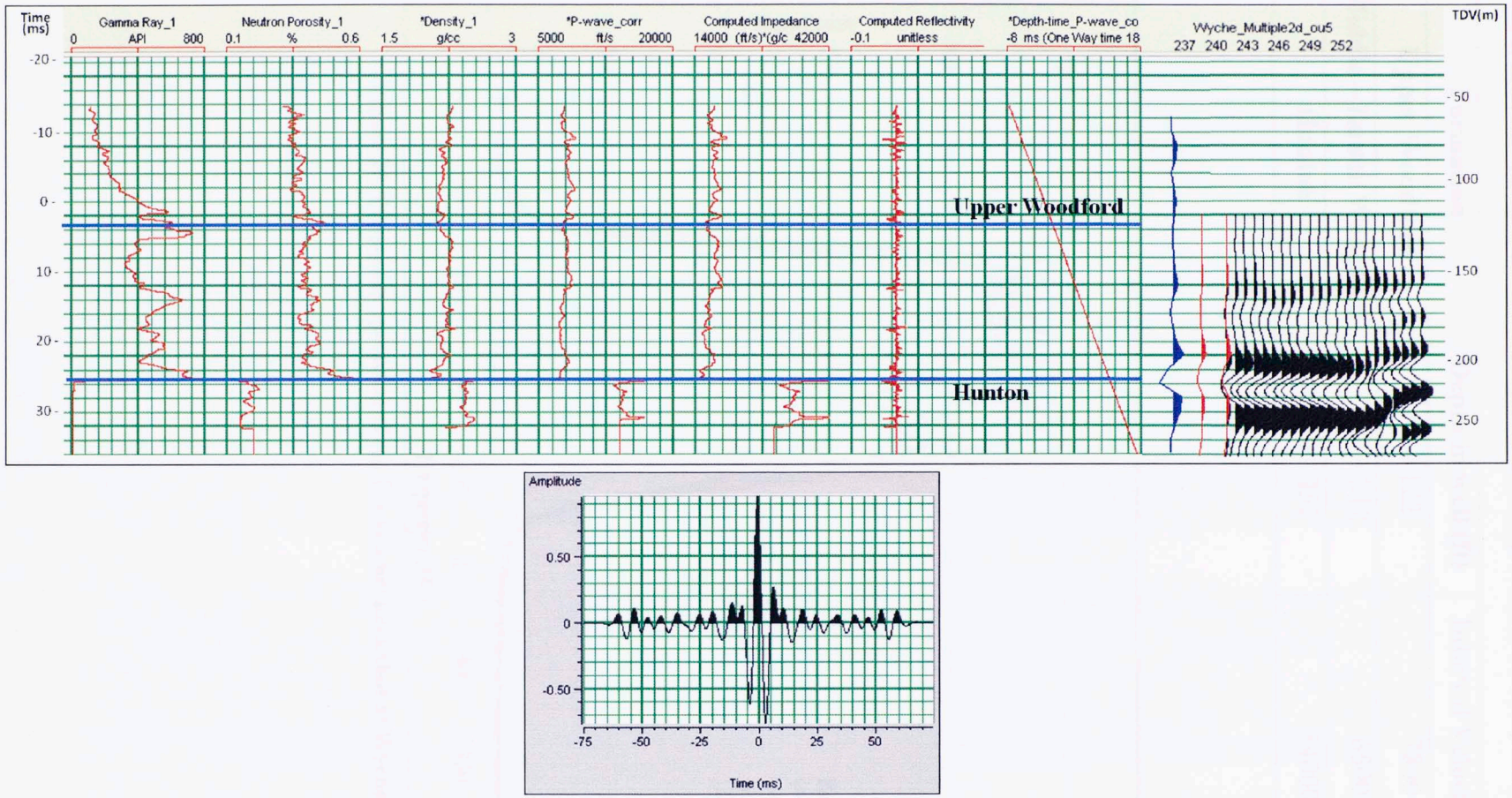

Figure 25. Correlation between seismic data in time and well log data in depth, with a correlation coefficient of 0.97. A time-depth curve was generated, using a wavelet extracted from the well with constant phase.

Table 1. Interval velocities for the different formations present in the study area.

Formation	Depth in well (ft)	Interval Velocity (ft/sec)
Upper Woodford	50 – 122	7800
Middle – Lower Woodford	122 – 212	6500
Hunton	212 - 252	14000

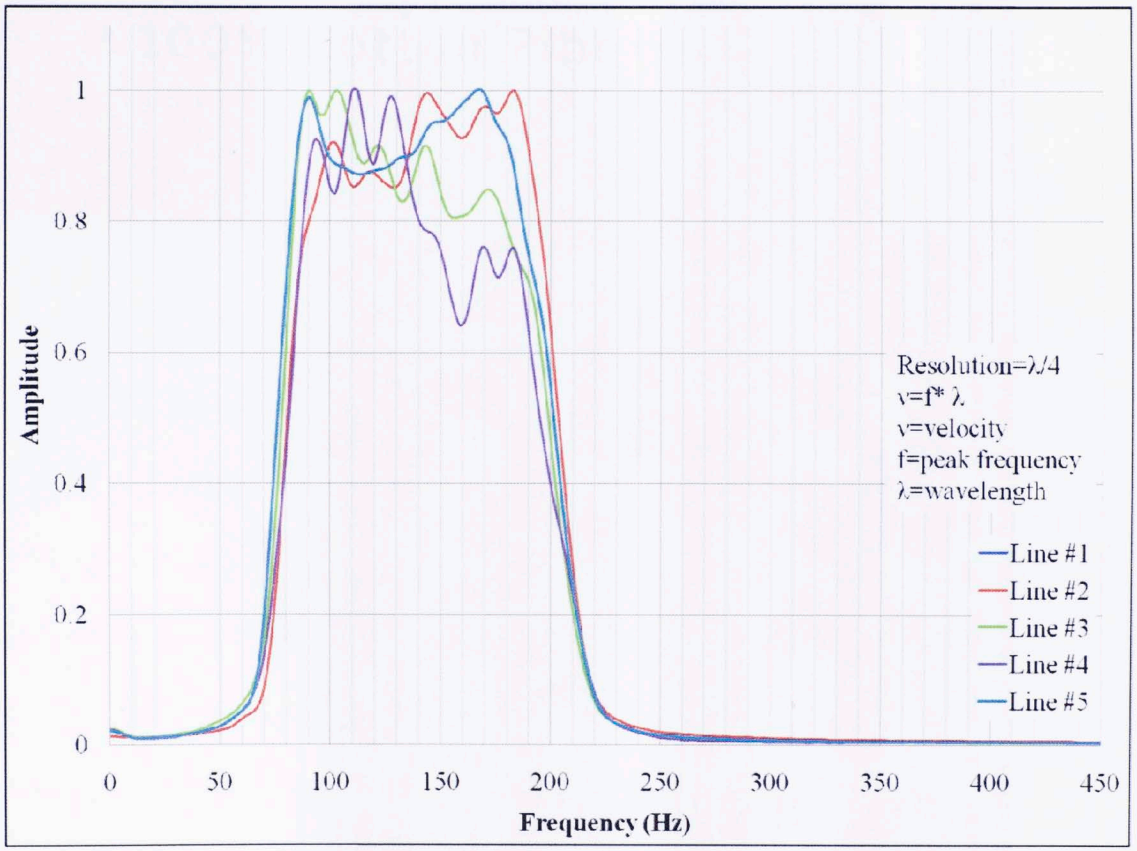

Figure 26. Frequency spectrum of the five seismic lines shot at Wyche Shale Pit

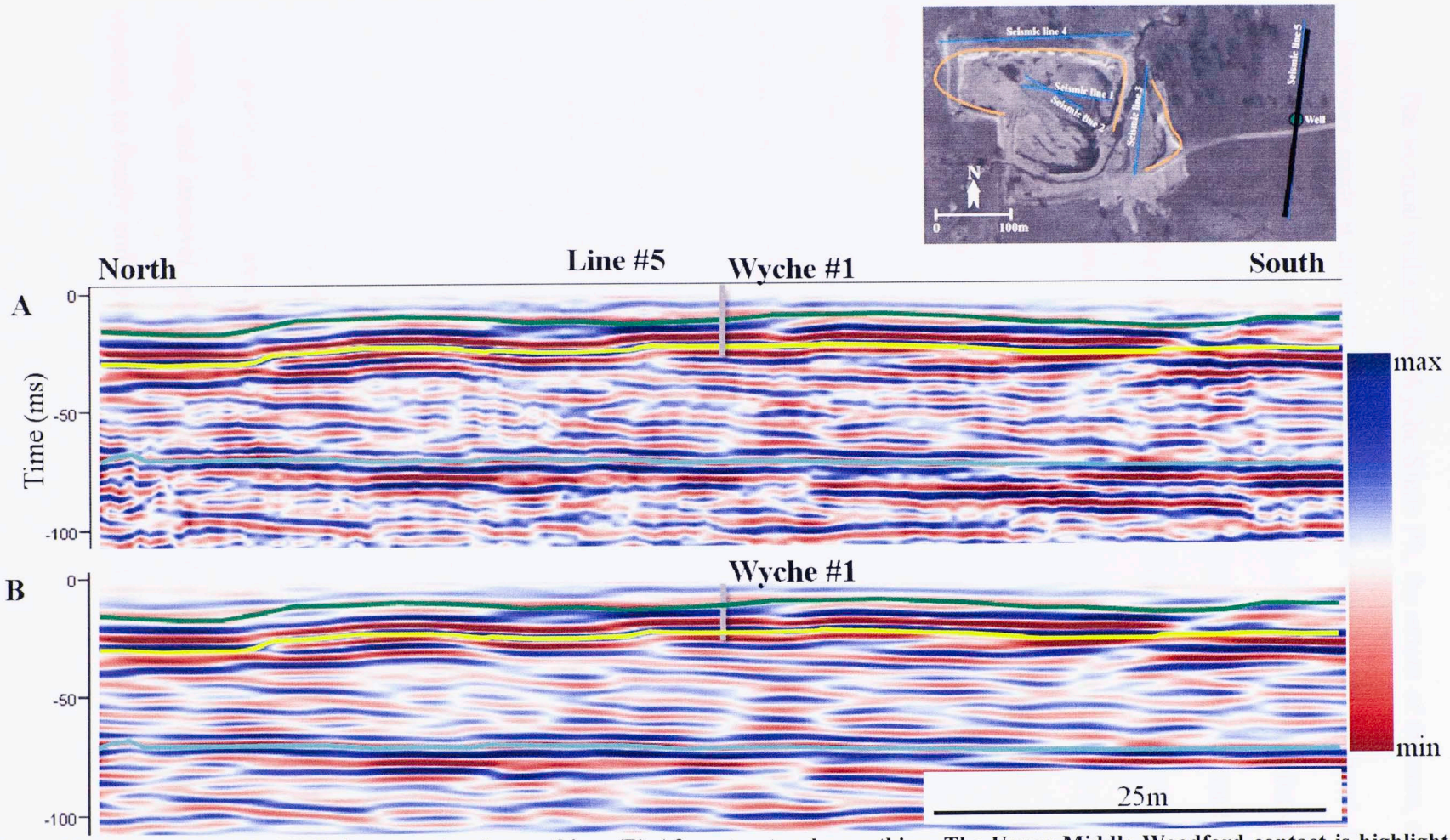

Figure 27. Seismic Line #5. (A) Before structural smoothing, (B) After structural smoothing. The Upper-Middle Woodford contact is highlighted in green, Woodford-Hunton unconformity in yellow, and a interesting interval below the Hunton in cyan, as well as the position of Wyche #1 well.

2.1.4 Laser Imaging Detection and Ranging (LIDAR) data

The vertical walls in the Wyche Shale Pit, the extent of the area, and the amount of fractures made it difficult to characterize the entire area by hand. Laser Imaging Detection and Ranging (LIDAR) is a technique that determines the distance to an object using laser pulses by measuring the time it takes for a pulse to reach an object and return as a reflected signal. Therefore, it has the capability to scan large areas in a short time by recording many distance points in three-dimensions (x, y, z) and creating a point cloud, making it perfect for areas like the Wyche quarry. The output data represents the surface of the quarry walls with millions of points positioned in 3D space.

The LIDAR survey was acquired by Dr. Tim F. Wawrzyniec from the University of New Mexico using a Opentech Inc Ilris 3D Terrestrial Lidar Scanner (TLS) which is capable of acquiring data with an accuracy of 4mm and recording up to 2000 points per second as well as the intensity of the reflected signal which may help in the identification of bedding and lithological changes (Rothfolk, 2006) (Figures 28 and 29). The acquisition is done by placing the equipment at different stations that overlap on the edges, thus providing better resolution of the walls from various angles.

Dr. Wawrzyniec also processed the data, which included aligning the multiple scans to eliminate redundant data points, registering them in the same coordinate system (each point has x, y, and z coordinates that are located in a global datum), point cloud meshing, and removal of points of data not related to the outcrop (like surrounding objects), to finally end up with a unified data set (Figure 30).

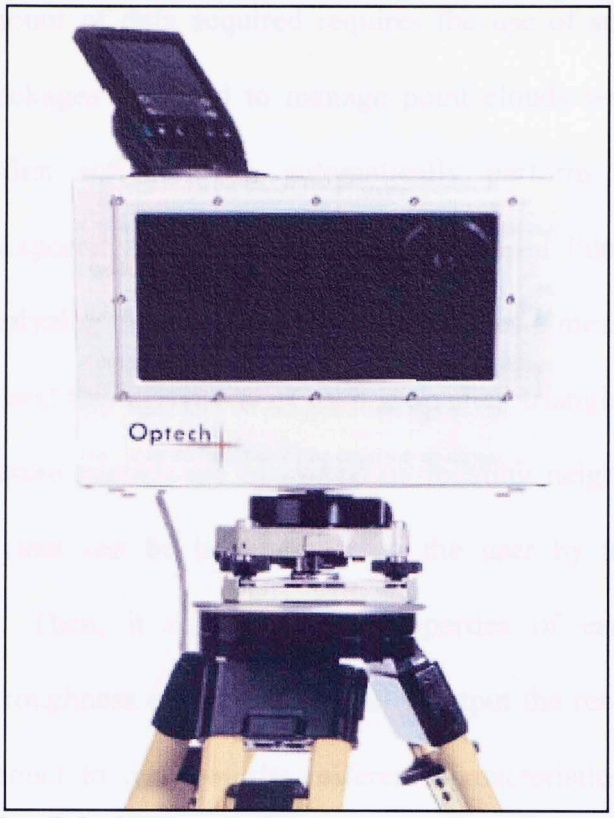

Figure 28. Opentech Inc Ilris 3D Terrestrial Lidar Scanner (TLS). Image courtesy of Tim Wawrzyniec, UNM



Figure 29. View of the Wyche Shale Pit during the Lidar acquisition. Notice the Terrestrial Lidar Scanner.

The large amount of data acquired requires the use of special software. Two different software packages designed to manage point clouds were used to compare their results. The first software can automatically perform rock mass fracture characterization on exposed rock faces using ground-based lidar and digital image processing. While analyzing lidar data, the software creates a mesh of the rock surface from the point cloud and the orientation of each individual triangle is calculated. From this information, fracture patches are identified by locating neighboring patches with similar orientations (that can be hand edited by the user by adding, deleting and modifying a patch). Then, it calculates the properties of each patch, including orientation, size and roughness estimation to finally output the results as a list that can be plotted in a stereonet to compare the different characteristics (Split Engineering LLC, 2009) (Figure 31 B to D).

The second software is used to handle point clouds by performing data inspection and reverse-engineering tasks. The features include processing, data measurements (distances, angles, radii, and volumes), and geometrical primitives (cylinders, planes, vectors, etc), among others (InnovMetric Software, 2009). In this case, the fracture planes were picked manually and imported into a stereonet (Figure 31 E).

Both software applications represent strike azimuth (from 0°- 180°), dip magnitudes (from 0°- 90°), and the trend of the dip direction. The final step was to compare the results from the different point cloud software.

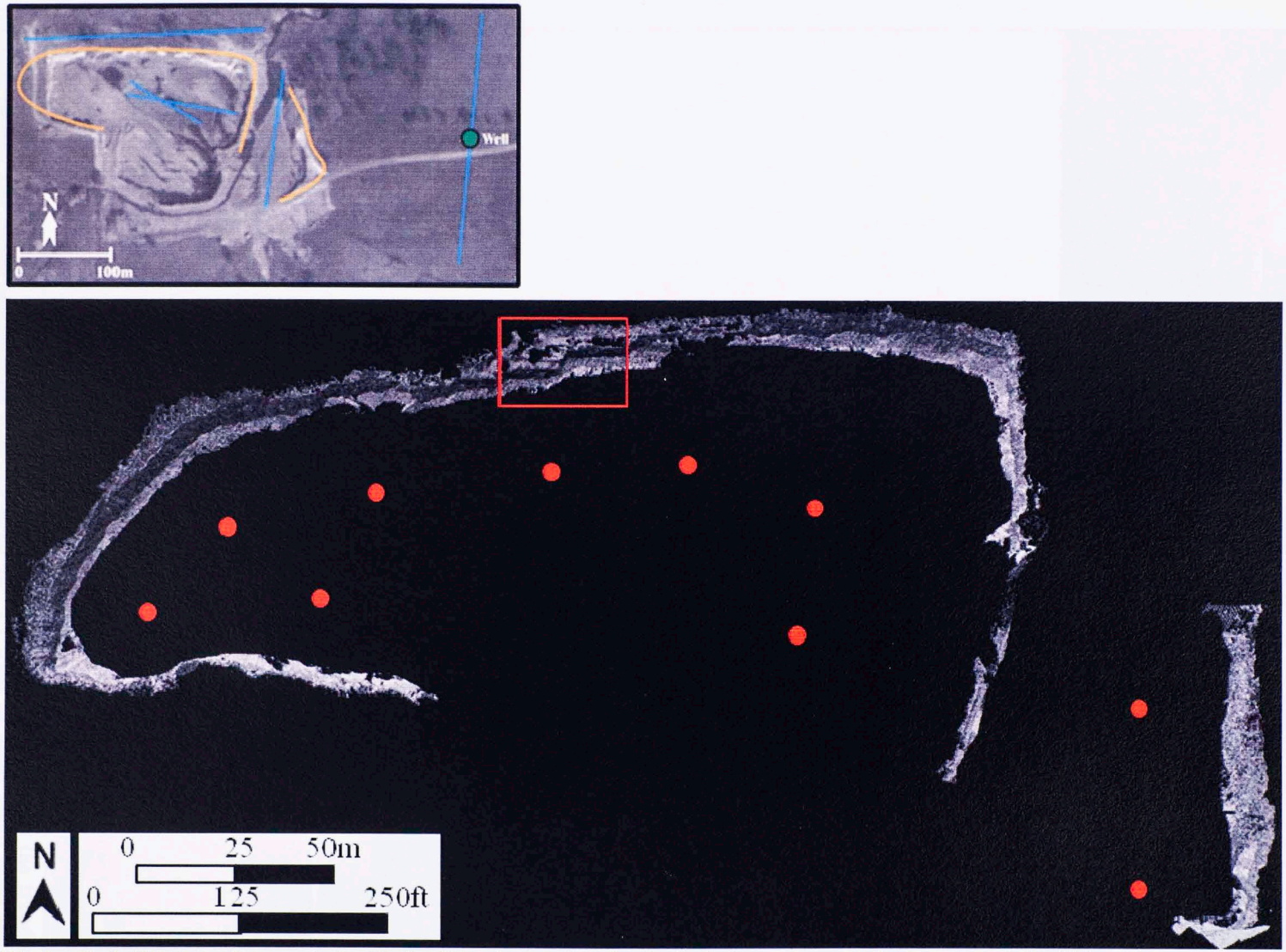

Figure 30. Wyche Shale Pit plan view created with the lidar data point clouds. Red dots represent the location of the different stations used during the data acquisition. The red box delimits the area shown in Figure 31.

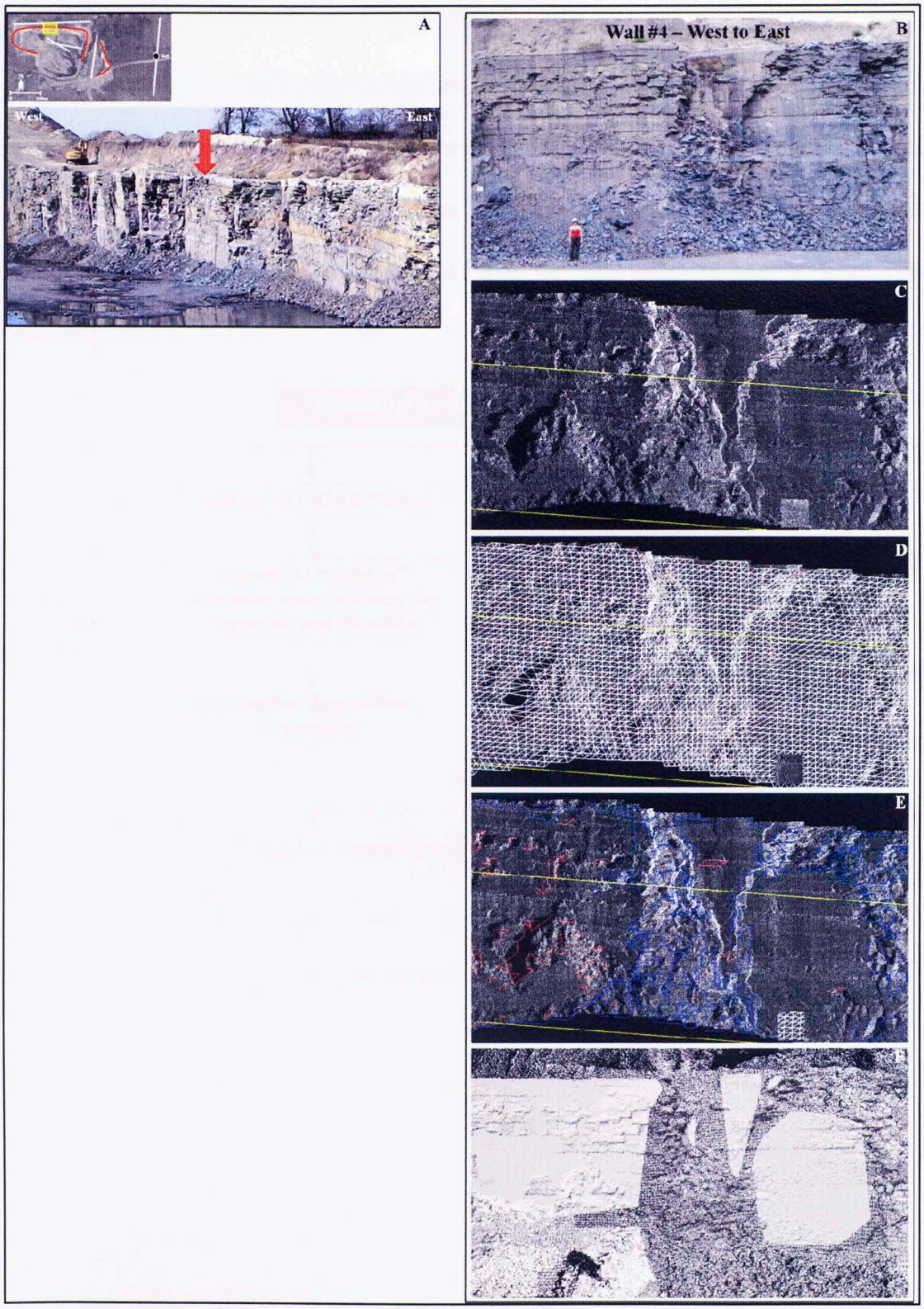

Figure 31. (A) Lateral view of Wall #4 pointing the location of "B" and showing the trend of the fracture planes, (B) Photo of east-west trending Wall #4. (C) View of point cloud from the same areas as "A" loaded into the first software, (D) Mesh of the rock surface from the point cloud generated automatically by a software, (E) Fracture patches identified by software (red outlines are areas within a patch that are not part of the planar patch outlined) (F) Point cloud loaded into the second software that allows fracture planes to be picked manually.

2.2 Workflow

Figure 32 shows the entire workflow, which includes the analysis of all the data mentioned above and the comparison of results. The well logs, seismic, and lidar data were loaded into the seismic interpretation software to have all the data in one place. However, this kind of software does not have the capability to handle large point clouds.

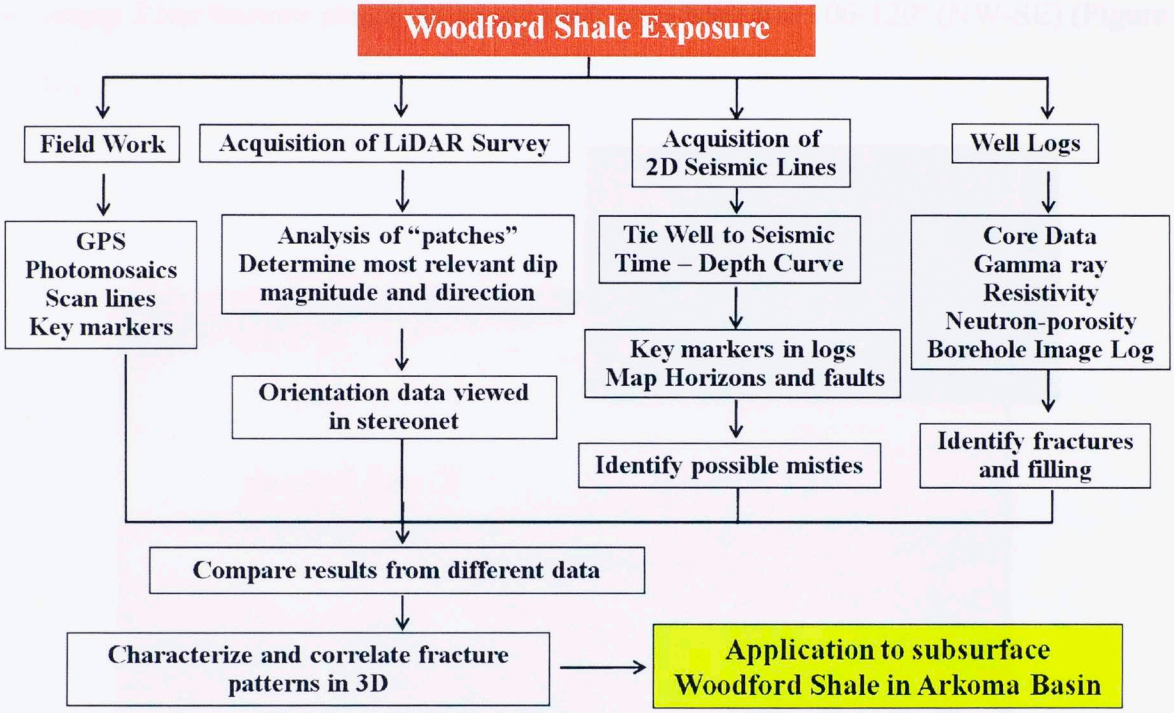

Figure 32. Workflow followed to complete the research.

3. RESULTS

3.1 Fracture measurements on quarry floor

The fracture planes measured in the scan lies on the outcrop floor were grouped into 15° strike intervals (Figure 33, 34 and Appendix 11):

- Group 1 has fracture planes striking 76-90° (ENE-WSW) and 91-105° (WNW-ESE), with spacing between 15 to 50cm (6 to 18inches).
- Group 2 has fracture planes striking 31-45° (NE-SW) and 106-120° (NW-SE) (Figure 35).

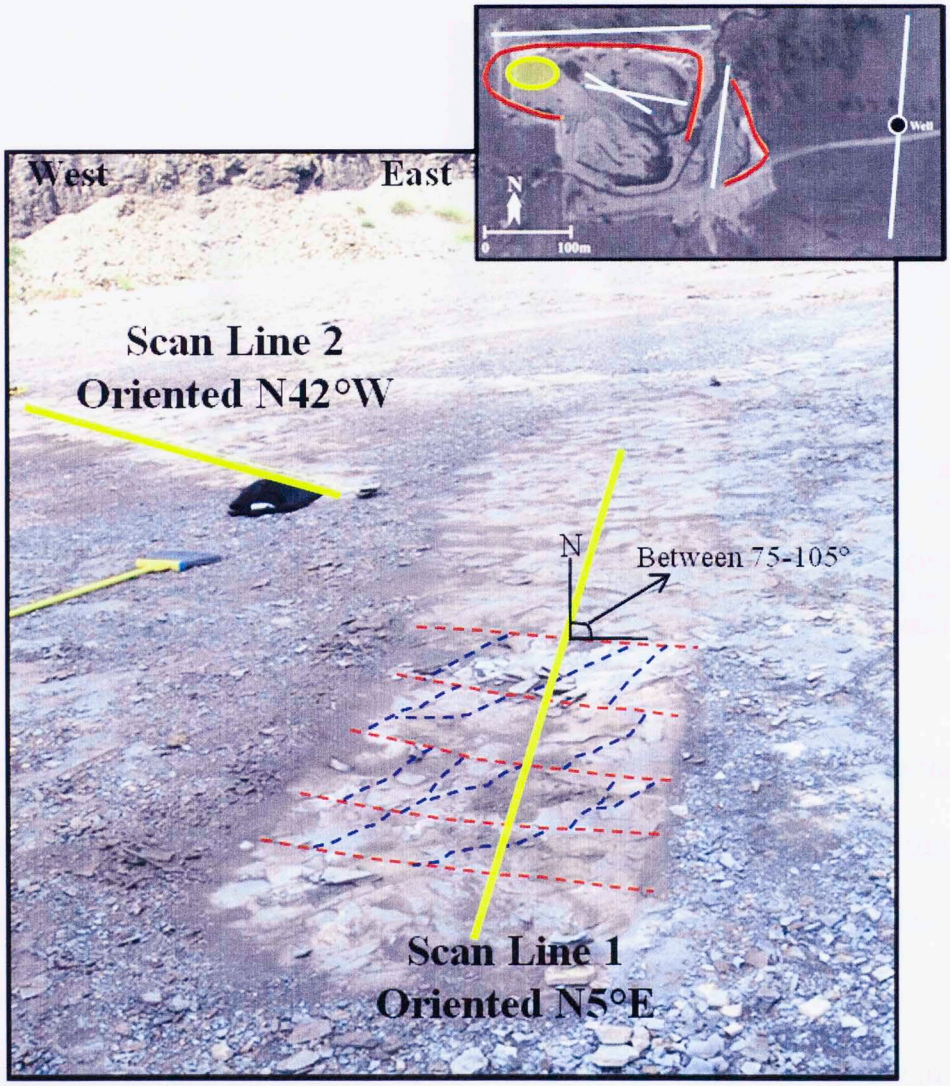

Figure 33. Scan lines #1 and 2 with Group 1 fractures being systematic highlighted in red, and Group 2 fractures being not systematic highlighted in blue.

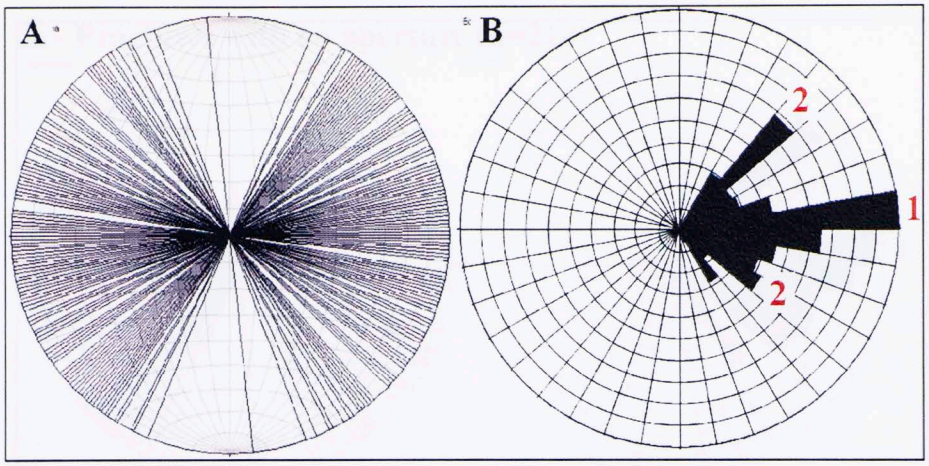

Figure 34. Fractures planes measured on Scan Line #1 and 2 (n=357), with group numbers.

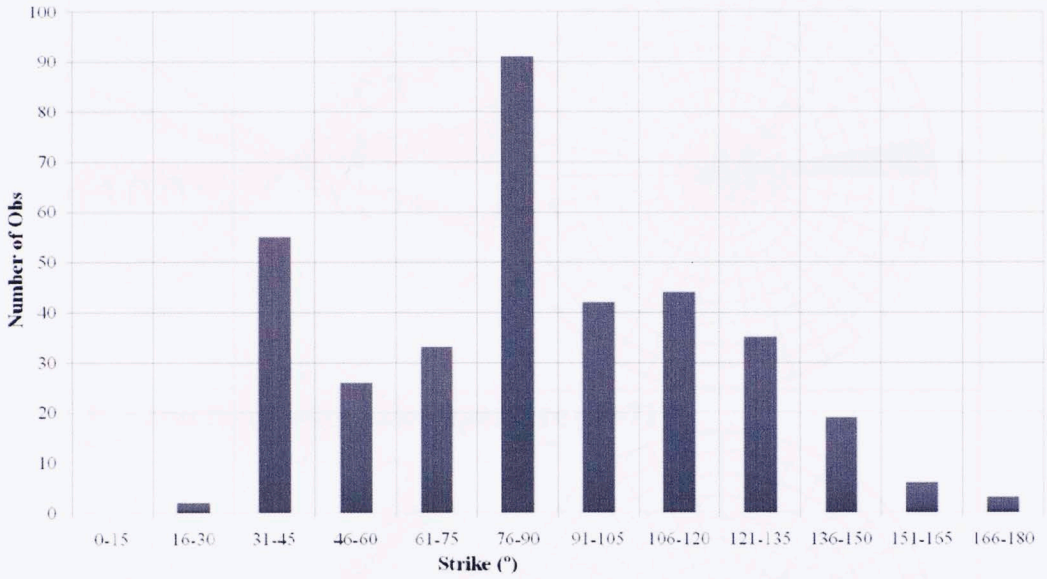

Figure 35. Histogram of fracture plane strikes measured on both scan lines (n=357). Observe that the majority of the fractures have a strike between 76-90° (ENE orientation), followed by fractures with strikes between 31-45° (NE direction), and fractures with strikes between 106-120° (NW direction).

The scan lines and core data were the only methods able to measure the size of the fracture apertures, as well as the filling material. They were classified in three types: no aperture, open aperture, and filled (mineralized) aperture (Figures 36). The quantity of fractures every 15° interval into the different classes is listed in Appendix 12 (Figure 37). Results indicate that the majority of the fractures with filled aperture are in Group 1 (strike 76-90° (ENE-WSW)).

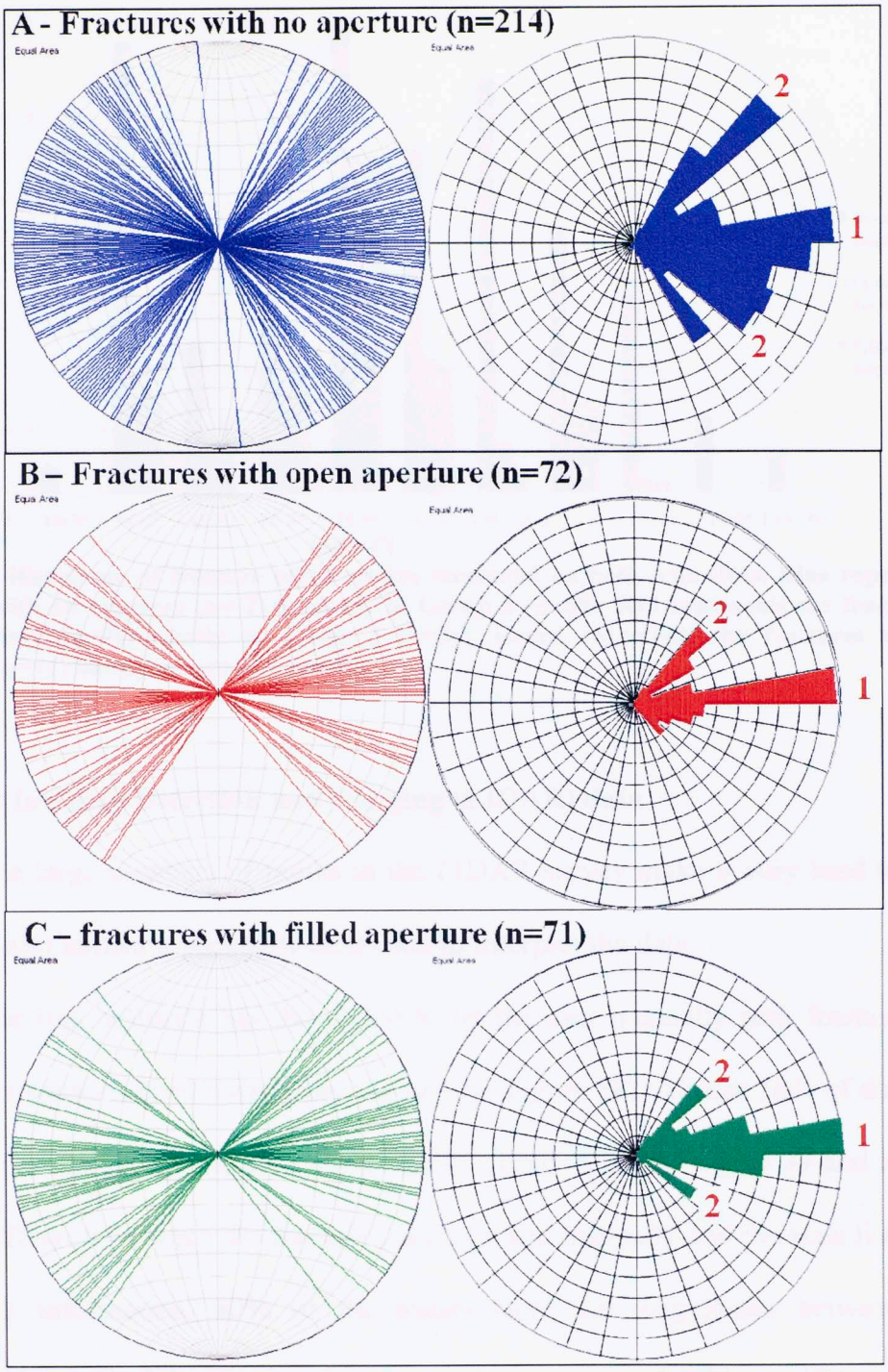

Figure 36. Fracture planes in Scan Lines divided in classes: (A) Fractures with no aperture (n=214), (B) Fractures with open aperture (n=72), and (C) Fractures with filled aperture (n=71). Group numbers are shown.

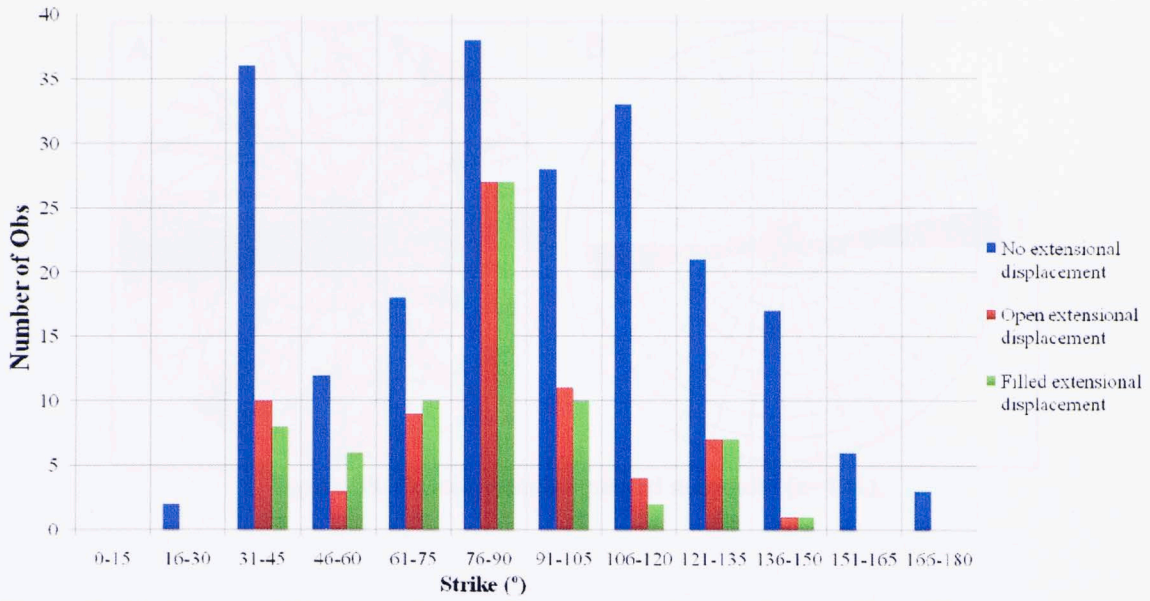

Figure 37. Histogram of fracture plane strikes measured on both scan lines. Blue represents the fractures with no aperture (n= 214) mostly in Group 2 (n=69). Red represents the fractures with open aperture (n=72) mostly in Group 1 (n=56). Green represents the fractures with filled apertures (n=71) mostly in Group 1 (n=37).

3.2 Laser Imaging Detection and Ranging (LIDAR) data

The large numbers of points in the LIDAR survey make it very hard to handle. Two different software packages were used to interpret the data.

The first software has the option to let the user manually pick fracture planes. 131 planes were mapped throughout the survey (Figure 38). Almost 50% of the fracture planes are in Group 1 (strikes between 76-90° (ENE-WSW)) (Figure 39 and Appendix 13). A difference between the fracture planes picked manually and the scan lines planes is the dip information, 80% of the planes have dip magnitudes between 76-90° following the vertical fracture pattern seen on the outcrop walls (Figure 40).

Figures 41, 42, and 43 are images of the LIDAR data on different walls, showing the west-east trend of the majority of the fractures (Group 1).

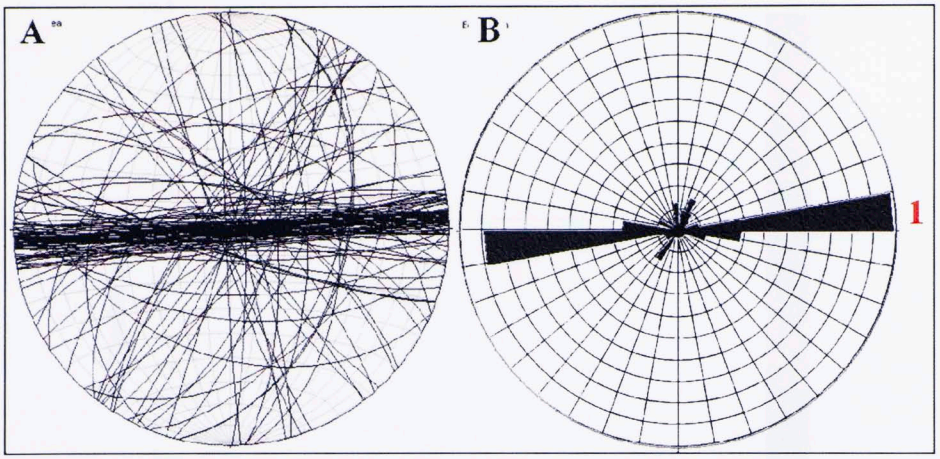

Figure 38. Fracture planes picked manually (n=131).

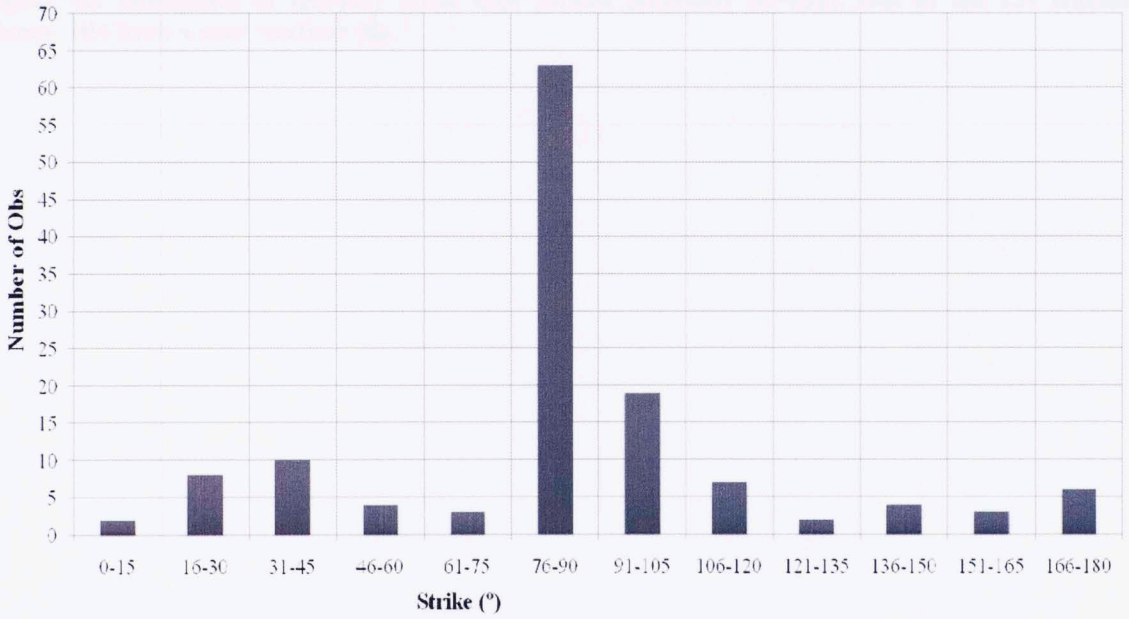

Figure 39. Histogram of fracture plane strikes picked manually (n=131). The majority of the fractures are in Group 1.

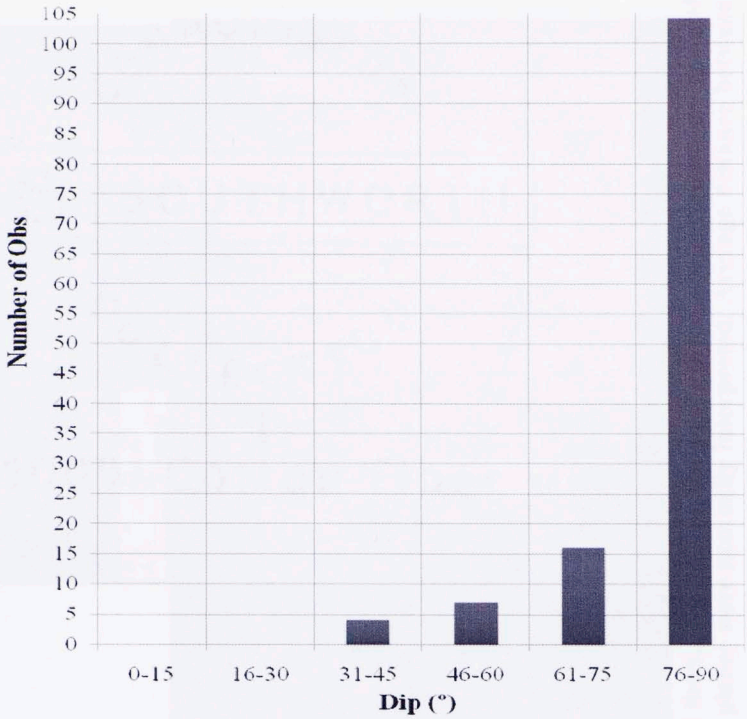

Figure 40. Histogram of fracture plane dips picked manually (n=131). Out of the 131 fracture planes, 104 have a near vertical dip.

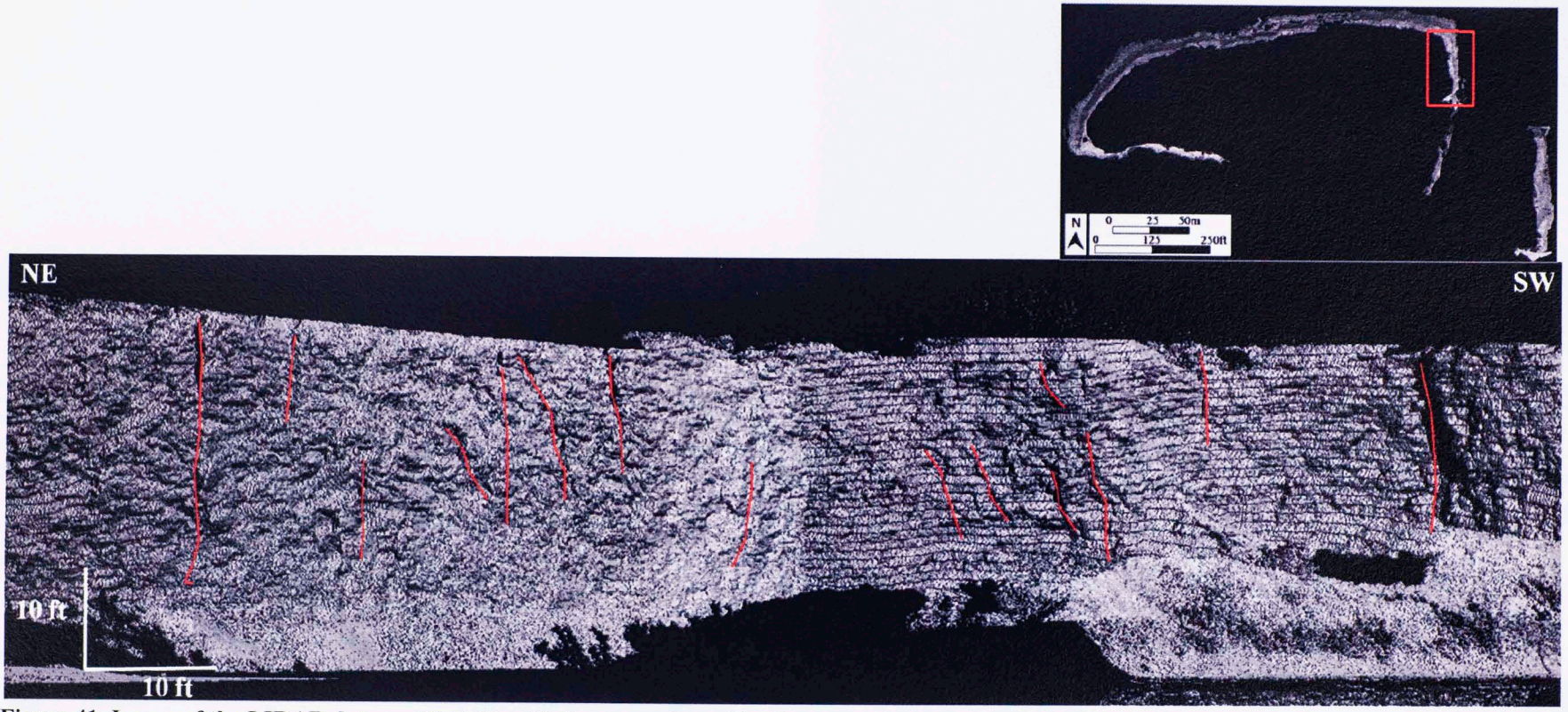

Figure 41. Image of the LIDAR data on Wall #3, with fracture planes highlighted with red lines. Most of the fractures planes interpreted have a vertical dip and a west-east strike, like Group #1. On 20m (65ft) horizontal distance, 15 fracture planes were manually interpreted. Average distance between fractures is 1.5m (4ft).

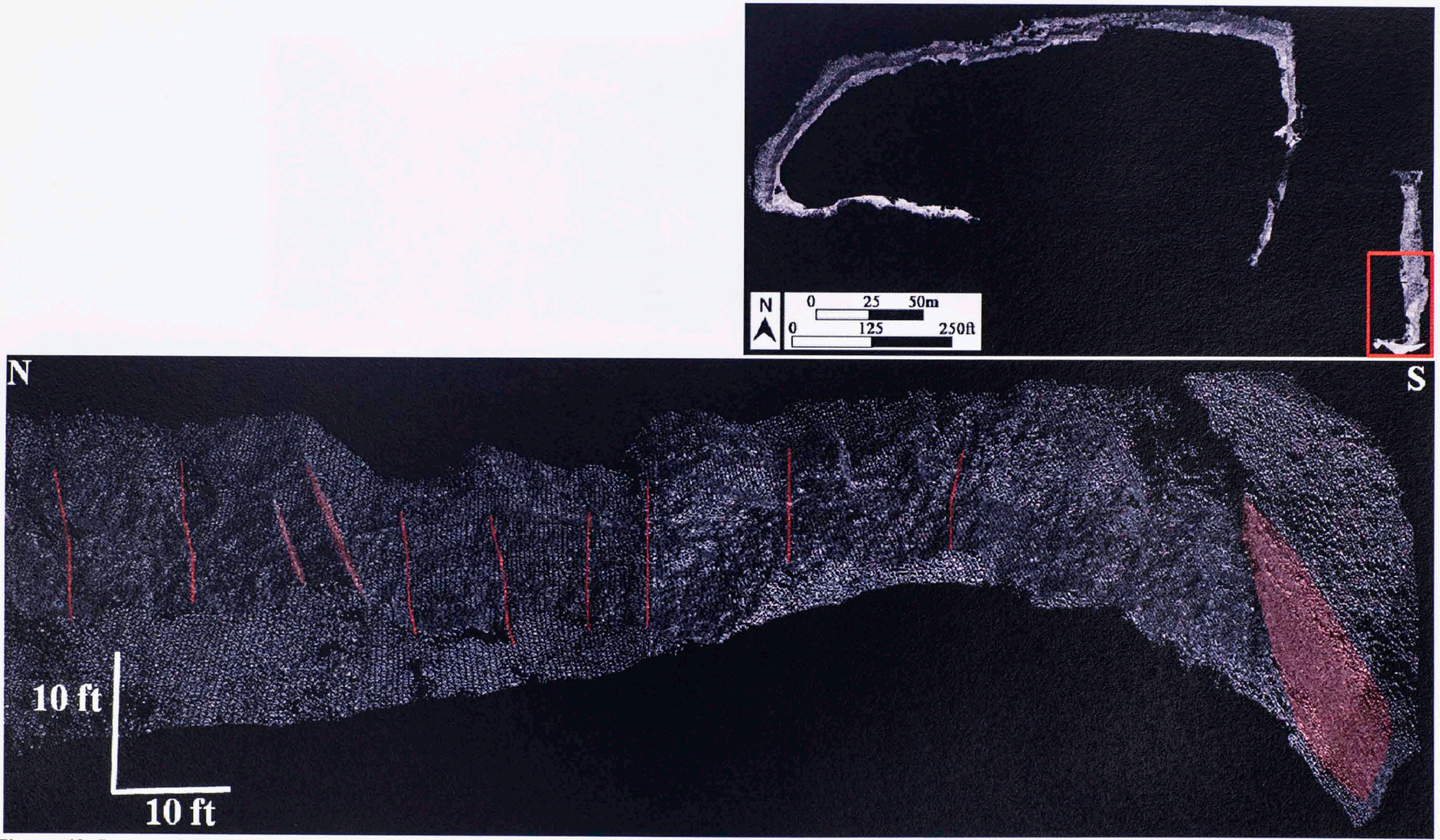

Figure 42. Image of the LIDAR data on Wall #2 and 1, with fracture planes highlighted with red lines. Most of the fractures interpreted have a vertical dip and a west-east strike, like Group #1. On 14m (45ft) horizontal distance, 11 fracture planes were manually interpreted. Average distance between fractures is 1.5m (4ft).

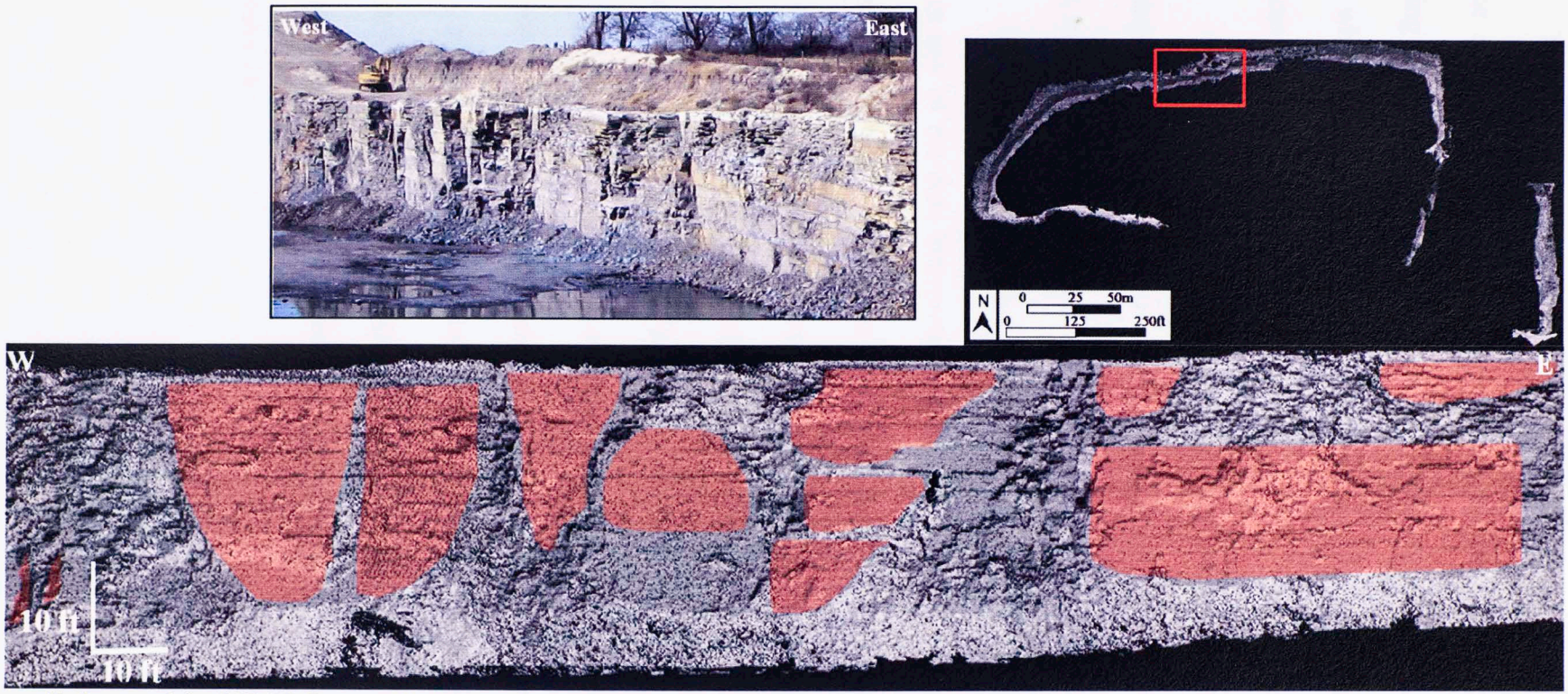

Figure 43. Image of the LIDAR data on Wall #4, with fracture planes highlighted with red planes. Most of the fractures interpreted have a vertical dip and a west-east strike, like Group #1. On 14m (45ft) horizontal distance, 11 fracture planes were manually interpreted. For further understanding refer to figure 31.

The other software automatically performs rock mass fracture characterization on the survey by creating a mesh, calculating the orientation of each triangle, and creating fracture patches with orientation, size and roughness estimation. This saves time when doing the interpretation, but adds error by taking into account random surfaces that may not be fracture planes.

A total of 5008 fracture planes were interpreted on the survey. After performing the statistical analysis, 48% of the data strikes between 31-90° with no major relevant value, making it hard to discriminate a dominant strike (Figure 44 and Appendix 14).

The majority of the planes were dipping between 31-70°, which is a pattern not seen in any of the data interpreted manually. Due to the possible errors added by the automatic interpretation, only the planes with high dips were considered as real fracture planes (n=280) (Figure 45). Results indicate that the majority of the fracture planes are in Group 1 (strike 76-90° (ENE-WSW)), followed by Group 2 (31-45° (NE-SW)) (Figure 46, 47, and Appendix 15).

Another quality control performed on the data was the roughness attribute on the data, which represents the smoothness of the fracture plane with a value between 0 and 1 (the higher the values, the smoother the surface). The number of fracture planes dipping between 76-90° and roughness values ranging from 0.8 to 1 are 93 (Figure 48). Results indicate the same number of fracture planes in Group 1 and 2 (Figure 49 and Appendix 16).

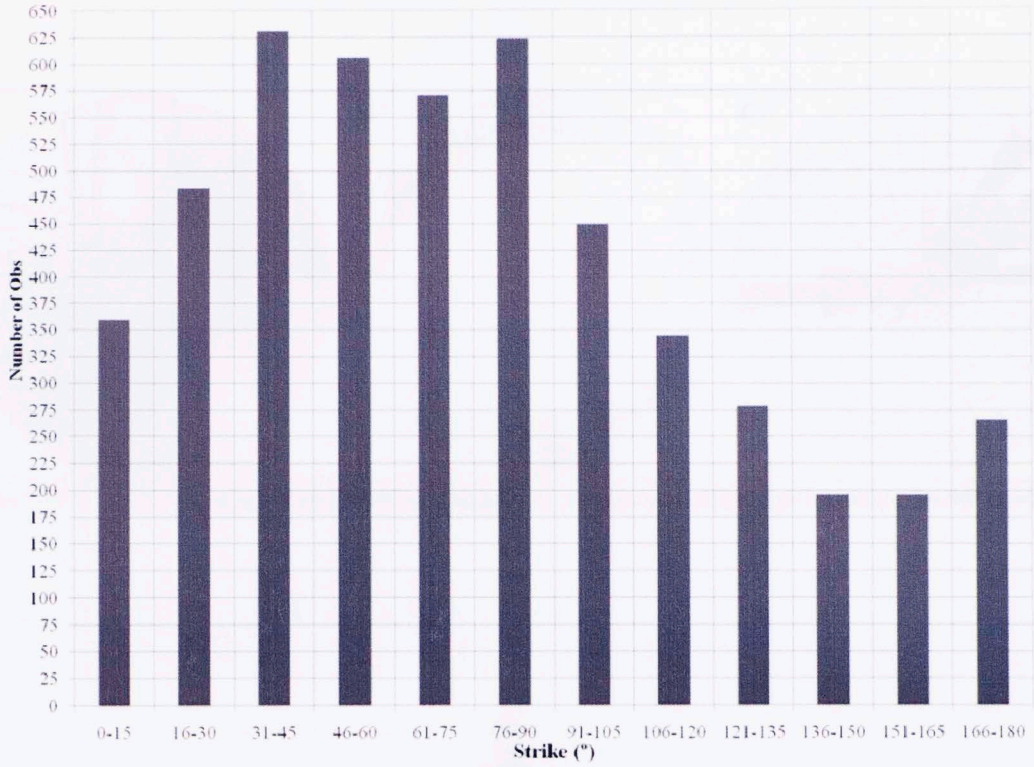

Figure 44. Histogram of fracture plane strikes picked automatically by a software (n=5008). Observe the difficulty to discriminate a dominant strike direction.

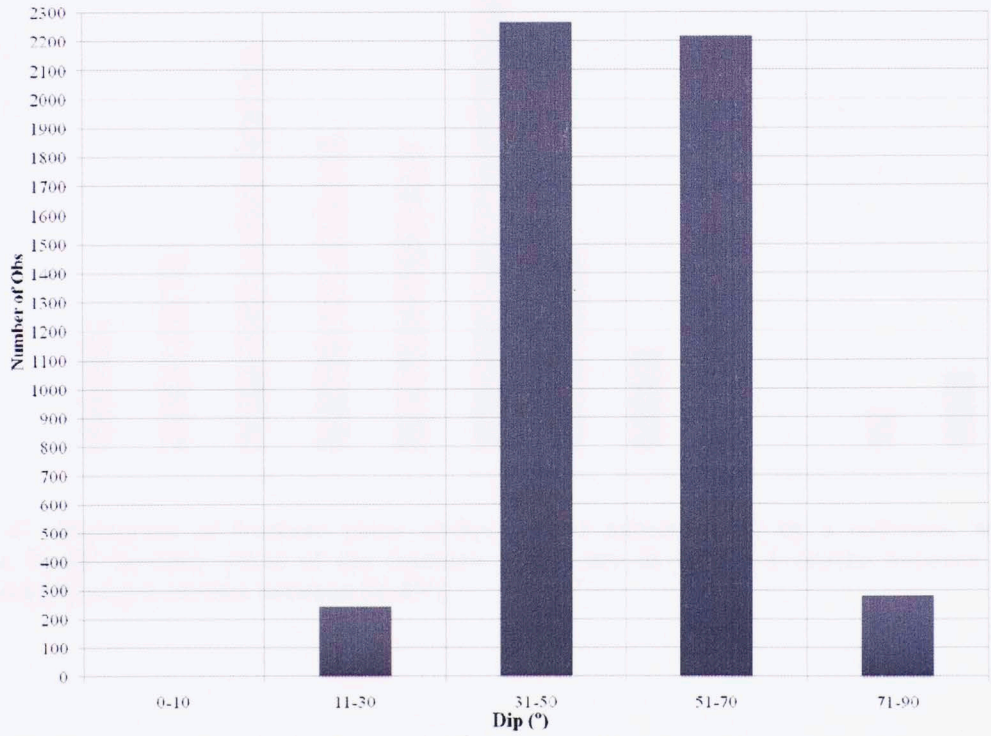

Figure 45. Histogram of fracture dips picked automatically by a software (n=5008). The greatest amounts of planes have dips between 31 to 70°.

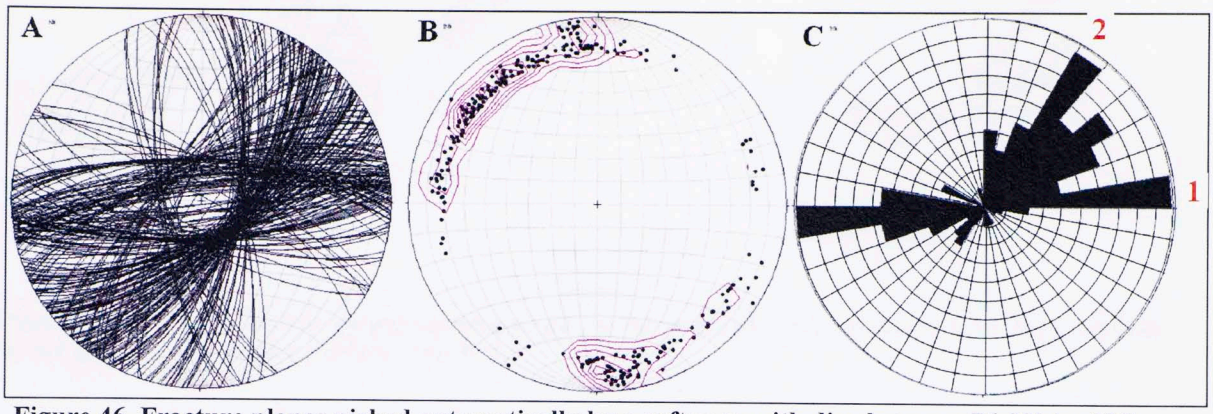

Figure 46. Fracture planes picked automatically by a software with dips between 76-90° (n=280).

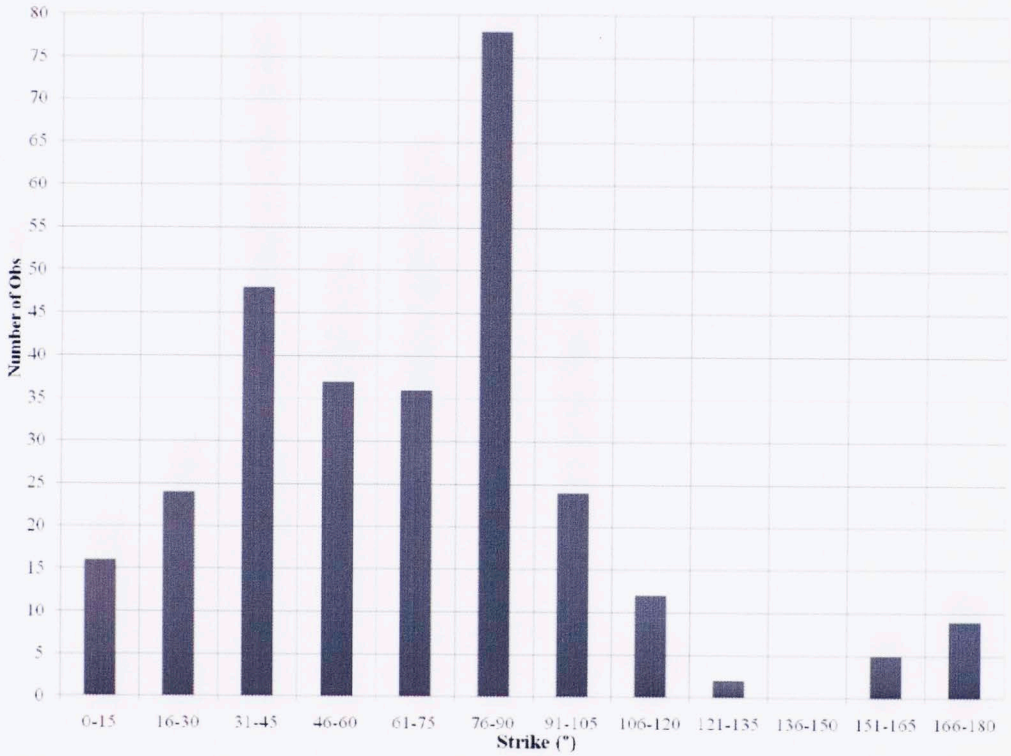

Figure 47. Histogram of fracture plane strikes picked automatically by a software, with dips between 70-90° (n=280). Most of the fracture planes are in Group 1 (strike between 76-90°), followed by Group 2 (strikes between 31-45°).

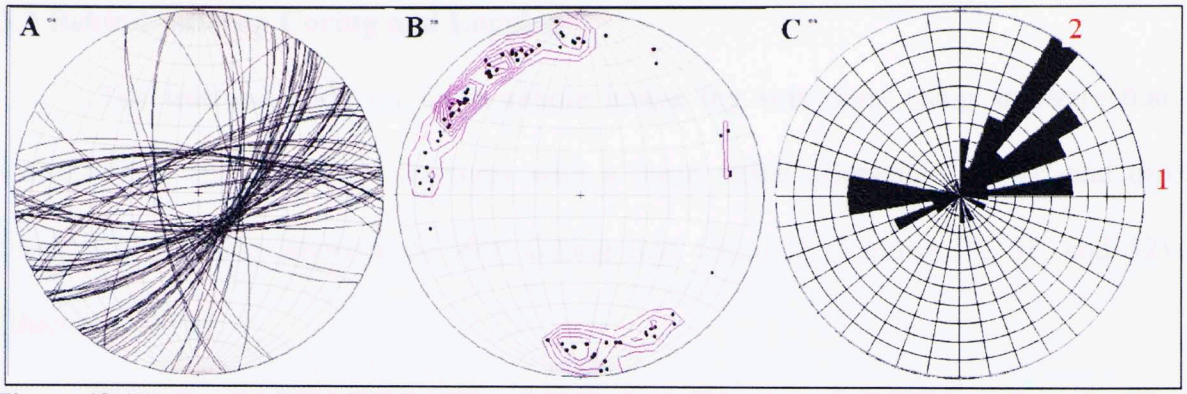

Figure 48. Fracture strikes picked automatically using interpretation software with dips between 70-90° and roughness between 0.8-1 (n=93).

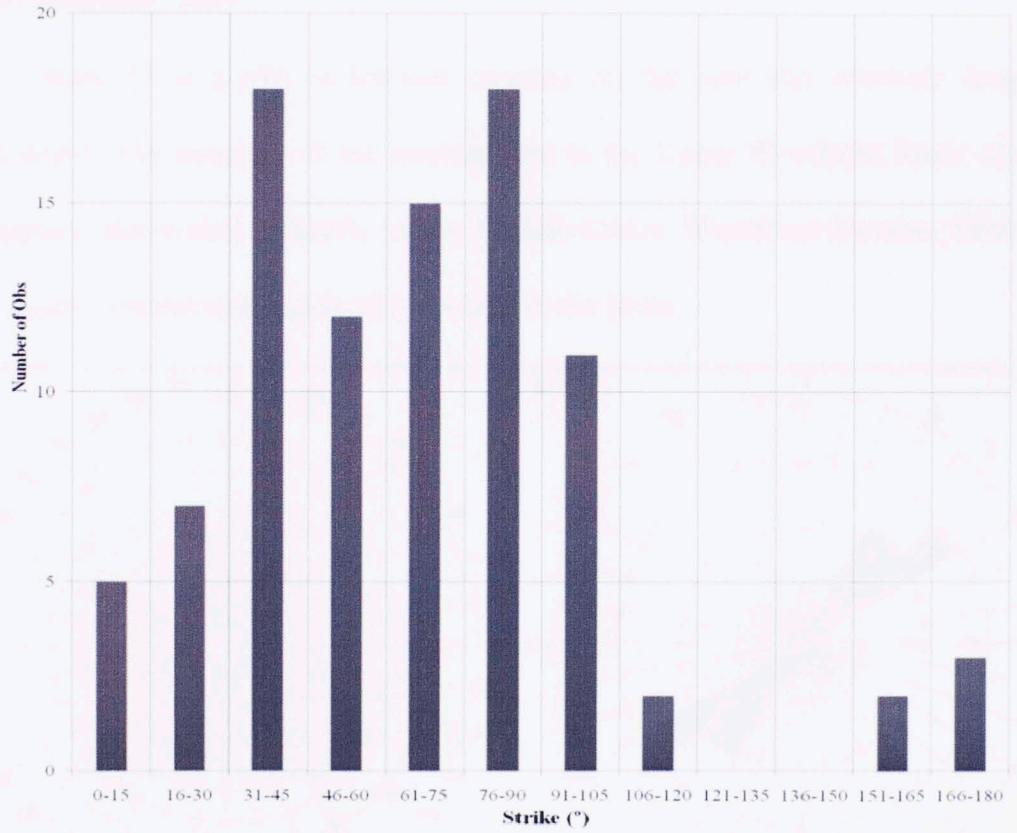

Figure 49. Histogram of fracture planes strikes picked automatically by a software with dips between 70-90° and roughness between 0.8-1 (n=93). Most of the fracture planes strike between 76-90, followed by 31-45.

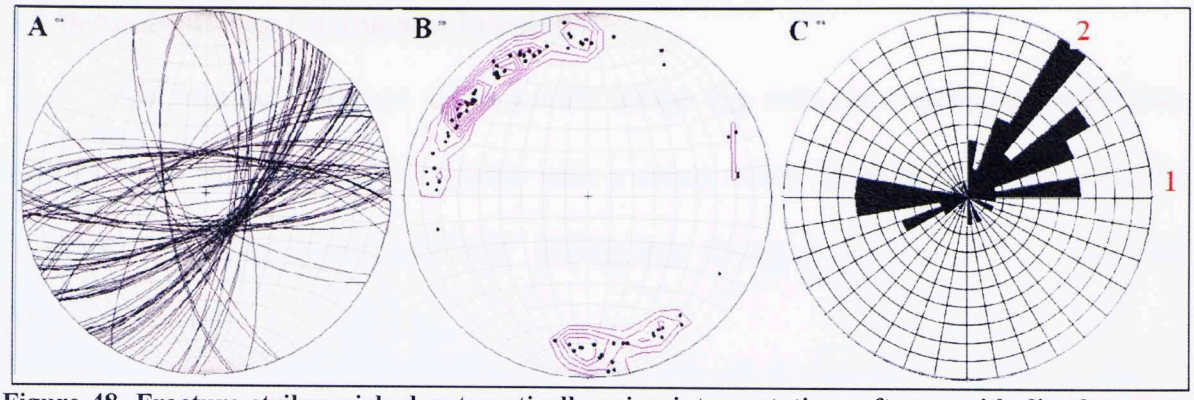

Figure 48. Fracture strikes picked automatically using interpretation software with dips between 70-90° and roughness between 0.8-1 (n=93).

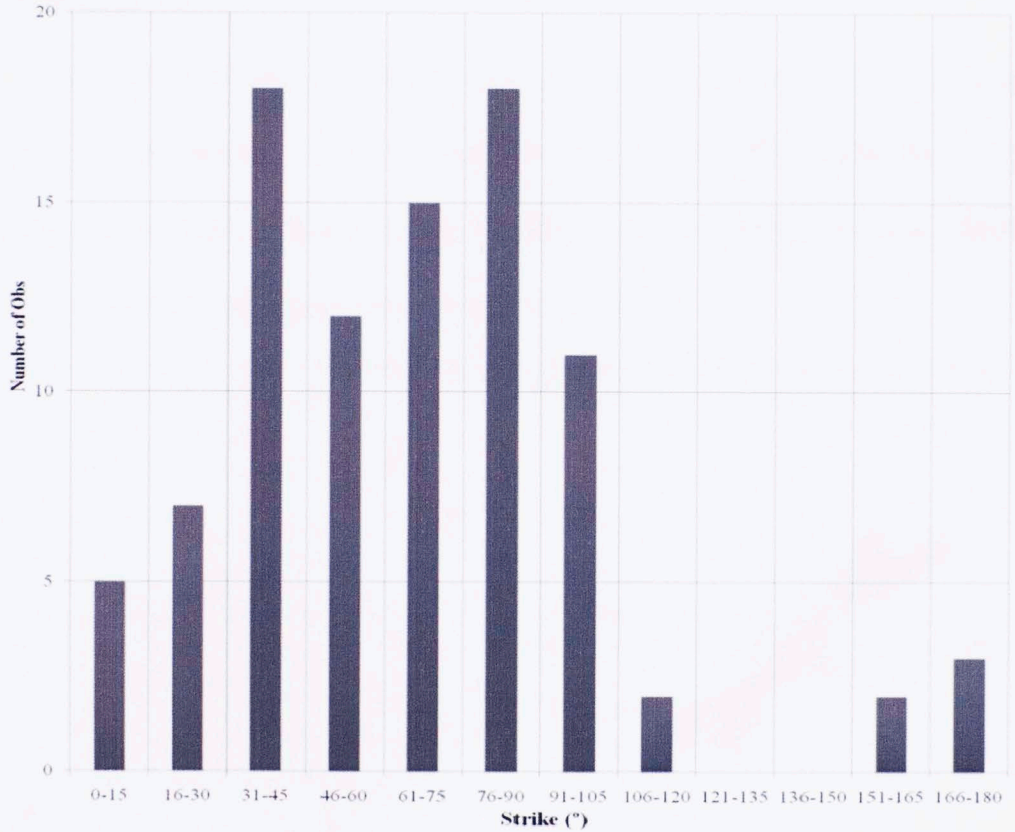

Figure 49. Histogram of fracture planes strikes picked automatically by a software with dips between 70-90° and roughness between 0.8-1 (n=93). Most of the fracture planes strike between 76-90, followed by 31-45.

3.3 Behind-outcrop Coring and Logging

The fracture study on the borehole image log was done using software that automatically interpreted 14 fractures with a mean strike orientation of 50° and dip magnitudes ranging between 51°-90° falling into Group 2 (Figures 50, 51, and 52) (Buckner, 2009).

A total of 69 fractures were identified in the core, described as jagged, thin (often less than 2mm in thickness), healed, vertically discontinuous (often only appearing for 2.5-5cm (1–2inches)), and zigzagging at lithologic boundaries (Figure 51 and 52) (Buckner, 2009).

Figure 53 is a plot of fracture quantity on the core and borehole image log versus depth. The majority of the fractures are in the Upper Woodford Shale Member, the quantity diminishes radically in the Middle-Lower Woodford Member because of lower quartz content and higher clay content in the latter.

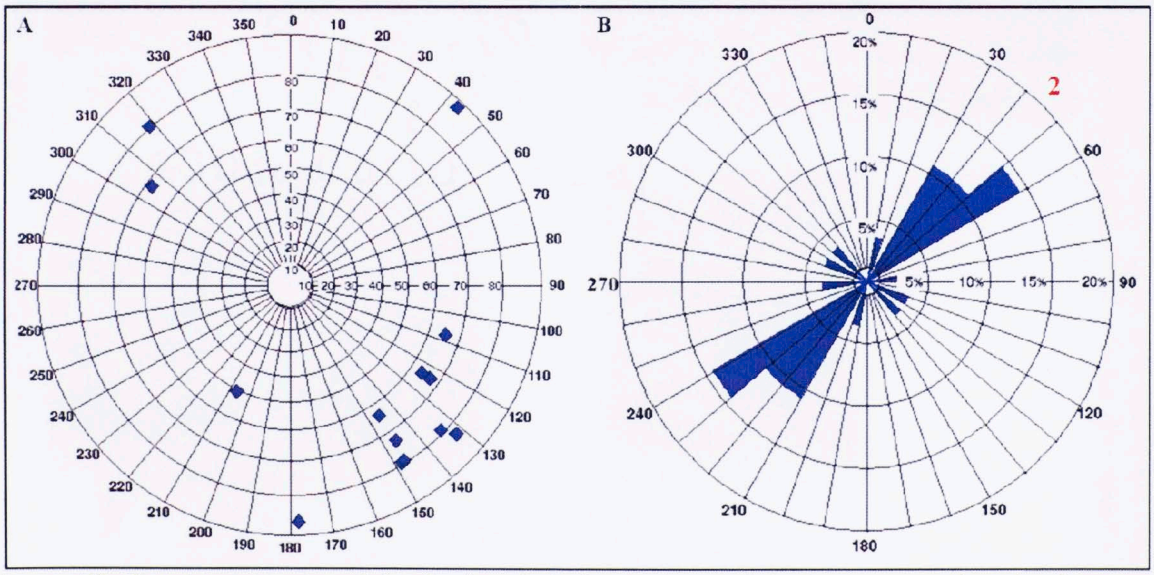

Figure 50. Fractures measured in the borehole image log. (A) Poles representing the fractures strike and dip magnitudes, (B) Fractures strike plotted on a rose diagram (n=14). All fractures appeared to be healed, and none were planar features cutting through the entire wellbore. The mean strike orientation is N50°E-S50°W, with dip magnitudes ranging between 51°-99° (average dip of 77.5° at 140° azimuth) (Buckner, 2009).

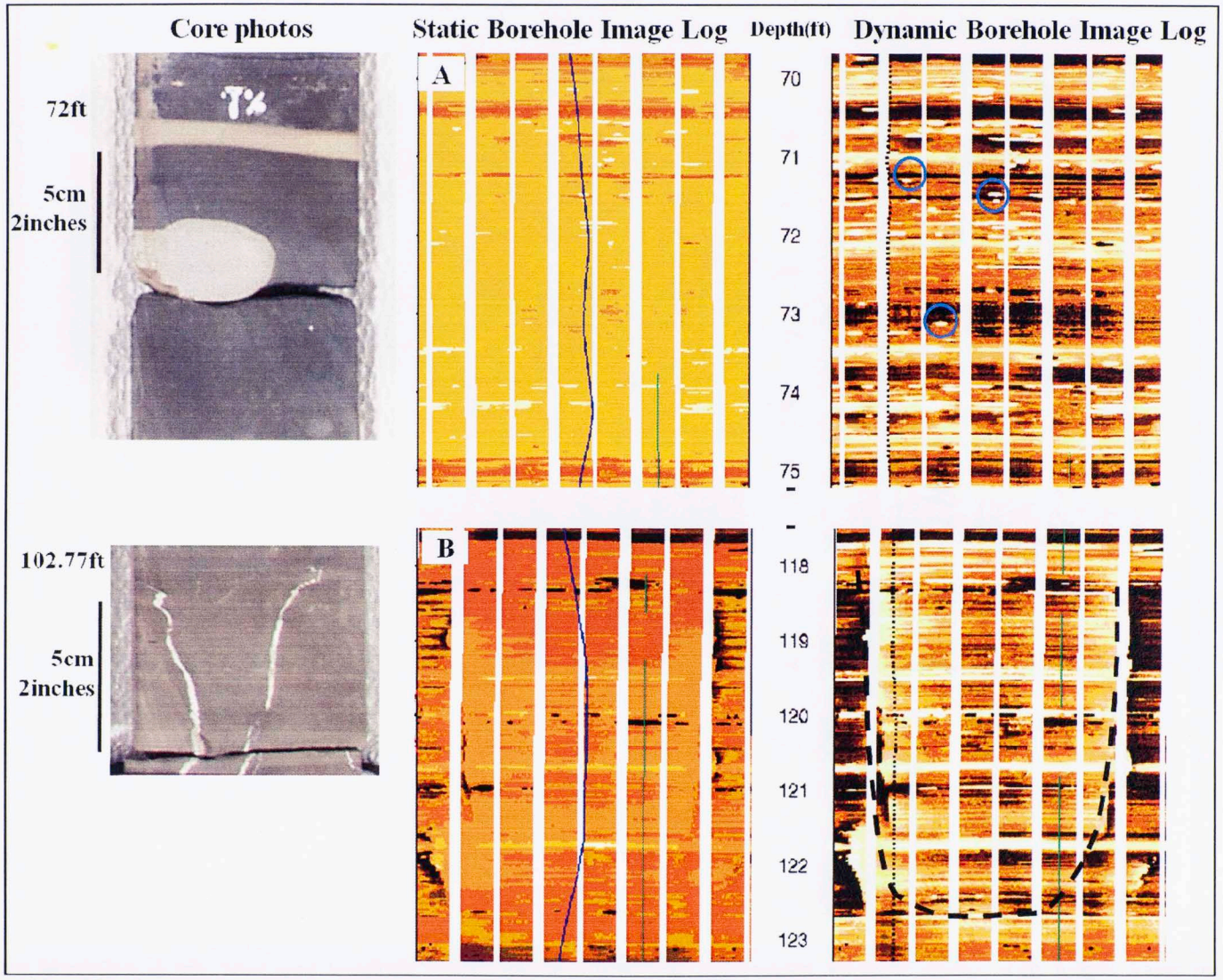

Figure 51. Features identified in the core and borehole image log, (A) Phosphatic nodules are bright ovals in the borehole image log, (B) Fractures in core and borehole image log (notice how the fractures are healed in the core) (core images modified from Buckner, 2009).

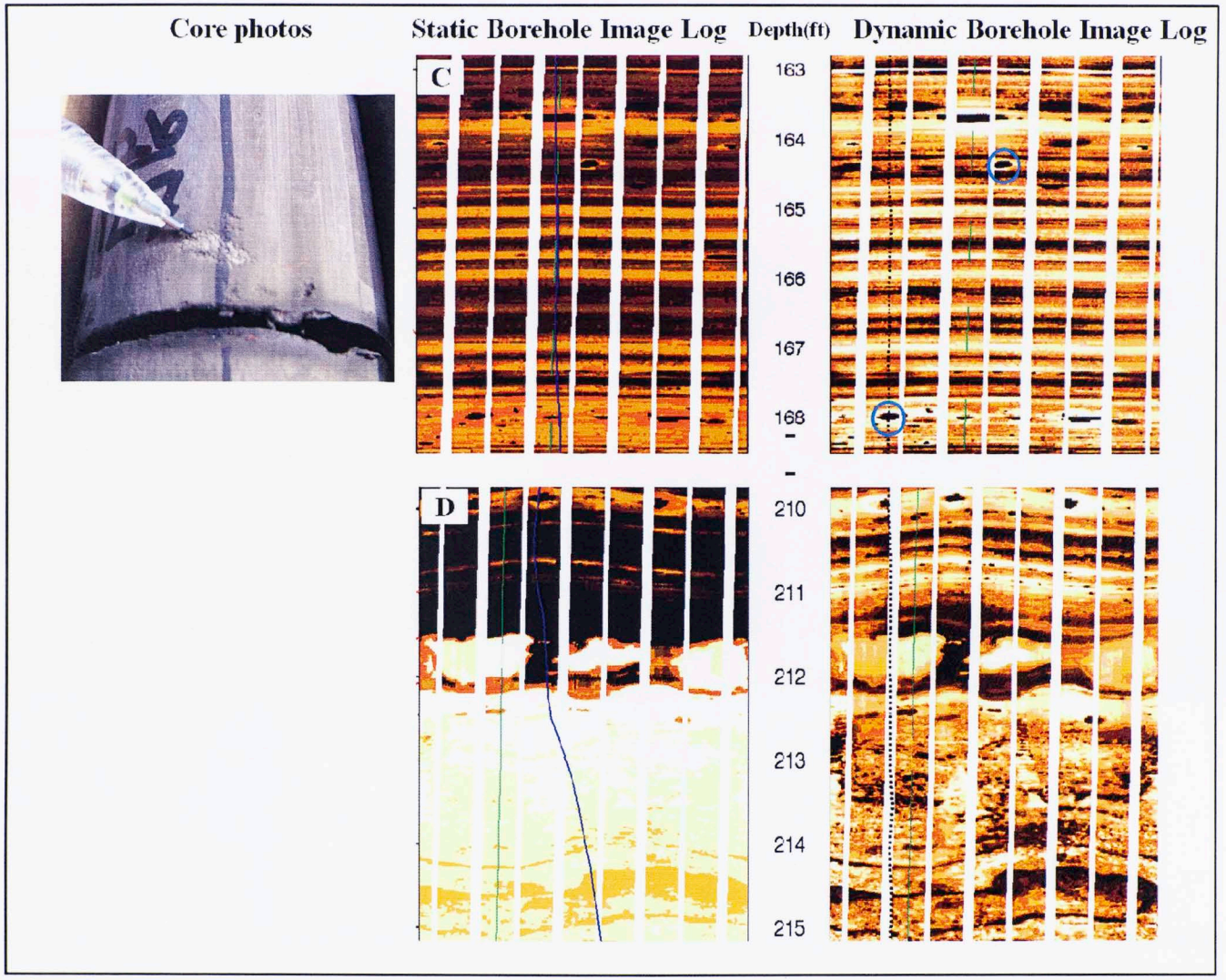

Figure 52. Features identified in the core and borehole image log, (C) Pyrite is represented as dark circles with bright halos in the log, and (D) Unconformity between Woodford-Hunton (darker color represents most conductive material, lighter color represents most resistive material) (core images modified from Buckner, 2009).

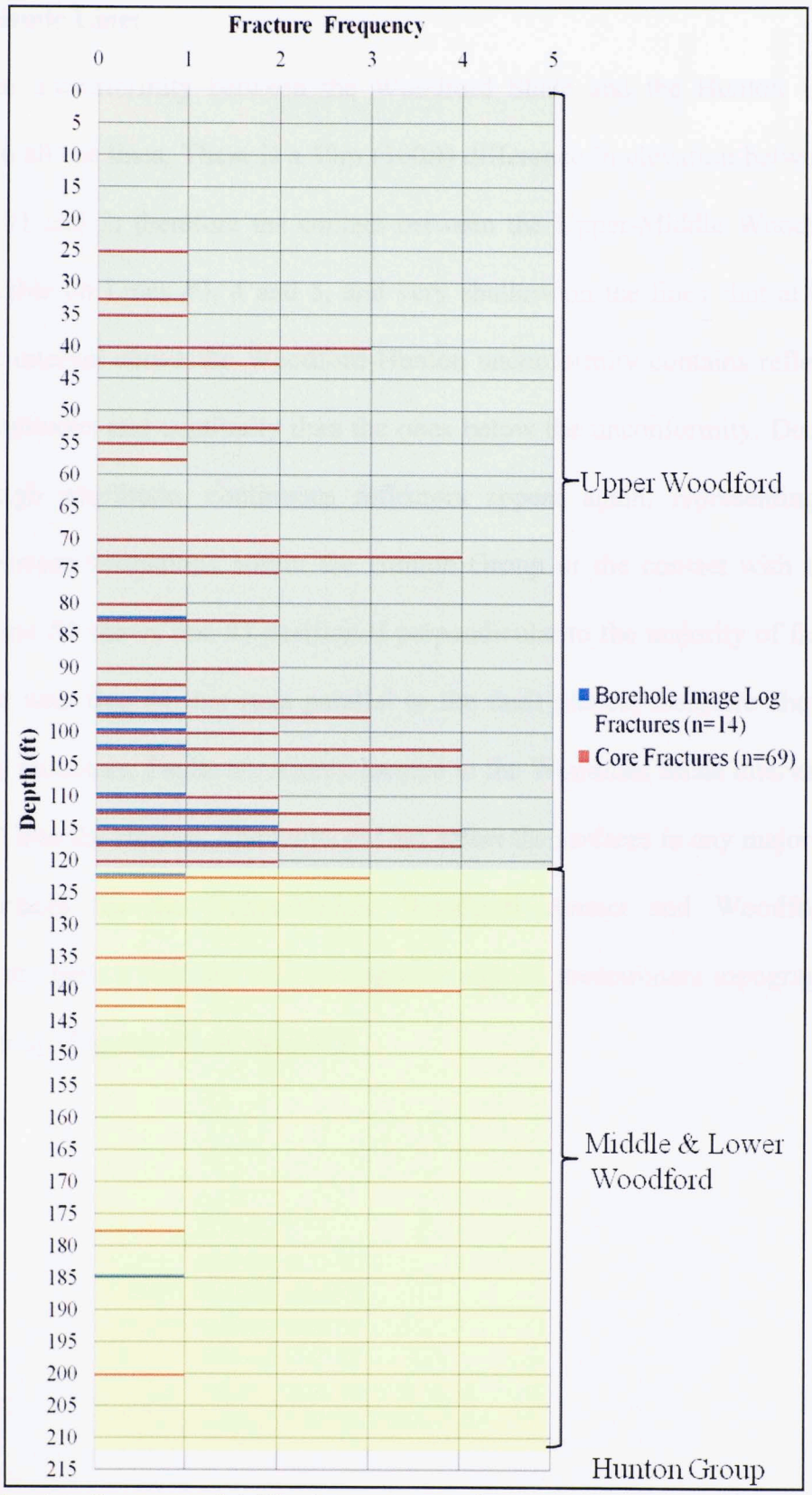

Figure 53. Fracture frequency plot. Blue bars represent fractures in the Borehole image log and red bars represent fractures in the core. The majority of the fractures are in the Upper Woodford member. Data obtained from Buckner, 2009.

3.4 2D Seismic Lines

The unconformity between the Woodford Shale and the Hunton Group was mapped on all the lines. There is a 30m (100ft) difference in elevation between line #5 and lines #1 and 2; therefore the contact between the Upper-Middle Woodford Shale was mappable on Lines #3, 4 and 5, and very shallow on the lines shot at the quarry floor. The interval above the Woodford-Hunton unconformity contains reflectors with higher amplitudes and continuity than the ones below the unconformity. Deeper in the section, high amplitude, continuous reflectors appear again, representing either a contact between formations within the Hunton Group or the contact with the Sylvan Shale. Figure 54 shows line #5 positioned perpendicular to the majority of fault planes, in contrast with line #4 that runs parallel to the fault planes, therefore showing very continuous reflectors. Faults are mainly located in the Woodford Shale interval, but they can extend into the Hunton. The faults did not affect the surfaces in any major way.

Surfaces for the Upper-Middle Woodford contact and Woodford-Hunton unconformity have a NW dip with no apparent sign of predominant topography on the Hunton Group (Figures 55, 56, and 57).

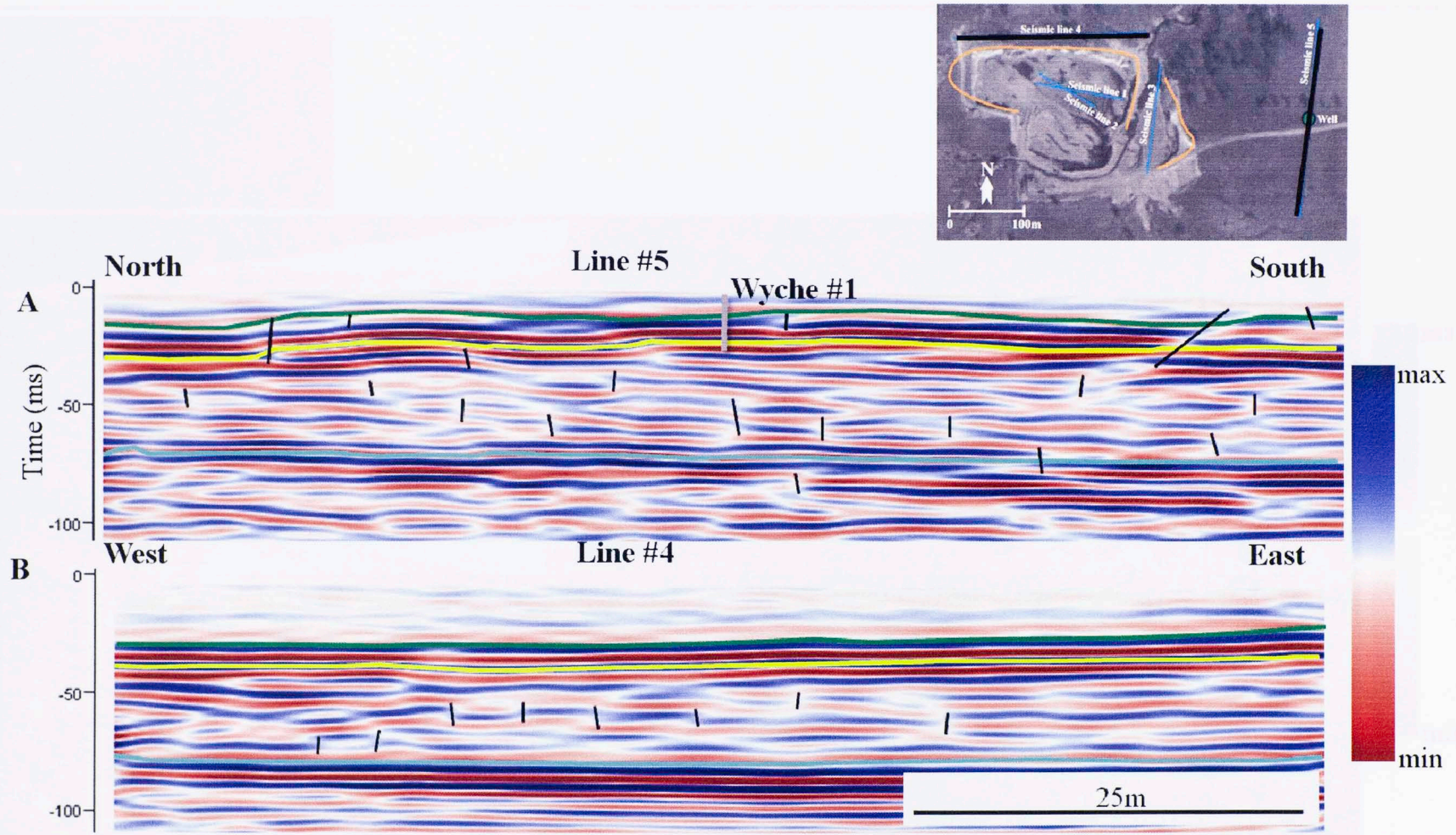

Figure 54. (A) Line #5 and (B) Line #4. The Upper-Middle Woodford contact is highlighted in green, and the Woodford-Hunton unconformity in yellow, as well as different faults and the position of well Wyche #1.

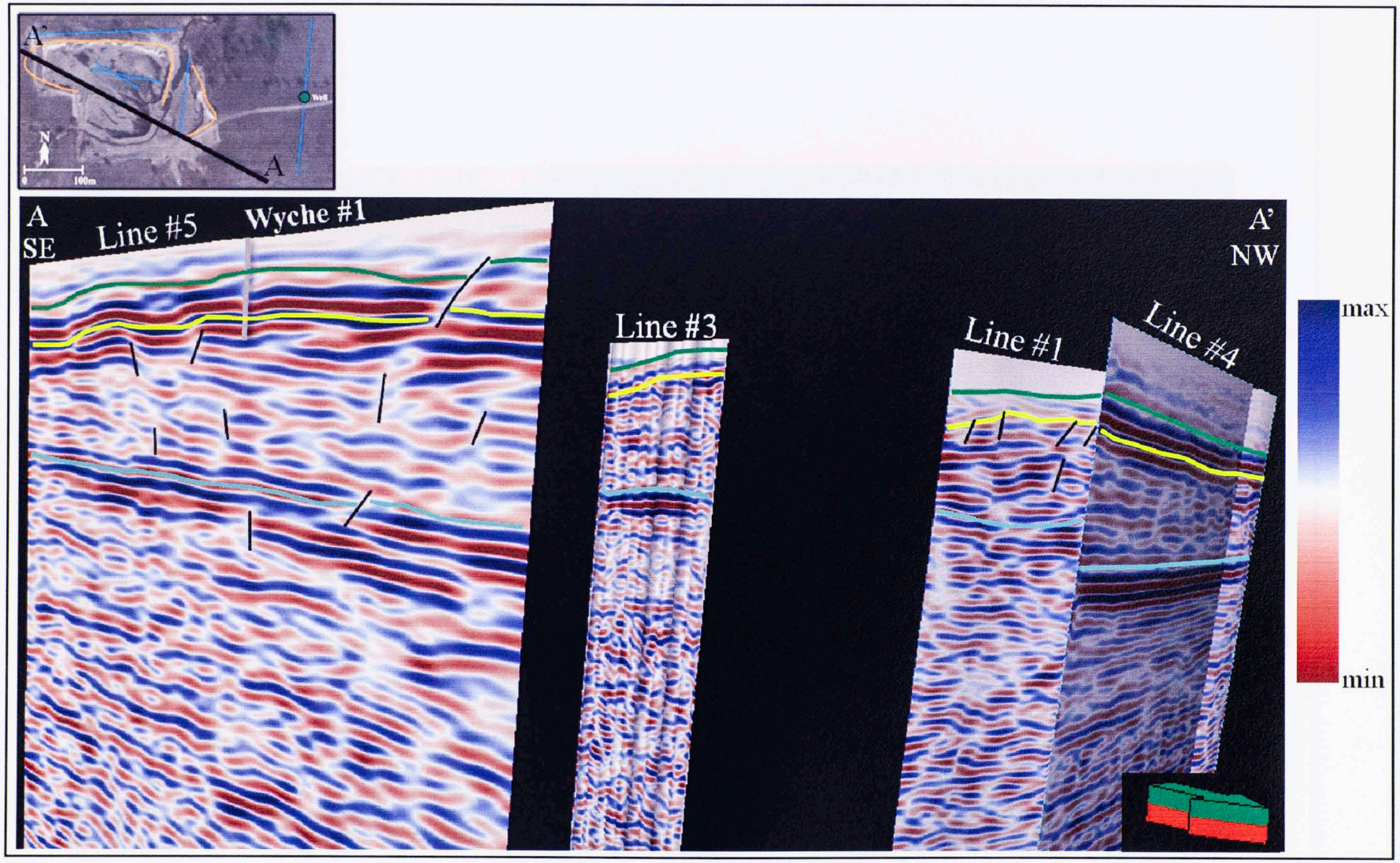

Figure 55. Lateral view of the 2D seismic lines shot at the Wyche Shale Pit, with horizons and faults interpreted. The Upper-Middle Woodford contact is highlighted in green, and the Woodford-Hunton unconformity in yellow, as well as different faults and the position of well Wyche #1.

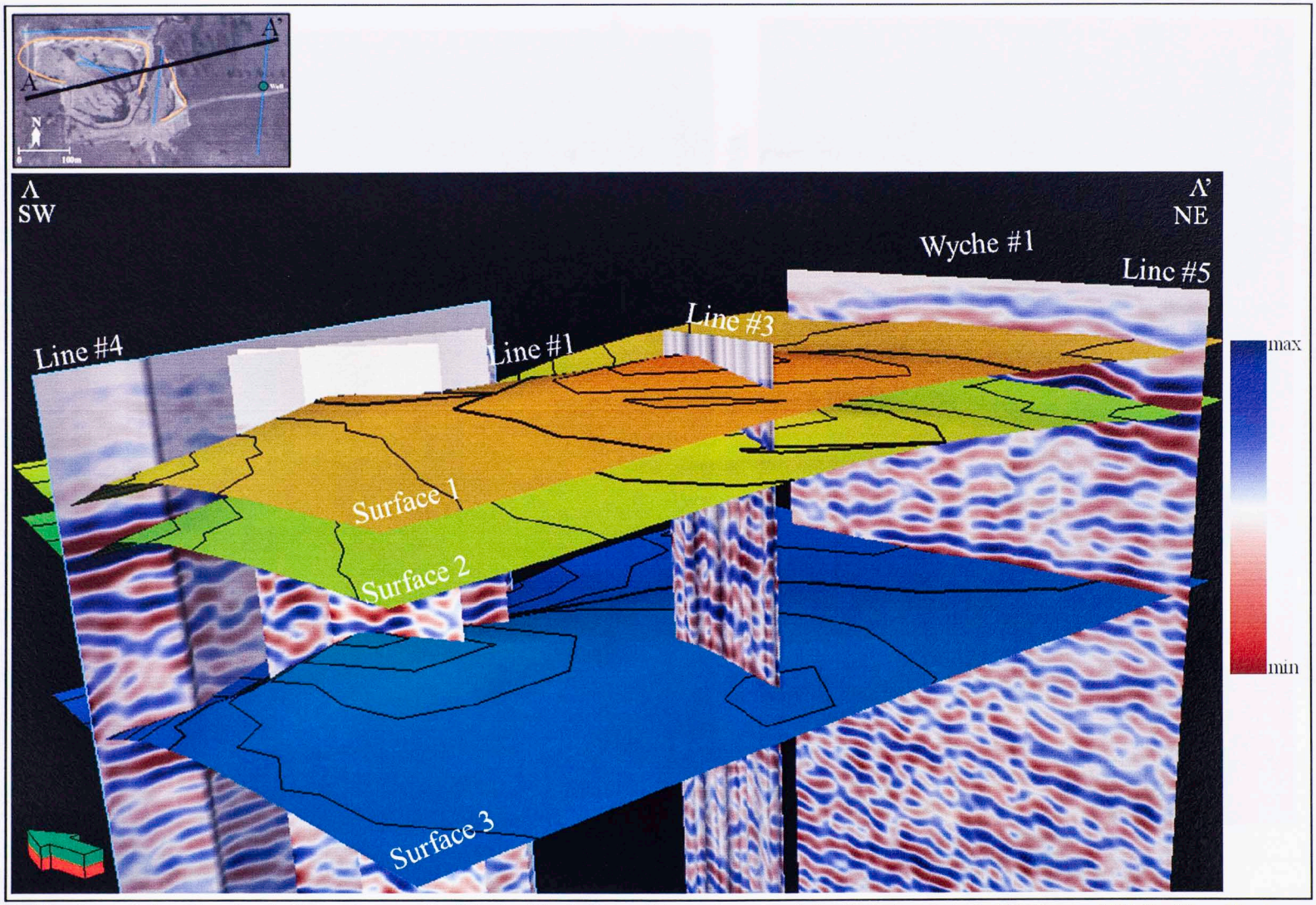

Figure 56. 3D view of the 2D seismic lines shot at the Wyche Shale Pit, with surfaces and faults interpreted. (1) Upper-Middle Woodford contact, (2) Woodford-Hunton unconformity, and (3) Possible contact between the Hunton Group and the Sylvan Shale.

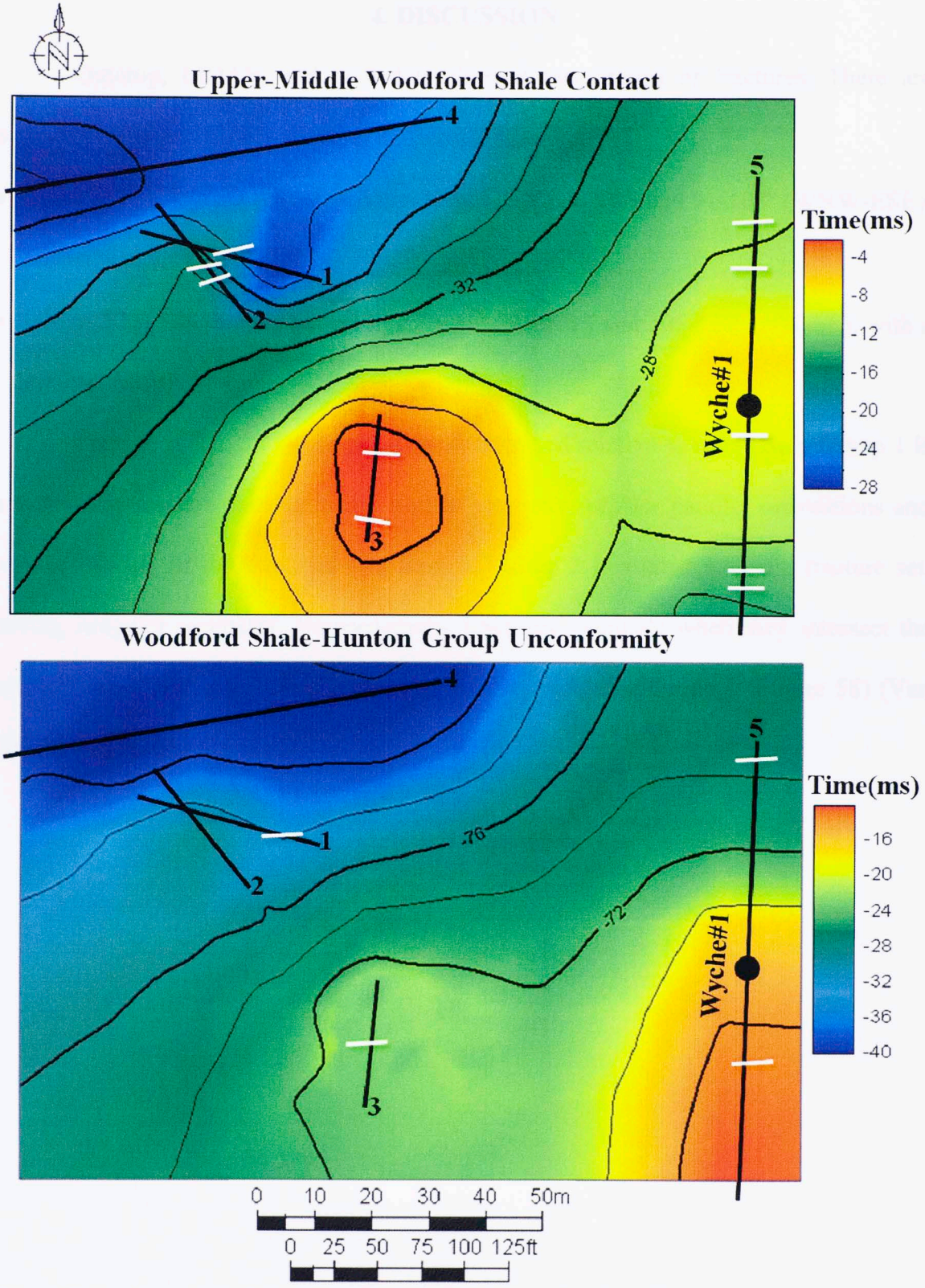

Figure 57. Isochron maps for the Upper-Middle Woodford Shale Member contact and Woodford-Hunton unconformity with position of 2D seismic lines, well, and faults that cut through them. Map units are in ms. Contours are every 2ms. Keep in mind that the interpolation may not be precise due to the distance between lines.

4. DISCUSSION

Outcrop, LIDAR, and well data showed two groups of fractures. There are additional fractures planes showing no trend orientation:

- Group 1 has fracture planes striking 76-90° (ENE-WSW) and 91-105° (WNW-ESE), with a median value of 90°.
- Group 2 has fracture planes striking 31-45° (NE-SW) and 106-120° (NW-SE), with a median value of 45°.

The age of the fracture sets can be determined relative to each other. Group 1 is a systematic fracture set due to the similar geometry, regular parallel orientations and regular spacing of the fractures that form it. Group 2 is a nonsystematic fracture set, having irregular geometry. Nonsystematic fractures terminate when they intersect the primary set of fractures; therefore Group 2 is younger than Group 1 (Figure 58) (Van der Pluijm, 2003).

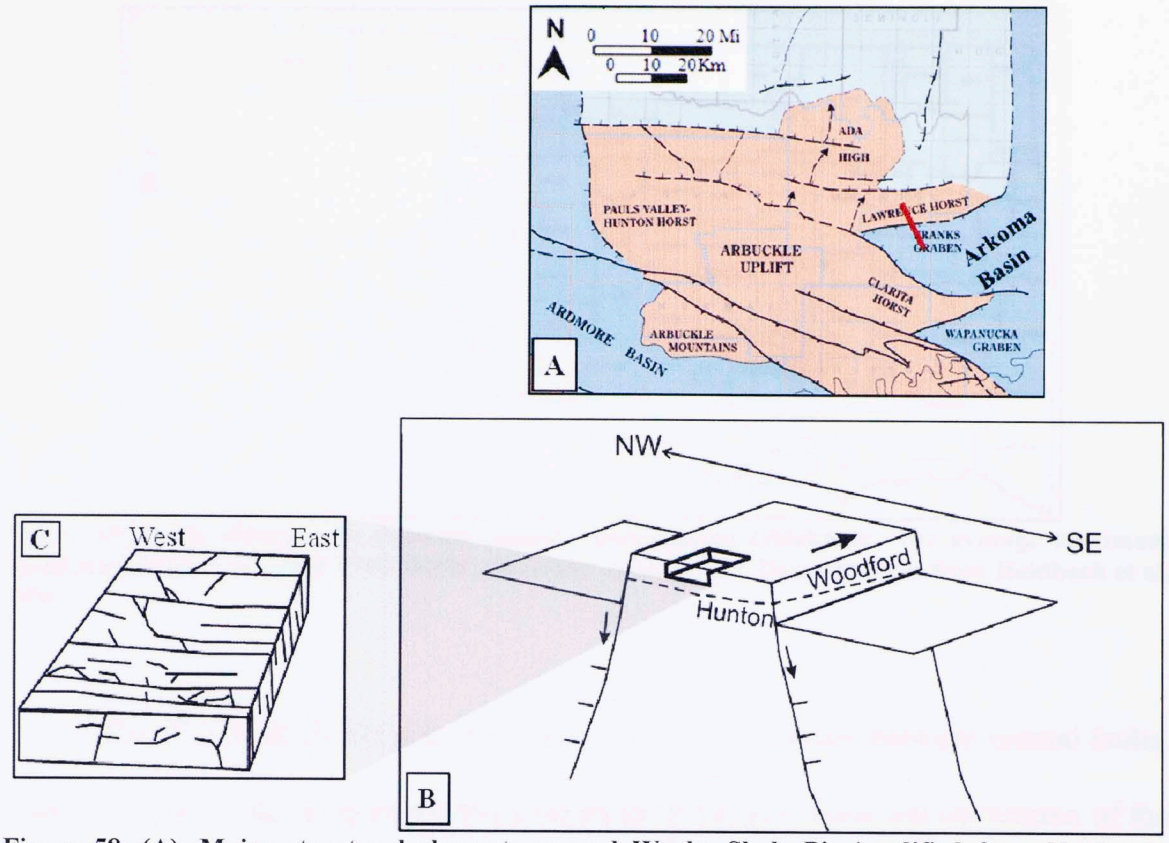

Figure 58. (A). Major structural elements around Wyche Shale Pit (modified from Northcutt, 1995), with location of cross-section. (B). Sketch cross-section showing structural position of the outcrop (not to scale). (C) Sketch block of Wyche Shale Pit showing systematic and nonsystematic fracture planes.

Fractures show the orientation of the stresses at the time of their formation (paleostresses or ancient stresses). Stresses may change orientation and magnitude through time, modifying the folding and faulting generated by the previous stresses (Lacazette, 2000). In the area of study, the present stress has an ENE-WSW direction, the same direction that generated Group 2 fractures (Figure 59).

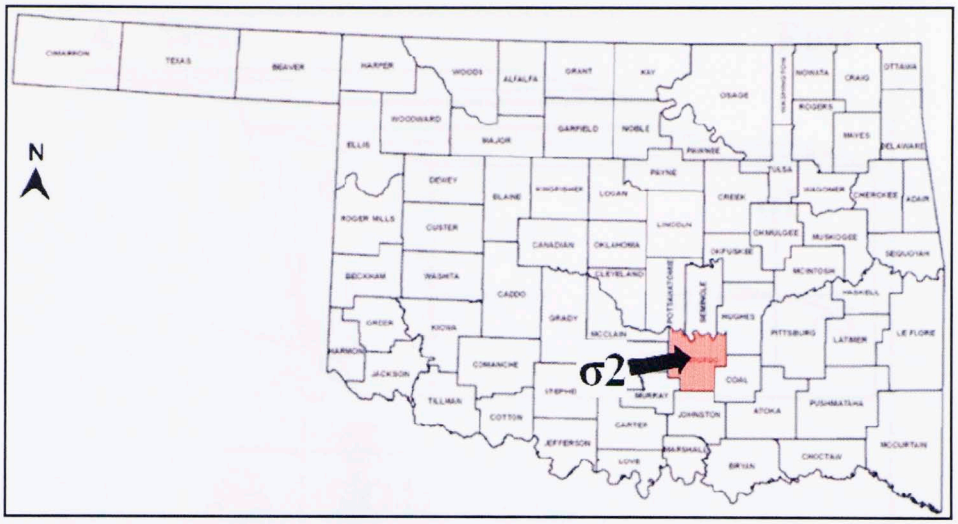

Figure 59. Stress direction in Pontotoc county, southeastern Oklahoma. The average maximum horizontal stress is oriented ENE-WSW, σ2 (error of up to 25°). Data obtained from Heidbach et al, 2008.

The Wyche Shale Pit is in the Lawrence Horst, contained between normal faults. There is a close relation between the orientation of fractures and the orientation of the stress field. The plane of an extensional fracture is perpendicular to σ3 (the minimum stress), parallel to σ2 (maximum horizontal stress), created by failure produced by σ1 (maximum vertical stress). The plane of the faults forms with an angle between σ1, ranging from 25-40°. In Andersonian regimes, the study area has a normal-faulting stress regime (Figure 60) (Lacazette, 2000).

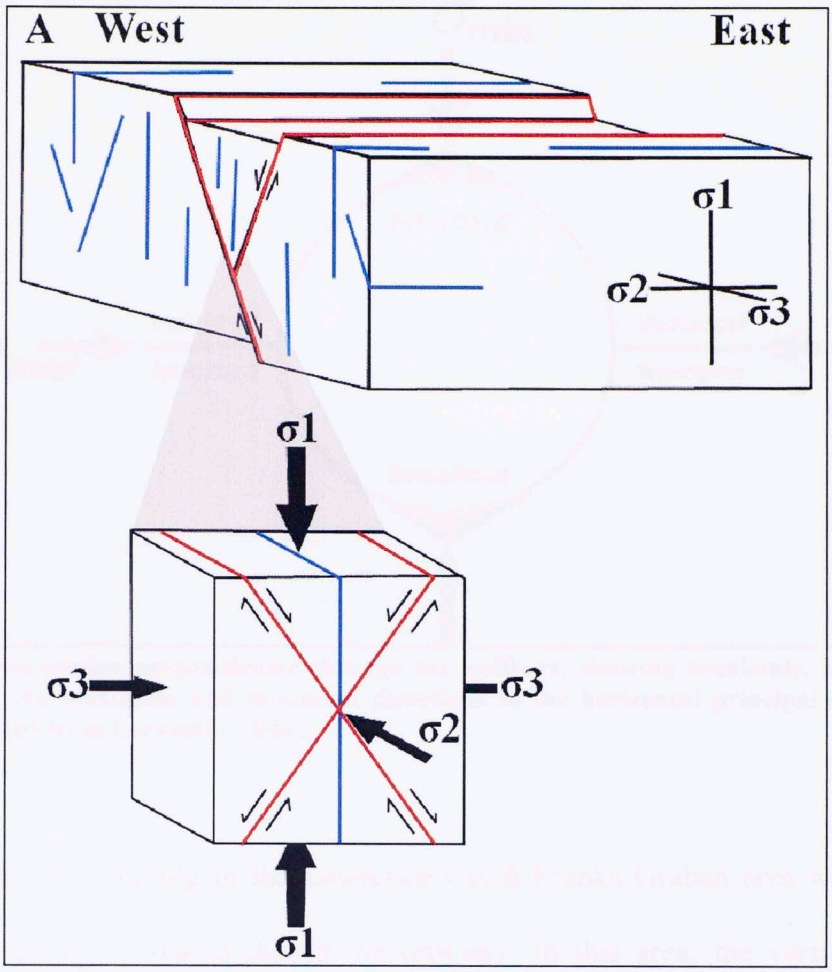

Figure 60. Relationship between fracture orientation and regional/local principal stresses in a normal faulting stress regime like the one present in the Wyche Shale Pit area. The fractures are represented in cyan, while the faults are in red (modified from Lacazette, 2000).

It is unlikely for a vertical well to cross through vertical fractures, this may be why no fractures from Group 1 are apparent in the Wyche #1 well. The borehole image log only showed incomplete, small fractures from Group 2. It is a shame that no drilling-induced fractures were generated because they would have had the same plane strike as the maximum horizontal principal stress (Figure 61).

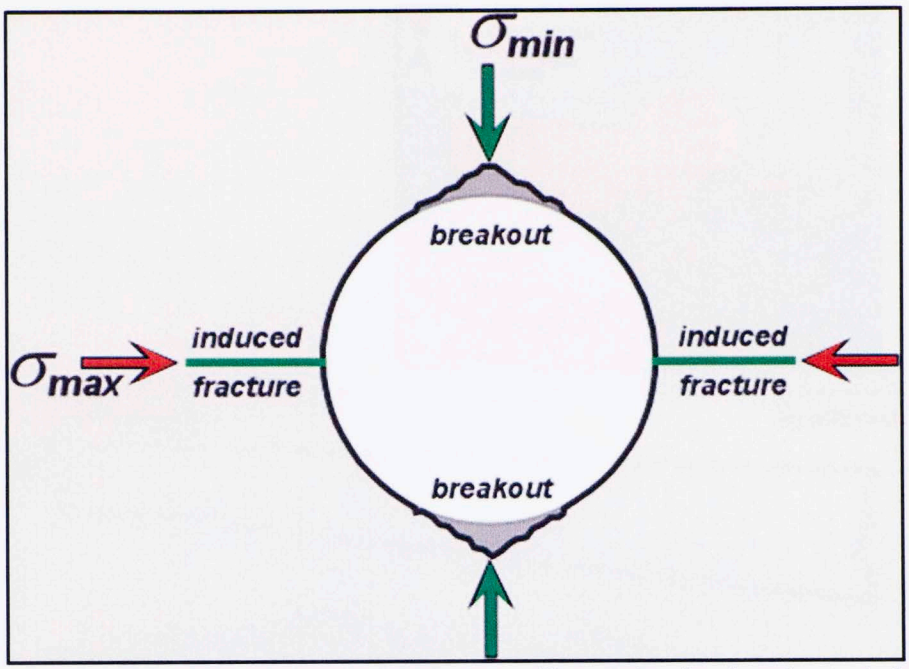

Figure 61. Cross-section perpendicular through the wellbore, showing breakouts, induced tensile fractures, and the maximum and minimum directions of the horizontal principal stresses in the present (modified from Lacazette, 2000).

The normal faulting in the Lawrence Uplift-Franks Graben area was generated by tensional collapse created during the orogeny. In this area, the vertical principal stress overcame in magnitude the other two horizontal principal stresses. This is the reason that a system of tensional fractures was generated, and additional uplift eliminated compressional stresses, to form grabens, horsts, and collapse along the dual system of fractures (Figure 62) (Diggs, 1961). Geologic history places regional and local structural events to have occurred after the deposition of the Woodford Shale formation.

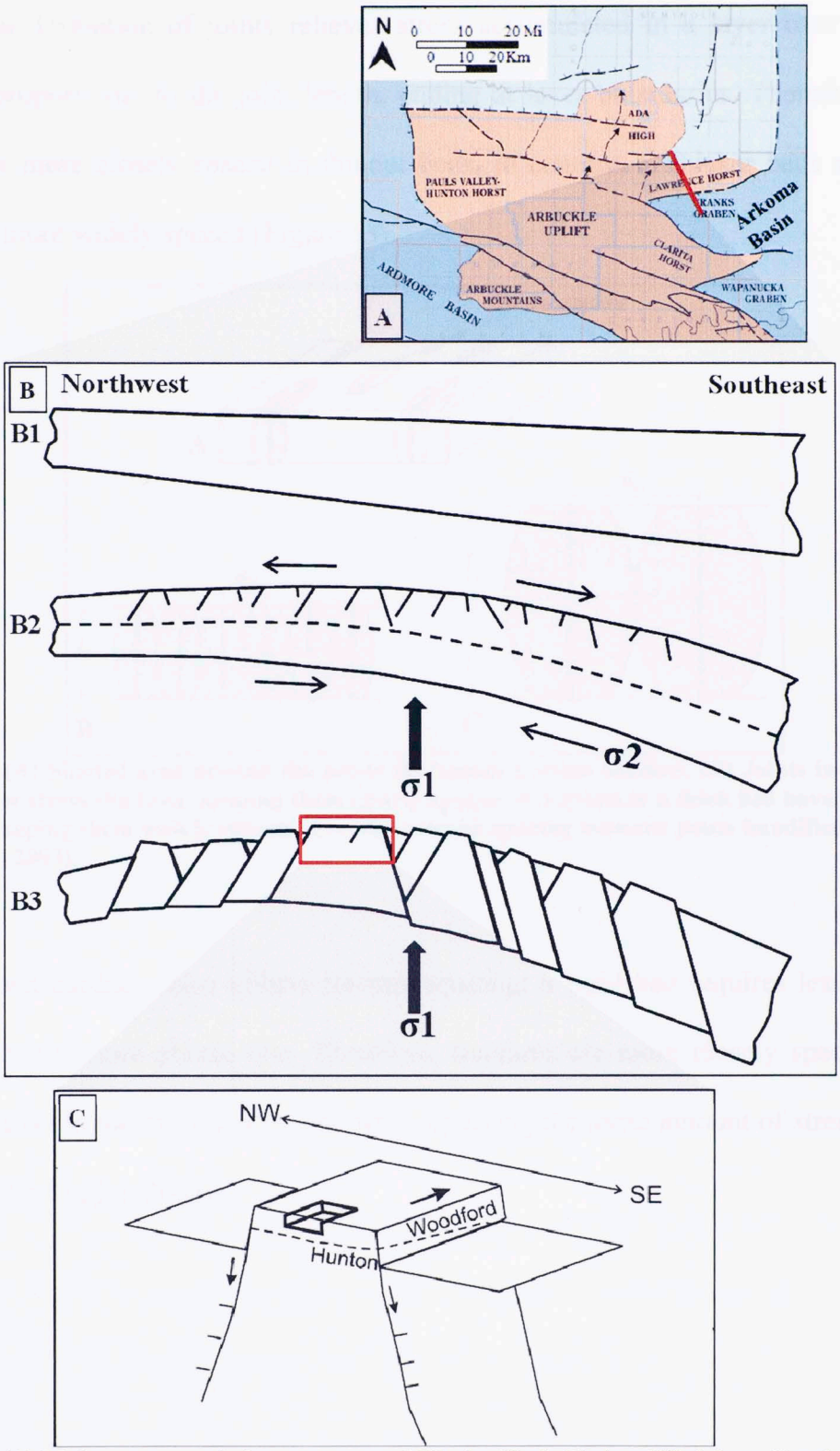

Figure 62. (A) Major structural elements around Wyche Shale Pit (modified from Northcutt, 1995), with location of cross-section. (B) Sketch showing the theory for the origin of the fracturing in the area of study. (B1) Represents the area before deformation, (B2) Beginning of the formation of tensional fractures by uplift, and (B3) Continuation of uplift producing tensional collapse, red rectangle represents Wyche Shale Pit area shown in Figure C (modified from Digg, 1961). (C) Sketch cross-section showing structural position of the outcrop (not to scale).

The formation of joints relieves stress accumulated in a layer over a lateral distance proportional to the joint length, ending at layer boundaries. Therefore, joints tend to be more closely spaced in thinner beds, in contrast to thicker beds where the joints are more widely spaced (Figure 63).

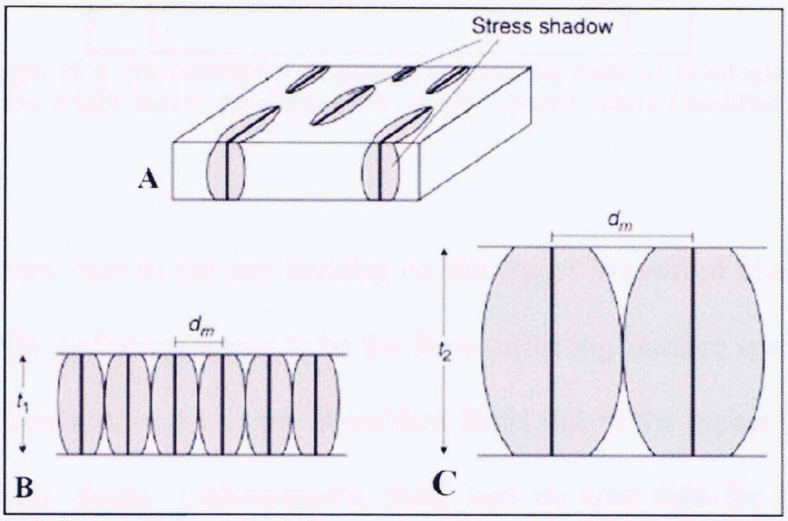

Figure 63. (A) Shaded area around the joints represents a stress shadow. (B) Joints in a thin bed have narrow stress shadows, keeping them closely spaced. (C) Joints in a thick bed have wide stress shadows, keeping them widely spaced. d_m is the average spacing between joints (modified from Van der Pluijm, 2003).

Rock hardness also affects fracture spacing; a rigid bed requires less stress to fracture than a more plastic one. Therefore, fractures are more closely spaced in the rigid bed than in the more plastic one when applying the same amount of stress (Figure 64) (Van der Pluijm, 2003).

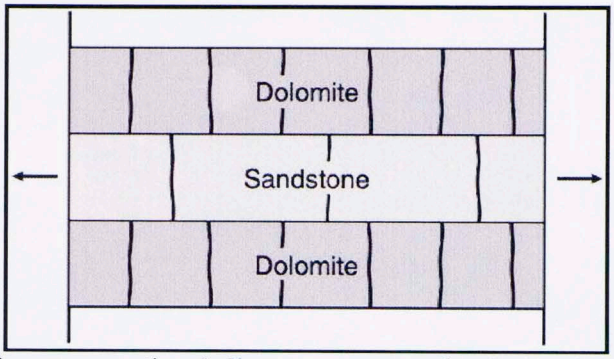

Figure 64. Example of a cross-sectional diagram representing beds of lithologies with different elasticity. Dolomite (rigid layer) develops more closely spaced joints (modified from Van der Pluijm, 2003).

It was very hard to see any bedding on the Upper Woodford Shale exposed on the outcrop walls. Lithology seems to be the factor affecting fracture spacing. The core contains more fractures in the Upper Woodford Shale due to the higher quartz content that makes it less elastic. Unfortunately, there was no core data for the Hunton to compare, but on seismic the interval below the Woodford-Hunton contact is more fractured that the interval above (Figure 3).

On the quarry walls, there visually seemed to be fracture swarms, but after the LIDAR data was characterized, this observation was dismissed with an average fracture spacing of 1.2m (4ft), which may be due to a lack of lateral lithology or bedding change.

Figure 65 is the fracture model for the Wyche Shale Pit, generated with fractures interpreted on LIDAR and seismic data. Figure 66 is the structural map of the Arbuckle Mountains with the fracture model from the area of study.

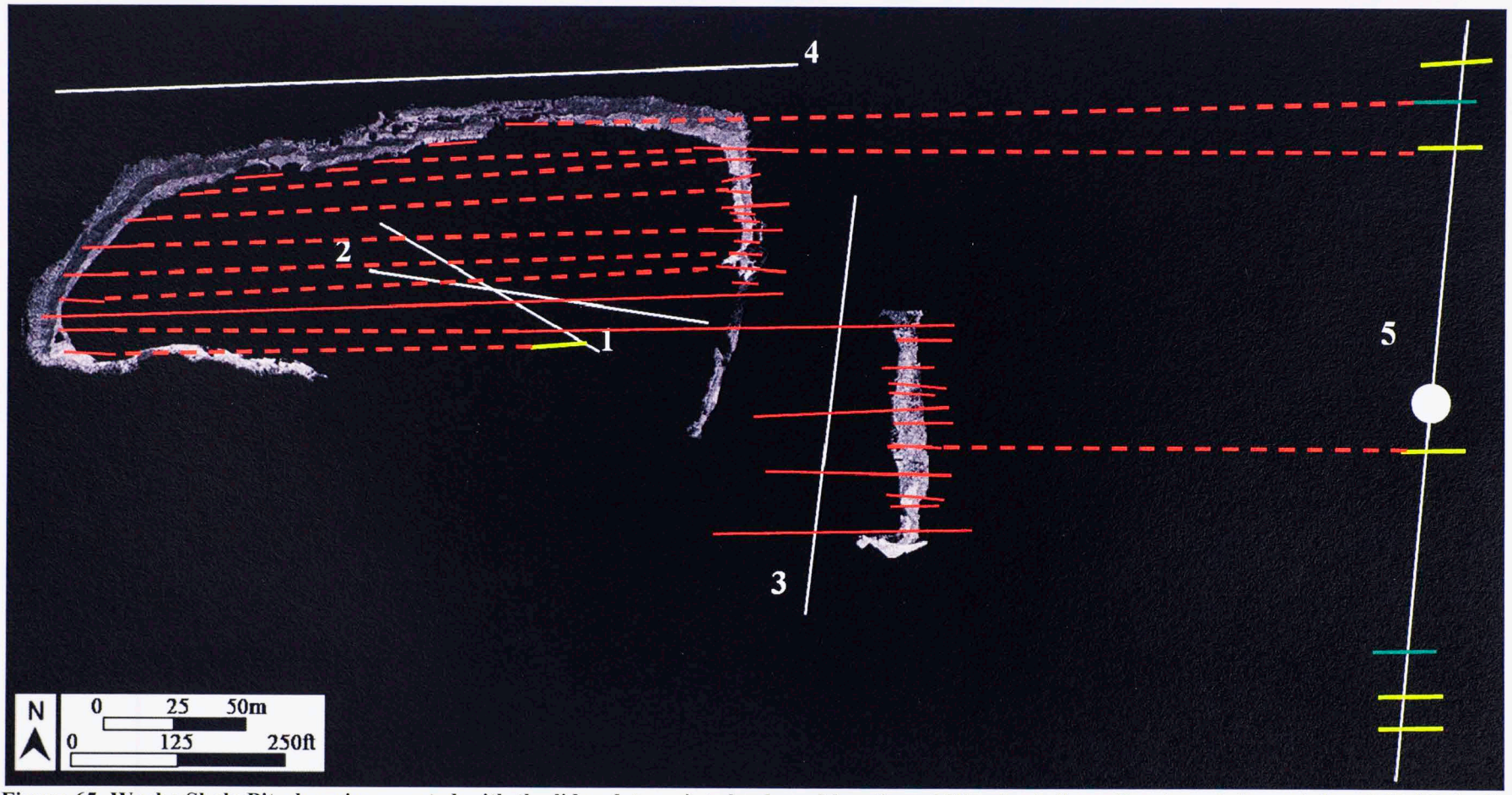

Figure 65. Wyche Shale Pit plan view created with the lidar data point clouds and location of 2D seismic lines. Fractures interpreted on LIDAR (red) and seismic data (yellow and green) are correlated. Group 1 fractures have an average strike of N85°E.

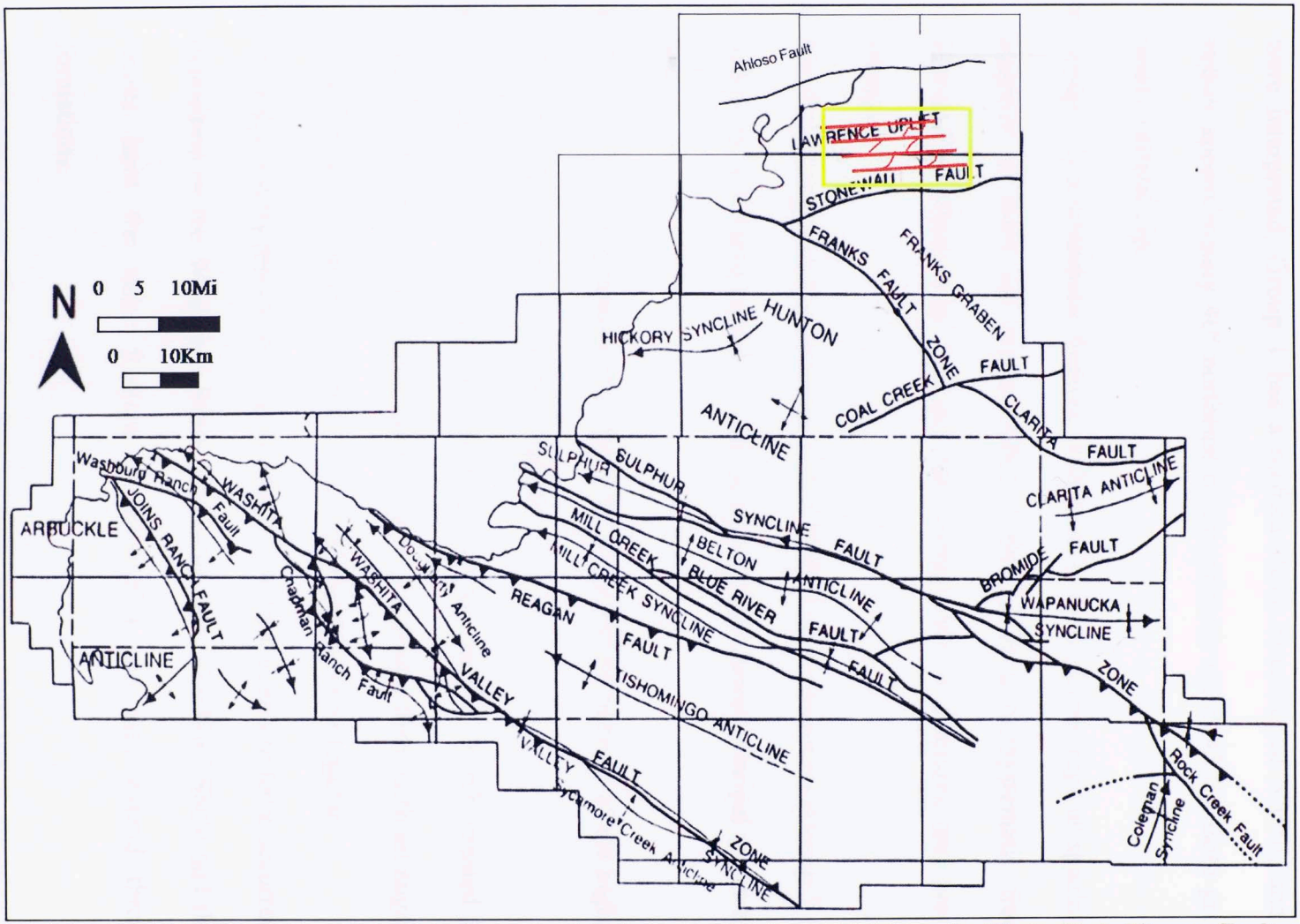

Figure 66. Map of the Arbuckle Mountains with principal structural features and fracture model from the Wyche Shale Pit area. Faults are shown by thick lines (thrust faults with sawteeth), folds (anticlines and synclines) are shown by thin lines. The location of study area is between the Ahloso Fault (normal fault with hanging wall to the north, striking east-west), and the Stonewall Fault (normal fault with hanging wall to the southeast, striking southwest-northeast) (modified from Suneson, 1997).

5. CONCLUSIONS

- Fractures in the Wyche Shale Pit are extensional fractures (joints). Two fractures sets were interpreted: Group 1 has a median strike direction of N85°E, and Group 2 strikes approximately 40° northeast of the primary set (N45°E). Both groups have nearly vertical dip.
- Group 1 is a systematic fracture with parallel orientations, regular spacing, and the majority of them are mineral-filled. Group 2 is a nonsystematic fracture set, terminating where they intersect the primary set of fractures and are therefore younger.
- Borehole image log has fractures with a N50°E strike direction (Group 2 fractures), which are generated parallel to the maximum horizontal principal stress in the area now.
- There are more fractures in the Upper Woodford Shale because of the higher content of quartz, therefore it has greater rigidity.
- The plane of a fracture is perpendicular to $\sigma 3$, parallel to $\sigma 2$, created by failure produced by $\sigma 1$ present at the time of its origin. Faults form with an angle between 25-40° with $\sigma 1$. The study area has a normal-faulting stress regime.
- Geologic history places regional and local structural events to have occurred after the deposition of the Woodford Shale. Therefore, the Woodford Shale and the Hunton Group have the same fracture characteristics and they extend through both formations.
- The present stress field in the area of study has an ENE-WSW direction, the same direction that generated fractures in Group 2.

- There is no lateral lithology or bedding change, therefore the average fracture spacing is 1.2m (4ft).
- The 2D seismic lines allowed the interpretation of the Upper-Middle Woodford and Woodford-Hunton contact surface, showing no significant topography and dipping slightly to the northwest. The faults interpreted on the seismic follow the same trend as the regional faults and coincide with the fracture trends. On seismic, the interval below the Woodford-Hunton contact contains more fractures that the interval above.
- One of the objectives of this research was to determine if the fracture distribution was affected by paleotopography on the underlying Hunton Group unconformity surface. This could not be met because there was no relevant relief on the unconformity that could have affected the fracture distribution in a greater way than local tectonics.

6. RECOMMENDATIONS

The Wyche Shale Pit has enough space in an area close to the Wyche #1 well to collect a 3D seismic survey. This would be a great area to apply seismic attributes that can identify fracture trends, as well as their continuity into the Hunton Group and deeper (Figure 67).

Fractures in Group 1 have a N85°E strike direction and the maximum horizontal principal stress in the area has an ENE-WSW direction. Therefore, a horizontal well should be drilled perpendicular to the maximum horizontal principal stress in the area (in other words, parallel to the minimum horizontal principal stress), which will cut through many fractures in Group 1, Group 2, and will also generate many drilling-induced fractures (Figures 67 and 68).

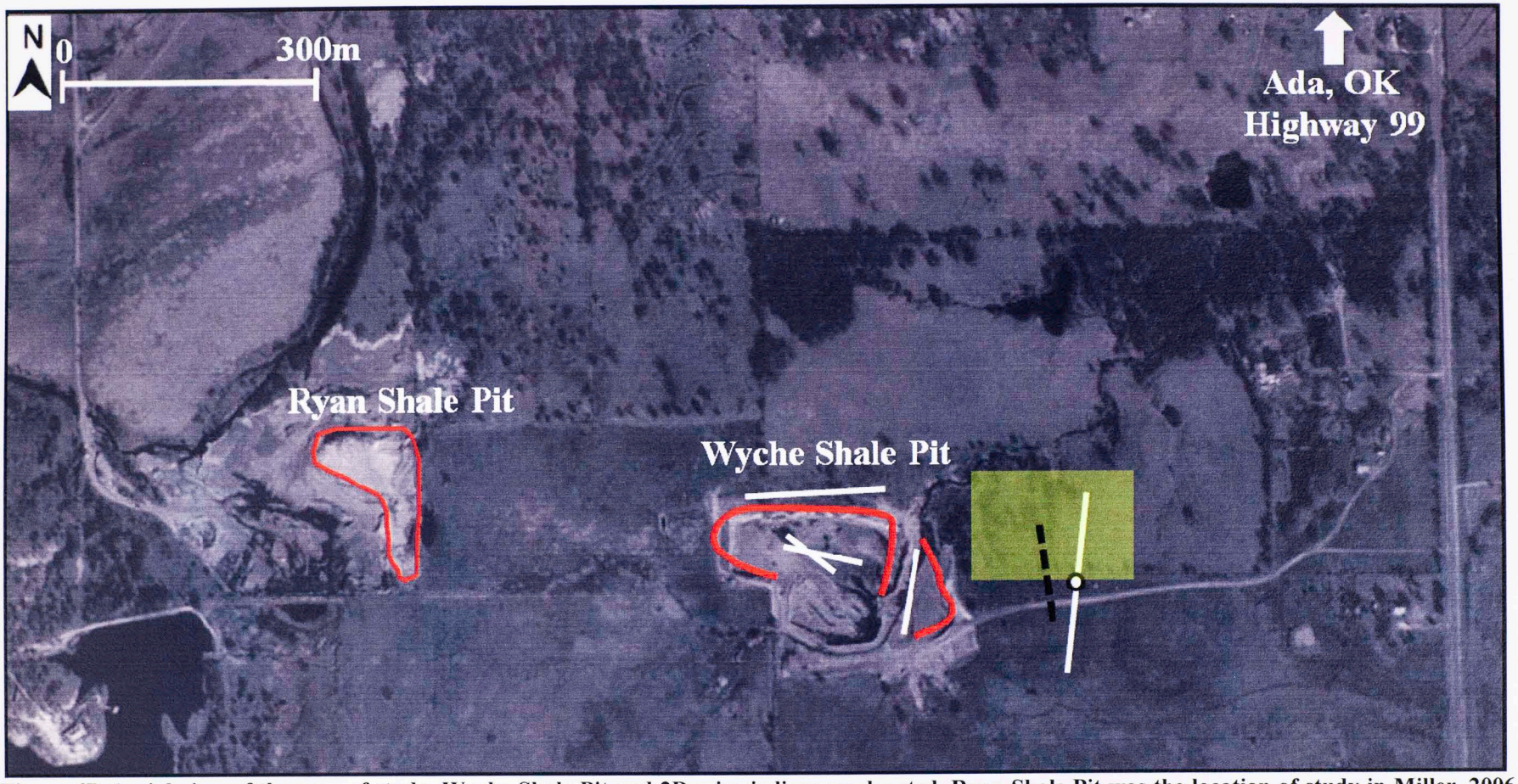

Figure 67. Aerial view of the area of study. Wyche Shale Pit and 2D seismic lines are located. Ryan Shale Pit was the location of study in Miller, 2006 and is west to the area of study in this thesis. The yellow square represents the possible location for a 3D seismic acquisition and the black dashed line represents the direction of drilling for a horizontal well (see Figure 68).

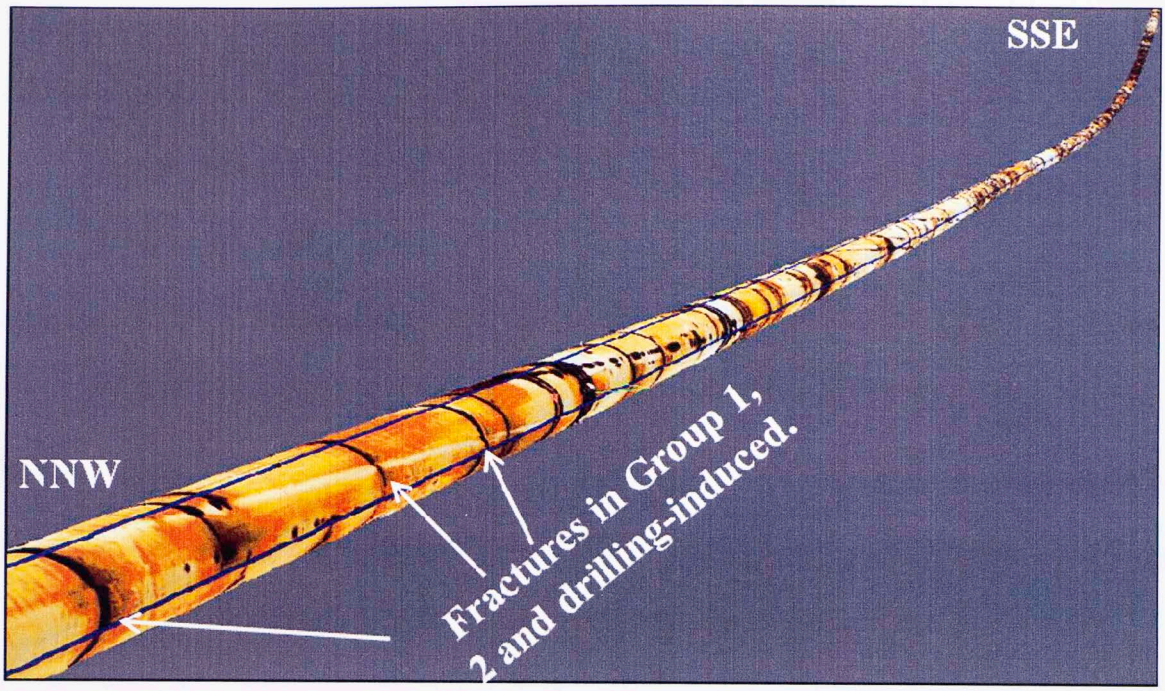

Figure 68. Borehole image log for a horizontal well drilled with a NNW-SSE direction perpendicular to the strike of fractures in group 1 and to σ2 (modified from Miller, 2006).

REFERENCES

Allmendinger, R. W., 2002, Stereonet for Macintosh / StereoWin for Windows, http://www.geo.cornell.edu/geology/faculty/RWA/programs.html, accessed January 20, 2009.

Amsden, T. W., 1980, Hunton Group (Late Ordovician, Silurian, and Early Devonian) in the Arkoma Basin of Oklahoma: Oklahoma Geological Survey Bulletin, 129.

Bellian, J. A., C. Kerans, and D. C. Jennette, 2005, Digital outcrop models: Applications of terrestrial scanning lidar technology in stratigraphic modeling: Journal of Sedimentary Research, 75, no. 2, 166-176.

Bellian, J. A., Jennette, D. C., Kerans, C., Gibeaut, J., Andrews, J., Yssldyk, B., and Larue, D., 2002, 3-Dimensional digital outcrop data collection and analysis using eye-safe laser (LIDAR) technology, AAPG Search and Discovery Article, 40056.

Blakey, R., 2005, Paleogeography and Geologic Evolution of North America - Images that track the ancient landscapes of North America, http://jan.ucc.nau.edu/~rcb7/nam.html, accessed March 20, 2009.

Bonnaffe, F., D. Jennette, and J. Andrews, 2007, A method for acquiring and processing ground-based lidar data in difficult-to-access outcrops for use in three-dimensional, virtual-reality models: Geosphere, 3, no. 6, 501-510.

Branch, A. A., 2007, Comprehensive characterization of a core from an overmature Woodford shale in Leflore County, Oklahoma, and comparison with data from other studies of the Woodford shale in the Arkoma Basin: M.S. thesis, University of Oklahoma.

Browne, G. H., R. M. Slatt, and P. R. King, 2000, Outcrop and behind-outcrop characterization of a Late Miocene slope fan (channel-levee complex), Mt. Messenger Formation, New Zealand, *in* Bouma, A. H., C. Stelting, and C. G. Stone, eds., Fine-grained turbidite systems: AAPG Memoir 72 / SEPM Special Publication 68, 143-152.

Buckner, T. N., 2009, High resolution facies changes, lateral continuity, and fracturing of the Woodford Shale from behind outcrop drilling, logging, and coring: M.S. thesis, University of Oklahoma.

Cardott, B. J., 2001, Thermal maturation of the Woodford Shale in Eastern Oklahoma, *in* K. S. Johnson and D. F. Merriams, eds., Petroleum systems of sedimentary basins in the southern Midcontinent, 2000 symposium: Oklahoma Geological Survey, Circular 106, p. 193.

Cardott, B. J., 2005, Overview of unconventional energy resources of Oklahoma, *in* B. J. Cardott, ed., Unconventional energy resources in the southern Midcontinent, 2004 symposium: Oklahoma Geological Survey Circular 110.

Cardott, B. J., 2007, Overview of Woodford gas-shale play in Oklahoma: Oklahoma Geological Survey, Woodford Gas Shale Conference, http://www.ogs.ou.edu/pdf/WoodfordOverview.pdf, accessed on March 15, 2009.

Ciftci, B. N., A. A. Aviantara, N. F. Hurley, and D. R. Kerr, 2004, Outcrop-based three-dimensional modeling of the Tensleep Sandstone at Alkali Creek, Bighorn Basin, Wyoming, *in* G. M. Grammer, P. M. Harris, and G. P. Eberli, eds., Integration of outcrop and modern analogs in reservoir modeling: AAPG

Memoir 80, 235-259.

Cladouhos, T. T., and R. Marrett, Are fault growth and linkage models consistent with power-law distributions of fault lengths?: Journal of Structural Geology, 18, no. 2/3, 281-293

Comer, J. B., 2005, Facies distribution and hydrocarbon production potential of Woodford Shale in the Southern Midcontinent: Oklahoma Geological Survey Circular 110, 51 – 62.

Davis, R. J., C. R. Blume, and R. M. Slatt, 2006, Reservoir characterization applications of electrical borehole images, *in* R. M. Slatt, N. C. Rosen, M. Bowman, J. Castagna, T. Good, R. Loucks, R. Latimer, M. Scheihing, and R. Smith, eds., Reservoir Characterization: Integrating Technology and business practices: 26th Annual GCSSEPM Foundation Bob F. Perkins Research Conf., Dec. 3-6, Houston, CD Book.

Diggs, W. E., 1961, Structural framework of the Arkoma basin: Tulsa Geological Society Guidebook, Field Conference.

Goyeneche, J. C., 2005, Outcrop characterization, 3D geological modeling, "reservoir" simulation and upscaling of Jackfork Group turbidites in Hollywood quarry, Arkansas: M.S. thesis, University of Oklahoma.

Goyeneche, J. C., R. M. Slatt, A. C. Rothfolk, and R. J. Davis, 2006, Systematic geological and geophysical characterization of a deepwater outcrop for 'reservoir' simulation: Hollywood Quarry, Arkansas, *in* R. M. Slatt, N. C. Rosen, M. Bowman, J. Castagna, T. Good, R. Loucks, R. Latimer, M. Scheihing, and R. Smith, eds., Reservoir Characterization: Integrating

Technology and business practices: 26th Annual GCSSEPM Foundation Bob F. Perkins Research Conf., Dec. 3-6, Houston, CD Book.

Ham, W. E., 1973, Regional geology of the Arbuckle Mountains, Oklahoma: Oklahoma Geological Survey Special Publication 73-3.

Hansen, S. M., and T. Fett, 2000, Identification and Evaluation of Turbidite and Other Deepwater Sands Using Open Hole Logs and Borehole Images, *in* A. H. Bouma and C. G. Stone, eds., Fine-Grained Turbidite Systems: AAPG Memoir 72 / SEPM Special Publication 68, 317-337.

Heidbach, O., m. Tingay, A. Barth, J. Reinecker, d. Kurfeß, and B. Müller, 2005, The 2008 release of the World Stress Map, http://www.world-stress-map.org, accessed on May 4, 2009.

InnovMetric Software, 2009, PolyWorks®, http://www.innovmetric.com/Surveying/english/home.html, accessed on March 15, 2009.

Lacazette, A., 2000, Technical Presentations on Fractures, http://www.naturalfractures.com/technical.htm, accessed on April 9, 2009.

Lee, K., M. Tomasso, W. A. Ambrose, 2007, Integration of GPR with stratigraphic and lidar data to investigate behind-the-outcrop 3D geometry of a tidal channel reservoir analog, upper Ferron Sandstone, Utah: The Leading Edge, 26, 994-98.

Marrett, R., O. J. Ortega, and C. M. Kelsey, 1999, Extent of power-law scaling for natural fractures in rock: Geology, 27, no.9, 799-802.

Miller, C., 2006, Horizontal well planning within the Woodford Shale and other gas shales within the Mid-Continent, USA,

http://www.ogs.ou.edu/pdf/GSMillerS.pdf, accessed March 15, 2009.

Miller, R. C., 2006, Characterization of the Woodford Shale in outcrop and subsurface in Pontotoc and Coal Counties, Oklahoma: M.S. thesis, University of Oklahoma.

Mitcham, T. W., 1963, Scientific Communication – Fractures, joints, faults and fissures: Economic Geology, 58, 1157-1158.

Negrey, A. L., 2005, Geophysical evaluation of a deepwater channel prospect using spectral decomposition: Permian Wolfcamp limestone, Midland Basin: M.S. thesis, University of Oklahoma.

Niglio, L. C., Fracture analysis of Precambrian and Paleozoic rocks in selected areas of the Grand Canyon National Park, USA: M.S. thesis, university of Oklahoma.

Northcutt, R. A., and J. A. Campbell, 1996, Geologic Provinces of Oklahoma: The Shale Shaker, 46, no. 5, 99-103.

Optech Inc, 2003, Standard instrument Specifications for the Optech ILRIS 3D Terrestrial Line Scanner, http://epswww.unm.edu/facstaff/tfw/IMAGES/pdfs/ilrisspecsheet.pdf, accessed April 10, 2009.

Ortega, O. J., R. A. Marrett, and S. E. Laubach, 2006, A scale-independent approach of fracture intensity and average spacing measurement: AAPG Bulletin, 90, no. 2, 193-208.

Partyka, G., J. Gridley, and J. Lopez, 1999, Interpretational applications of spectral decomposition in reservoir characterization: The Leading Edge, 18, 353-360.

Perry, W. J., 1995, USGS 1995 National Oil and Gas Assessment - Arkoma Basin Province. United States Geological Survey 62.

Rich, A. J., Fracture analysis and paleostress history of the Gulf of Suez margin, Egypt: M.S. thesis, University of Oklahoma.

Rothfolk, A. C., 2006, Characterization of a fractured, turbidite channel sandstone: The Jackfork group, Hollywood Quarry, Arkansas: M.S. thesis, University of Oklahoma.

Rottmann, K., E. A. Beaumont, R. A. Northcutt, Z. Al-Shaieb, J. Puckett, and P. Blubaugh, 2000, Hunton play in Oklahoma (including Northeast Texas Panhandle): Oklahoma Geological Survey Special Publication 2000-2, 131 p., 6 pls.

Slatt, R. M., H. A. Al-Siyabi, C. W. VanKirk, and R. W. Williams, 2000, From geologic characterization to 'reservoir simulation' of a turbidite outcrop, Arkansas, U.S.A., *in* A. H. Bouma and C. G. Stone, eds., Fine-Grained Turbidite Systems: AAPG Memoir 72 / SEPM Special Publication 68, 187-194.

Split Engineering LLC, 2009, Split-FX® Software Automated Rock Mass Fracture Characterization, http://www.spliteng.com/split-fx/default.asp, accessed on March 15, 2009.

Suneson, N. H., 1997, The geology of the eastern Arbuckle Mountains in Pontotoc and Johnston counties, Oklahoma – An introduction and field-trip guide: Oklahoma Geological Survey Open File Report 4-97.

Tomasso, M., F. L. Bonnaffe, D. R. Pyles, R. Bouroullec, and D. C. Jennette, 2006, Outcrop versus seismic architecture of deep-water deposits: use of lidar along a slope-to-basin transect of the Brushy Canyon formation, West Texas, *in* R. M. Slatt, N. C. Rosen, M. Bowman, J. Castagna, T. Good, R. Loucks, R. Latimer,

M. Scheihing, and R. Smith, eds., Reservoir Characterization: Integrating Technology and business practices: 26th Annual GCSSEPM Foundation Bob F. Perkins Research Conf., Dec. 3-6, Houston, CD Book.

Van der Pluijm, B .A. and S. Marshak, 2003, Earth Structure - An Introduction to Structural Geology and Tectonics, 2nd edition, W.W. Norton, 674 p.

APPENDICES

Appendix 1. GPS locations for the Wyche Shale Pit

Station Name	WGS84_LAT	WGS84_LON	WGS84_ALT (m)	WGS84_LAT	WGS84_LON	UTM_X	UTM_Y	Notes
Well	N34°40.357	W96°38.374	260	34.67261667	-96.63956667	716269.5697	3839273.641	
Well road	N34°40.351	W96°38.374	256	34.67251667	-96.63956667	716269.8301	3839262.549	Dist well-road
P01	N34°40.349	W96°38.398	258	34.67248333	-96.63996667	716233.26	3839257.991	
P02	N34°40.348	W96°38.416	258	34.67246667	-96.64026667	716205.8109	3839255.499	
P03	N34°40.346	W96°38.435	257	34.67243333	-96.64058333	716176.8784	3839251.12	
P04	N34°40.341	W96°38.455	256	34.67235	-96.64091667	716146.5473	3839241.161	
P05	N34°40.334	W96°38.472	254	34.67223333	-96.6412	716120.8857	3839227.611	
P06	N34°40.327	W96°38.487	252	34.67211667	-96.64145	716098.2785	3839214.134	
P07	N34°40.324	W96°38.496	251	34.67206667	-96.6416	716084.6622	3839208.266	Corner
P08	N34°40.328	W96°38.497	249	34.67213333	-96.64161667	716082.9613	3839215.624	
P09	N34°40.336	W96°38.481	246	34.67226667	-96.64135	716107.0528	3839230.987	
P10	N34°40.339	W96°38.472	246	34.67231667	-96.6412	716120.6691	3839236.856	
P11	N34°40.354	W96°38.486	246	34.67256667	-96.64143333	716098.6366	3839264.085	
P12	N34°40.369	W96°38.494	247	34.67281667	-96.64156667	716085.7674	3839291.53	
P13	N34°40.378	W96°38.499	247	34.67296667	-96.64165	716078.131	3839291.351	
P14	N34°40.325	W96°38.519	249	34.67208333	-96.64198333	716049.4899	3839209.291	
P15	N34°40.339	W96°38.525	246	34.67231667	-96.64208333	716039.7194	3839234.959	
P16	N34°40.356	W96°38.533	247	34.6726	-96.64221667	716026.7638	3839266.101	
P17	N34°40.368	W96°38.539	245	34.6728	-96.64231667	716017.08	3839288.071	
P18	N34°40.383	W96°38.532	240	34.67305	-96.6422	716027.1222	3839316.052	
P19	N34°40.395	W96°38.527	241	34.67325	-96.64211667	716034.2389	3839338.416	
P20	N34°40.404	W96°38.543	241	34.6734	-96.64238333	716009.4124	3839354.482	
P21	N34°40.411	W96°38.561	241	34.67351667	-96.64268333	715981.6172	3839366.779	
P22	N34°40.418	W96°38.581	240	34.67363333	-96.64301667	715950.7668	3839379.004	
P23	N34°40.421	W96°38.601	240	34.67368333	-96.64335	715920.0906	3839383.835	
P24	N34°40.415	W96°38.619	239	34.67358333	-96.64365	715892.8583	3839372.099	
P25	N34°40.413	W96°38.642	235	34.67355	-96.64403333	715857.8164	3839367.58	
P26	N34°40.409	W96°38.662	240	34.67348333	-96.64436667	715827.4422	3839359.47	

Station Name	WGS84_LAT	WGS84_LON	WGS84_ALT (m)	WGS84_LAT	WGS84_LON	UTM_X	UTM_Y	Notes
P27	N34°40.398	W96°38.676	239	34.6733	-96.6446	715806.5356	3839338.634	
P28	N34°40.391	W96°38.687	238	34.67318333	-96.64478333	715790.038	3839325.299	
P29	N34°40.384	W96°38.691	241	34.67306667	-96.64485	715784.2311	3839312.216	
P30	N34°40.378	W96°38.673	239	34.67296667	-96.64455	715811.9829	3839301.767	
P31	N34°40.382	W96°38.653	243	34.67303333	-96.64421667	715842.3564	3839309.876	
P32	N34°40.380	W96°38.632	245	34.673	-96.64386667	715874.5172	3839306.93	
P33	N34°40.388	W96°38.635	246	34.67313333	-96.64391667	715869.589	3839321.612	
P34	N34°40.392	W96°38.613	245	34.6732	-96.64355	715903.0177	3839329.794	
P35	N34°40.387	W96°38.593	250	34.67311667	-96.64321667	715933.7807	3839321.266	
P36	N34°40.379	W96°38.576	246	34.67298333	-96.64293333	715960.0925	3839307.083	

Appendix 7. Scan line #1 and 2 measurements

Orientation metric tape: N5°E / S5°W

Index	Position (ft)	Orientation (N)	Orientation with metric tape (-5°)	Dilatation Width (ft)	Fill
1	0.542	48	43	0.14	Calcite - Effervesced to HCL 10%
2	0.82	51	46		
3	0.93	124	119		
4	1.112	108	103		
5	1.18	52	47	0.01	No calcite - No effervesced
6	1.39	49	44		
7	1.5	98	93		
8	1.58	158	153		
9	1.59	60	55		
10	1.79	86	81		
11	1.99	95	90	0.001	No calcite - No effervesced
12	2.22	44	39	0.02	Black filling with a little bit if calcite
13	2.36	118	113		
14	2.43	120	115		
15	2.6	94	89		
16	2.95	125	120		
17	3.19	85	80		
18	3.37	118	113		
19	3.54	110	105		
20	3.67	111	106		
21	3.68	111	106		
22	3.74	75	70		
23	3.8	98	93		
24	3.98	100	95		
25	4.05	102	97		
26	4.12	136	131		

Index	Position (ft)	Orientation (N)	Orientation with metric tape (-5°)	Dilatation Width (ft)	Fill
27	4.37	137	132		
28	4.44	50	45		
29	4.48	49	44		
30	4.52	49	44	0.01	
31	4.64	43	38		
32	4.78	48	43	0.02	White filling - No calcite - No effervesced
33	4.84	124	119		
34	4.86	48	43		
35	5	80	75		
36	5.05	73	68		
37	5.13	154	149		
38	5.23	67	62		
39	5.395	179	174		
40	5.48	116	111	0.01	
41	5.51	152	147		
42	5.6	48	43	0.01	
43	5.75	98	93		
44	5.81	147	142		
45	5.9	91	86		
46	5.9	91	86		
47	6.05	46	41	0.01	
48	6.2	131	126		
49	6.365	107	102		
50	6.47	72	67		
51	6.53	87	82		
52	6.6	147	142		
53	6.77	42	37		
54	6.83	94	89	0.02	
55	6.88	43	38		

Index	Position (ft)	Orientation (N)	Orientation with metric tape (-5°)	Dilatation Width (ft)	Fill
56	7.1	90	85		
57	7.21	50	45		
58	7.31	48	43	0.01	
59	7.47	80	75	0.01	White filling - Effervesced - Calcite
60	7.67	90	85		
61	7.87	136	131		
62	7.93	111	106		
63	7.99	112	107	0.01	
64	8.02	94	89	0.02	
65	8.15	46	41		
66	8.27	93	88		
67	8.39	56	51		
68	8.5	106	101		
69	8.98	39	34	0.01	
70	9.01	40	35		
71	9.35	45	40		
72	9.48	67	62		
73	9.65	118	113		
74	9.71	81	76	0.02	White filling - No calcite - No effervesced
75	9.77	31	26		
76	9.89	110	105		
77	9.98	48	43	0.01	
78	10.14	96	91		
79	10.26	99	94		
80	10.28	46	41		
81	10.34	50	45	0.01	
82	10.6	50	45	0.01	White, with a lot of effervesces
83	10.78	88	83		
84	11.09	49	44	less than 0.01	White, with a lot of effervesces

Index	Position (ft)	Orientation (N)	Orientation with metric tape (-5°)	Dilatation Width (ft)	Fill
85	11.16	41	36	less than 0.01	White, effervesces
86	11.37	86	81		
87	11.5	94	89		
88	11.55	111	106		
89	11.61	49	44	0.01	White, little effervesce, something else
90	11.66	96	91		
91	11.69	131	126		
92	11.74	48	43		
93	11.91	89	84		
94	11.94	78	73		
95	12.03	53	48	0.02	Some effervesce
96	12.27	76	71		
97	12.4	83	78		
98	12.52	56	51		
99	12.55	55	50		
100	12.67	47	42		
101	12.7	52	47		
102	12.71	131	126		
103	12.8	44	39		
104	12.99	84	79		
105	13.21	99	94		
106	13.23	108	103		
107	13.35	47	42		
108	13.42	44	39		
109	13.45	102	97		
110	13.5	102	97		
111	13.71	94	89		
112	13.88	95	90	less than 0.01	
113	13.94	109	104	less than 0.01	

Index	Position (ft)	Orientation (N)	Orientation with metric tape (-5°)	Dilatation Width (ft)	Fill
114	14.02	128	123		
115	14.16	45	40	0.02	Gray filling
116	14.39	148	143		
117	144	95	90		
118	14.64	118	113		
119	14.77	96	91		
120	15.06	40	35		
121	15.06	90	85	less than 0.01	
122	15.35	86	81		
123	15.52	145	140		
124	15.69	45	40	less than 0.01	
125	15.85	95	90		
126	15.93	90	85		
127	16.15	118	113		
128	16.38	40	35		
129	16.51	53	48		
130	16.7	40	35	0.01	
131	16.71	157	152		
132	16.84	55	50		
133	16.91	55	50		
134	17.02	32	27		
135	17.04	79	74		
136	17.09	72	67		
137	17.13	43	38		
138	17.33	37	32		
139	17.38	42	37		
140	17.41	46	41		
141	17.45	46	41		
142	17.59	43	38		

Index	Position (ft)	Orientation (N)	Orientation with metric tape (-5°)	Dilatation Width (ft)	Fill
143	17.6	130	125		
144	17.64	98	93		
145	17.72	55	50	less than 0.01	White, no effervesce
146	17.87	146	141		
147	17.99	36	31		
148	18.08	53	48		
149	18.21	40	35		
150	18.47	118	113		
151	18.5	43	38		
152	18.71	145	140		
153	18.81	46	41		
154	18.91	144	139		
155	19.1	50	45	less than 0.01	
156	19.13	165	160		
157	19.3	147	142		
158	19.48	50	45		
159	19.48	165	160		
160	19.63	50	45		
161	19.9	45	40		
162	19.95	45	40		
163	20.05	45	40		

Orientation metric tape: N42°W / S42°E (N317°)

Index	Position (ft)	Orientation (N)	Orientation with metric tape (+42°)	Dilatation Width (ft)	Fill
1	0.41	53	95	0.01	Little effervesce
2	0.64	3	45		
3	0.72	44	86	0.01	Gray filling, effervesce
4	0.76	45	87	0.01	White filling, effervesce
5	1.04	35	77	0.003	Effervesce
6	1.12	26	68	0.01	Gray filling
7	1.16	25	67		
8	1.29	37	79		
9	1.62	80	122		
10	1.67	72	114		
11	1.75	102	144		
12	1.82	66	108		
13	2.07	63	105		
14	2.1	53	95		
15	2.12	47	89		
16	2.17	45	87		
17	2.28	72	114		
18	2.34	45	87		
19	2.5	45	87		
20	2.53	42	84		
21	2.62	45	87	0.01	
22	2.68	64	106	0.01	
23	2.74	45	87		
24	2.88	1	43		
25	3	45	87		
26	3.03	170	212		
27	3.2	45	87	0.005	Effervesce
28	3.28	64	106		
29	3.3	65	107		

Index	Position (ft)	Orientation (N)	Orientation with metric tape (+42°)	Dilatation Width (ft)	Fill
30	3.34	66	108		
31	3.52	48	90	0.005	Effervesce
32	3.7	39	81		
33	3.9	75	117		
34	3.98	73	115		
35	4.1	50	92	0.005	Effervesce
36	4.15	68	110		Effervesce
37	4.3	9	51		
38	4.39	73	115		
39	4.55	48	90		
40	4.69	25	67		
41	4.71	44	86	0.005	Effervesce
42	4.72	46	88		Effervesce
43	4.73	86	128		
44	4.78	84	126		
45	4.86	98	140		
46	4.92	50	92		
47	4.94	49	91		White filling, Qz
48	4.99	48	90		
49	5.13	68	110		
50	5.22	73	115		
51	5.3	52	94		
52	5.38	47	89		
53	5.42	80	122		
54	5.96	78	120		
55	5.99	85	127		
56	6.02	78	120		
57	6.05	100	142		
58	6.1	50	92	0.005	Effervesce
59	6.1	83	125		Effervesce

Index	Position (ft)	Orientation (N)	Orientation with metric tape (+42°)	Dilatation Width (ft)	Fill
30	3.34	66	108		
31	3.52	48	90	0.005	Effervesce
32	3.7	39	81		
33	3.9	75	117		
34	3.98	73	115		
35	4.1	50	92	0.005	Effervesce
36	4.15	68	110		Effervesce
37	4.3	9	51		
38	4.39	73	115		
39	4.55	48	90		
40	4.69	25	67		
41	4.71	44	86	0.005	Effervesce
42	4.72	46	88		Effervesce
43	4.73	86	128		
44	4.78	84	126		
45	4.86	98	140		
46	4.92	50	92		
47	4.94	49	91		White filling, Qz
48	4.99	48	90		
49	5.13	68	110		
50	5.22	73	115		
51	5.3	52	94		
52	5.38	47	89		
53	5.42	80	122		
54	5.96	78	120		
55	5.99	85	127		
56	6.02	78	120		
57	6.05	100	142		
58	6.1	50	92	0.005	Effervesce
59	6.1	83	125		Effervesce

Index	Position (ft)	Orientation (N)	Orientation with metric tape (+42°)	Dilatation Width (ft)	Fill
60	6.26	115	157		
61	6.35	64	106		
62	6.42	86	128		
63	6.47	80	122		
64	6.49	50	92		
65	6.65	84	126		
66	6.7	60	102		
67	6.71	92	134		
68	6.75	47	89		
69	6.77	21	63		
70	6.8	35	77		
71	6.81	54	96		
72	6.82	76	118		
73	6.92	60	102	0.005	Effervesce
74	6.97	35	77		
75	7.04	35	77		Effervesce a lot
76	7.05	41	83		
77	7.12	68	110		
78	7.14	47	89		
79	7.19	5	47		
80	7.23	80	122		
81	7.25	85	127		
82	7.35	73	115		
83	7.44	20	62		
84	7.46	51	93		
85	7.57	69	111		
86	7.59	67	109		
87	7.97	98	140		
88	8.03	22	64		
89	8.18	104	146		

Index	Position (ft)	Orientation (N)	Orientation with metric tape (+42°)	Dilatation Width (ft)	Fill
90	8.22	36	78		
91	8.26	22	64		
92	8.38	160	202		
93	8.47	60	102		
94	8.83	43	85		Effervesce
95	8.93	48	90	0.01	White fill, effervesce
96	8.95	110	152		
97	9.1	30	72		
98	9.13	32	74	0.01	
99	9.3	90	132		
100	9.44	25	67		
101	9.54	32	74	0.01	
102	9.62	26	68	0.01	White fill, effervesce
103	9.65	58	100	0.01	White fill, effervesce
104	9.73	105	147		
105	9.78	48	90		
106	9.9	85	127		
107	9.97	47	89		Effervesce
108	10.1	24	66	2.001	White rimmed
109	10.16	26	68	0.01	Dark filling
110	10.33	12	54	0.001	
111	10.35	84	126	0.01	Material eroded
112	10.48	41	83	0.001	
113	10.66	29	71	0.001	
114	10.68	40	82	0.001	
115	10.83	41	83	0.001	
116	10.94	99	141	0.002	
117	10.97	90	132	0.001	
118	11.04	12	54	0.002	
119	11.05	92	134	0.001	

Index	Position (ft)	Orientation (N)	Orientation with metric tape (+42°)	Dilatation Width (ft)	Fill
120	11.13	72	114	0.001	
121	11.17	38	80	0.001	
122	11.18	89	131	0.001	
123	11.29	51	93	0.009	
124	11.385	59	101	Healed, 0.001	Dark filling
125	11.42	39	81	0.001	
126	11.485	68	110	0.001	
127	11.49	40	82	0.001	
128	11.51	40	82	0.001	
129	11.72	28	70	Healed, 0.002	Dark and white filling
130	11.82	42	84	0.002	
131	11.85	47	89	0.001	
132	12.08	44	86	0.004	
133	12.13	8	50	Healed, 0.001	Dark
134	12.3	36	78	0.001	
135	12.36	83	125	0.005	
136	12.55	48	90	Hairline	
137	12.62	39	81	0.001	
138	12.8	92	134	0.001	
139	12.86	28	70	Healed, 0.002	Dark
140	12.89	32	74	Healed, 0.002	Dark
141	12.92	35	77	Healed, 0.002	Dark
142	12.99	43	85	Healed, 0.001	Dark
143	13.05	64	106	0.001	
144	13.12	8	50	0.001	
145	13.16	65	107	0.001	
146	13.51	48	90	0.002	
147	13.59	34	76	0.001	
148	13.72	44	86	Healed, 0.001	White fill
149	14.02	24	66	0.001	

Index	Position (ft)	Orientation (N)	Orientation with metric tape (+42°)	Dilatation Width (ft)	Fill
150	14.24	44	86	0.01	
151	14.31	15	57	0.001	
152	14.545	49	91	0.002	
153	14.68	26	68	Healed, 0.01	White and dark fill
154	14.72	28	70	Healed, 0.008	White and dark fill
155	14.74	34	76	Hairline, 0.001	
156	14.84	81	123	Hairline, 0.001	
157	14.92	13	55	0.001	
158	15.32	16	58	Hairline, 0.001	
159	15.41	47	89	0.003	
160	15.54	83	125	Healed, 0.004	White fill
161	15.68	14	56	Healed, 0.005	White fill
162	15.85	102	144	Healed, 0.001	Dark filling
163	15.91	51	93	0.001	
164	16.035	44	86	Healed, 0.005	Dark filling
165	16.15	38	80	Healed, hairline, 0.001	White fill
166	16.17	49	91	Healed, 0.005	White and dark fill
167	16.27	67	109	0.001	
168	16.45	7	49	0.001	
169	16.51	91	133	Healed, 0.001	Dark
170	16.91	8	50	Hairline, 0.001	
171	16.95	83	125	0.03	Dark fill
172	17.02	46	88	0.005	
173	17.19	2	44	0.001	
174	17.26	39	81	0.02	Dark fill
175	17.4	84	126	0.001	
176	17.69	48	90	0.002	Dark fill
177	17.72	46	88	0.002	
178	17.8	81	123	0.02	Dark and white filling
179	17.91	69	111	0.004	

Index	Position (ft)	Orientation (N)	Orientation with metric tape (+42°)	Dilatation Width (ft)	Fill
180	18.15	19	61	0.005	
181	18.3	51	93	0.002	White fill
182	18.66	44	86	0.002	White fill
183	18.675	46	88	0.002	White fill
184	18.72	41	83	Hairline, 0.001	
185	18.78	48	90	0.001	
186	18.91	45	87	0.004	White
187	19.02	36	78	0.001	White
188	19.1	12	54	0.001	Dark
189	19.21	42	84	0.007	White and dark fill
190	19.24	81	123	0.001	Dark fill
191	19.32	43	85	0.005	White and dark fill
192	19.38	42	84	0.001	Dark fill
193	19.44	52	94	0.001	White fill
194	19.47	64	106	0.002	White and dark fill

Appendix 8. Wyche #1 Borehole Image Log

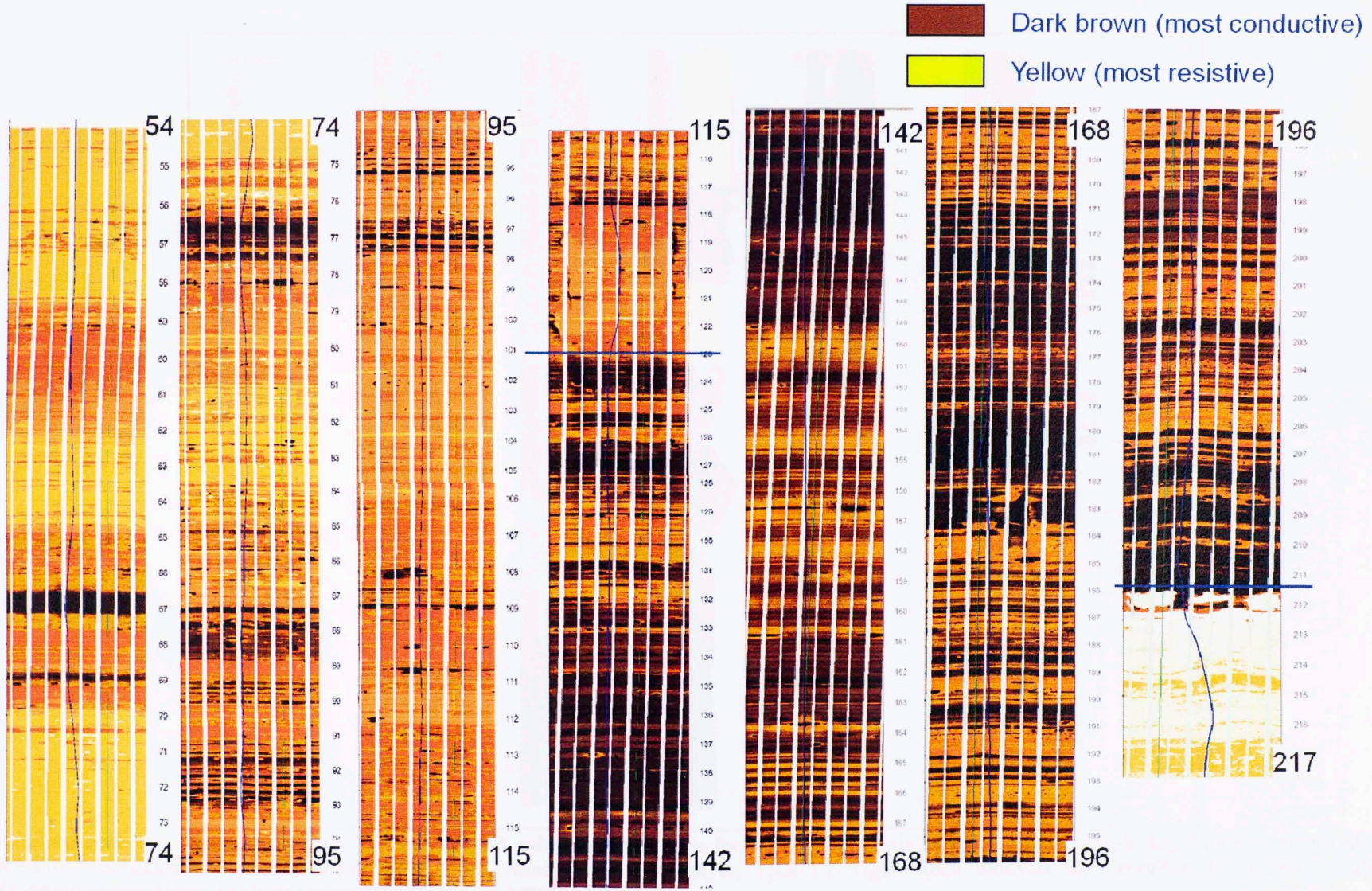

Appendix 9. Wyche #1 Core description

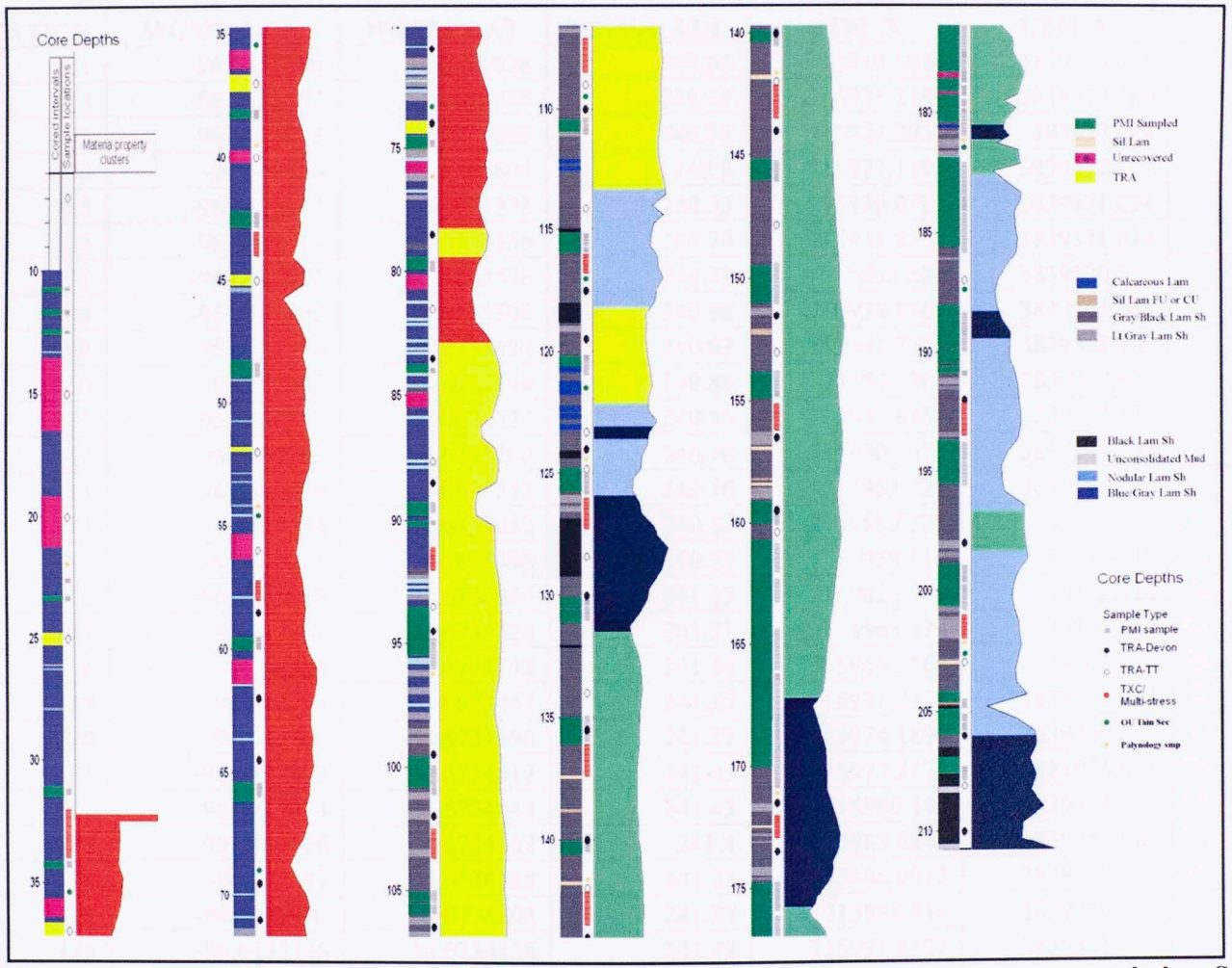

Behind-outcrop core description from Wyche #1. Left column shows core facies and right columns represents sample log. Samples removed for: PMI=PoroMechanics Lab, TRA-Devon=Tight Rock Analysis by Devon/OU, TRA-TT=Tight Rock analysis by TerraTek log cluster analysis, TXC/Multi-stress=Stress analysis (courtesy of Buckner, 2009).

Appendix 10. Locations and elevations for the 2D seismic lines

LINE	STATION	WGS84_LON	WGS84_LAT	WGS84_ALT	UTM_X	UTM_Y	Elev_ft
1	101	-96.6433696	34.6736028	240.61	715918.5036	3839374.861	782.94141
1	102	-96.6433402	34.673596	240.75	715921.2155	3839374.169	783.40075
1	103	-96.6433078	34.6735888	240.84	715924.2033	3839373.44	783.69604
1	104	-96.643276	34.6735804	240.8	715927.1393	3839372.577	783.5648
1	105	-96.6432442	34.673573	240.83	715930.0727	3839371.824	783.66323
1	106	-96.6432114	34.6735656	240.79	715933.0977	3839371.074	783.53199
1	107	-96.6431812	34.6735576	240.99	715935.886	3839370.251	784.18819
1	108	-96.6431492	34.6735506	240.98	715938.8367	3839369.543	784.15538
1	109	-96.6431174	34.6735424	240.93	715941.7721	3839368.702	783.99133
1	110	-96.643085	34.6735348	240.88	715944.761	3839367.928	783.82728
1	111	-96.6430532	34.673527	240.85	715947.6954	3839367.131	783.72885
1	112	-96.6430202	34.6735202	240.76	715950.7372	3839366.448	783.43356
1	113	-96.6429878	34.673513	240.76	715953.725	3839365.719	783.43356
1	114	-96.6429564	34.6735052	240.87	715956.6228	3839364.921	783.79447
1	115	-96.642925	34.673498	240.92	715959.519	3839364.19	783.95852
1	116	-96.6428938	34.6734904	241.05	715962.3979	3839363.414	784.38505
1	117	-96.642861	34.6734826	241.21	715965.424	3839362.619	784.91001
1	118	-96.64283	34.6734742	241.24	715968.2866	3839361.754	785.00844
1	119	-96.642798	34.673467	241.25	715971.2378	3839361.024	785.04125
1	120	-96.642766	34.6734596	241.27	715974.1896	3839360.272	785.10687
1	121	-96.6427332	34.6734512	241.43	715977.2172	3839359.41	785.63183
1	122	-96.6427014	34.6734448	241.43	715980.148	3839358.769	785.63183
1	123	-96.6426696	34.6734362	241.4	715983.0845	3839357.883	785.5334
1	124	-96.642637	34.6734288	241.32	715986.0912	3839357.132	785.27092
1	125	-96.6426062	34.6734202	241.27	715988.936	3839356.244	785.10687
1	126	-96.6425748	34.6734128	241.49	715991.8327	3839355.491	785.82869
1	127	-96.6425412	34.6734058	241.65	715994.93	3839354.786	786.35365
1	128	-96.64251	34.6733978	241.65	715997.81	3839353.966	786.35365

LINE	STATION	WGS84_LON	WGS84_LAT	WGS84_ALT	UTM_X	UTM_Y	Elev_ft
1	129	-96.6424782	34.6733892	241.64	716000.7465	3839353.08	786.32084
1	130	-96.6424454	34.6733822	241.52	716003.7705	3839352.374	785.92712
1	131	-96.6424146	34.6733754	241.38	716006.6107	3839351.686	785.46778
1	132	-96.6423822	34.6733664	241.26	716009.6032	3839350.757	785.07406
1	133	-96.642351	34.6733584	241.28	716012.4832	3839349.937	785.13968
1	134	-96.6423188	34.6733508	241.34	716015.4538	3839349.163	785.33654
1	135	-96.6422866	34.6733428	241.31	716018.4254	3839348.345	785.23811
1	136	-96.6422548	34.6733344	241.35	716021.3613	3839347.481	785.36935
1	137	-96.6422228	34.673327	241.15	716024.3131	3839346.729	784.71315
1	138	-96.642191	34.6733182	240.93	716027.2501	3839345.821	783.99133
1	139	-96.642161	34.6733104	240.88	716030.0196	3839345.02	783.82728
1	140	-96.6421278	34.673303	240.86	716033.0813	3839344.271	783.76166
2	101	-96.6432314	34.6737256	239.38	715930.8493	3839388.779	778.90578
2	102	-96.6432124	34.6737004	239.2	715932.6559	3839386.024	778.3152
2	103	-96.6431932	34.6736798	239.22	715934.4689	3839383.78	778.38082
2	104	-96.6431728	34.6736582	239.23	715936.3945	3839381.428	778.41363
2	105	-96.6431538	34.6736362	239.25	715938.1928	3839379.028	778.47925
2	106	-96.6431316	34.6736156	239.28	715940.2807	3839376.791	778.57768
2	107	-96.6431112	34.6735932	239.28	715942.2083	3839374.35	778.57768
2	108	-96.6430916	34.673572	239.26	715944.0595	3839372.041	778.51206
2	109	-96.6430708	34.6735516	239.28	715946.0186	3839369.822	778.57768
2	110	-96.643052	34.6735294	239.24	715947.7991	3839367.4	778.44644
2	111	-96.643032	34.6735048	239.25	715949.6958	3839364.714	778.47925
2	112	-96.6430124	34.6734834	239.25	715951.5476	3839362.383	778.47925
2	113	-96.6429896	34.673462	239.31	715953.6926	3839360.058	778.67611
2	114	-96.6429678	34.6734414	239.35	715955.7438	3839357.82	778.80735
2	115	-96.6429476	34.6734208	239.41	715957.6485	3839355.578	779.00421
2	116	-96.642925	34.6733988	239.46	715959.7767	3839353.186	779.16826
2	117	-96.6429054	34.6733768	239.46	715961.63	3839350.788	779.16826
2	118	-96.6428868	34.673355	239.45	715963.3911	3839348.41	779.13545
2	119	-96.642865	34.673332	239.43	715965.4486	3839345.905	779.06983

LINE	STATION	WGS84_LON	WGS84_LAT	WGS84_ALT	UTM_X	UTM_Y	Elev_ft
2	120	-96.6428472	34.6733118	239.44	715967.1323	3839343.703	779.10264
2	121	-96.6428226	34.6732874	239.45	715969.45	3839341.049	779.13545
2	122	-96.6428034	34.6732642	239.45	715971.2698	3839338.517	779.13545
2	123	-96.6427806	34.6732408	239.43	715973.42	3839335.97	779.06983
2	124	-96.6427606	34.673219	239.43	715975.3094	3839333.595	779.06983
2	125	-96.6427378	34.6731946	239.45	715977.4622	3839330.937	779.13545
2	126	-96.6427134	34.6731712	239.43	715979.759	3839328.394	779.06983
2	127	-96.642704	34.673157	242.53	715980.6573	3839326.839	779.24093
2	128	-96.6426832	34.6731374	242.68	715982.6144	3839324.71	779.73308
2	129	-96.6426602	34.6731176	242.94	715984.7735	3839322.563	780.58614
2	130	-96.642644	34.6730952	243.27	715986.3163	3839320.113	781.66887
3	94	-96.6419562	34.6719438	251.7	716052.3387	3839193.872	819.3277
3	95	-96.6419532	34.6719704	251.86	716052.5445	3839196.829	819.85266
3	96	-96.6419478	34.671997	252.33	716052.9702	3839199.791	821.39473
3	97	-96.6419426	34.6720242	252.46	716053.3761	3839202.819	821.82126
3	98	-96.641938	34.6720508	252.17	716053.7285	3839205.78	820.86977
3	99	-96.641933	34.6720788	252.07	716054.114	3839208.896	820.54167
3	100	-96.6419266	34.6721054	251.66	716054.6314	3839211.861	819.19646
3	101	-96.6419222	34.6721322	251.15	716054.9649	3839214.843	817.52315
3	102	-96.6419164	34.672159	251.09	716055.4268	3839217.828	817.32629
3	103	-96.6419122	34.6721866	250.95	716055.74	3839220.898	816.86695
3	104	-96.6419056	34.6722132	250.84	716056.2757	3839223.863	816.50604
3	105	-96.6418994	34.6722398	250.81	716056.7748	3839226.827	816.40761
3	106	-96.6418958	34.6722666	250.71	716057.035	3839229.808	816.07951
3	107	-96.6418906	34.6722938	250.57	716057.4409	3839232.836	815.62017
3	108	-96.6418848	34.6723206	250.67	716057.9028	3839235.821	815.94827
3	109	-96.6418796	34.6723484	250.7	716058.3071	3839238.916	816.0467
3	110	-96.641876	34.6723754	250.76	716058.5668	3839241.919	816.24356
3	111	-96.6418708	34.6724024	250.82	716058.9732	3839244.925	816.44042
3	112	-96.6418676	34.6724302	250.89	716059.1942	3839248.015	816.67009
3	113	-96.6418622	34.6724572	250.8	716059.6189	3839251.022	816.3748

LINE	STATION	WGS84_LON	WGS84_LAT	WGS84_ALT	UTM_X	UTM_Y	Elev_ft
3	114	-96.6418572	34.672484	250.73	716060.0075	3839254.005	816.14513
3	115	-96.6418528	34.6725118	250.64	716060.3384	3839257.098	815.84984
3	116	-96.641849	34.6725386	250.56	716060.617	3839260.079	815.58736
3	117	-96.6418442	34.672566	250.53	716060.9857	3839263.129	815.48893
3	118	-96.6418376	34.6725932	250.58	716061.5199	3839266.16	815.65298
3	119	-96.6418334	34.67262	250.46	716061.8351	3839269.142	815.25926
3	120	-96.6418286	34.6726474	250.47	716062.2038	3839272.192	815.29207
3	121	-96.6418242	34.6726744	250.46	716062.5368	3839275.196	815.25926
3	122	-96.641817	34.6727014	250.45	716063.1265	3839278.206	815.22645
3	123	-96.6418124	34.6727284	250.37	716063.4779	3839281.211	814.96397
3	124	-96.6418072	34.6727562	250.36	716063.8822	3839284.306	814.93116
3	125	-96.6418028	34.6727828	250.4	716064.2163	3839287.266	815.0624
3	126	-96.6417968	34.6728098	250.33	716064.6959	3839290.274	814.83273
3	127	-96.641791	34.6728366	250.32	716065.1578	3839293.259	814.79992
3	128	-96.641786	34.6728628	250.35	716065.5479	3839296.176	814.89835
3	129	-96.6417806	34.6728894	250.27	716065.9737	3839299.138	814.63587
3	130	-96.6417764	34.6729184	250.26	716066.2832	3839302.364	814.60306
3	131	-96.6417712	34.6729454	250.21	716066.6896	3839305.37	814.43901
3	132	-96.6417674	34.6729722	250.2	716066.9682	3839308.351	814.4062
3	133	-96.6417628	34.6729994	250.11	716067.319	3839311.378	814.11091
3	134	-96.6417566	34.6730254	250.12	716067.8196	3839314.275	814.14372
3	135	-96.6417522	34.673054	250.16	716068.1485	3839317.457	814.27496
3	136	-96.641748	34.6730806	250.11	716068.4643	3839320.417	814.11091
3	137	-96.6417426	34.6731078	250.13	716068.8885	3839323.445	814.17653
3	138	-96.6417368	34.6731348	250.13	716069.3498	3839326.453	814.17653
3	139	-96.6417314	34.6731618	250.04	716069.7745	3839329.459	813.88124
3	140	-96.6417272	34.6731898	250.05	716070.0866	3839332.574	813.91405
3	141	-96.6417222	34.6732174	250.05	716070.4731	3839335.646	813.91405
3	142	-96.6417148	34.6732436	250.1	716071.0831	3839338.569	814.0781
4	84	-96.6441516	34.6738116	255.2	715846.299	3839396.344	830.8112
4	85	-96.6441176	34.673816	255.28	715849.4033	3839396.905	831.07368

LINE	STATION	WGS84_LON	WGS84_LAT	WGS84_ALT	UTM_X	UTM_Y	Elev_ft
4	86	-96.6440844	34.6738206	255.3	715852.4338	3839397.486	831.1393
4	87	-96.6440518	34.6738244	255.17	715855.4114	3839397.978	830.71277
4	88	-96.6440188	34.6738282	255.13	715858.4257	3839398.47	830.58153
4	89	-96.6439852	34.6738328	255.09	715861.4928	3839399.052	830.45029
4	90	-96.6439534	34.6738366	254.95	715864.3971	3839399.542	829.99095
4	91	-96.6439218	34.6738402	254.95	715867.2836	3839400.009	829.99095
4	92	-96.6438874	34.6738448	254.89	715870.424	3839400.593	829.79409
4	93	-96.6438544	34.6738486	254.88	715873.4383	3839401.086	829.76128
4	94	-96.6438216	34.6738528	254.92	715876.4332	3839401.622	829.89252
4	95	-96.6437882	34.6738554	254.91	715879.4872	3839401.982	829.85971
4	96	-96.643757	34.6738596	254.92	715882.3354	3839402.515	829.89252
4	97	-96.6437238	34.673864	255.01	715885.3665	3839403.074	830.18781
4	98	-96.643688	34.6738414	254.98	715888.7058	3839400.644	830.08938
4	99	-96.6436522	34.6738384	254.68	715891.9943	3839400.388	829.10508
4	100	-96.6436168	34.6738442	254.75	715895.2233	3839401.107	829.33475
4	101	-96.643591	34.6738808	254.81	715897.4926	3839405.222	829.53161
4	102	-96.6435594	34.6738838	254.7	715900.3806	3839405.623	829.1707
4	103	-96.6435266	34.673887	254.65	715903.3781	3839406.048	829.00665
4	104	-96.6434934	34.6738916	254.63	715906.4086	3839406.63	828.94103
4	105	-96.6434626	34.673895	254.58	715909.2223	3839407.073	828.77698
4	106	-96.64343	34.6738992	254.57	715912.1988	3839407.609	828.74417
4	107	-96.6433958	34.6739052	254.39	715915.3173	3839408.348	828.15359
4	108	-96.6433644	34.673908	254.33	715918.1875	3839408.726	827.95673
4	109	-96.6433298	34.6739114	254.33	715921.3494	3839409.177	827.95673
4	110	-96.6432976	34.6739162	254.2	715924.2878	3839409.779	827.5302
4	111	-96.6432644	34.6739206	254.07	715927.3188	3839410.338	827.10367
4	112	-96.6432316	34.6739248	253.96	715930.3136	3839410.874	826.74276
4	113	-96.643198	34.6739304	253.88	715933.3782	3839411.567	826.48028
4	114	-96.6431656	34.6739344	253.88	715936.3369	3839412.081	826.48028
4	115	-96.6431324	34.6739388	253.81	715939.3679	3839412.64	826.25061
4	116	-96.6430988	34.6739434	253.74	715942.4351	3839413.222	826.02094

LINE	STATION	WGS84_LON	WGS84_LAT	WGS84_ALT	UTM_X	UTM_Y	Elev_ft
4	117	-96.6430684	34.6739482	253.64	715945.2085	3839413.82	825.69284
4	118	-96.643035	34.6739528	253.51	715948.2573	3839414.402	825.26631
4	119	-96.6430014	34.6739578	253.47	715951.3234	3839415.029	825.13507
4	120	-96.6429686	34.6739616	253.38	715954.3193	3839415.52	824.83978
4	121	-96.6429352	34.6739648	253.3	715957.3718	3839415.947	824.5773
4	122	-96.6429032	34.6739688	253.23	715960.2938	3839416.459	824.34763
4	123	-96.6428708	34.6739728	253.16	715963.2526	3839416.973	824.11796
4	124	-96.6428376	34.6739772	253.04	715966.2836	3839417.532	823.72424
4	125	-96.6428054	34.6739816	252.89	715969.2229	3839418.089	823.23209
4	126	-96.6427728	34.6739852	252.89	715972.201	3839418.558	823.23209
4	127	-96.6427402	34.6739902	252.76	715975.1755	3839419.183	822.80556
4	128	-96.6427064	34.6739948	252.87	715978.261	3839419.766	823.16647
4	129	-96.6426744	34.6739986	253.01	715981.1836	3839420.256	823.62581
4	130	-96.6426414	34.6740034	253.06	715984.1952	3839420.859	823.78986
4	131	-96.6426086	34.6740082	253	715987.1885	3839421.462	823.593
4	132	-96.6425752	34.6740124	253.02	715990.2384	3839422	823.65862
4	133	-96.6425426	34.6740158	252.96	715993.217	3839422.447	823.46176
4	134	-96.64251	34.6740208	252.86	715996.1915	3839423.071	823.13366
4	135	-96.6424768	34.6740246	252.85	715999.224	3839423.564	823.10085
4	136	-96.642444	34.6740294	253	716002.2173	3839424.167	823.593
4	137	-96.6424116	34.6740332	252.95	716005.1766	3839424.658	823.42895
4	138	-96.6423788	34.6740368	252.9	716008.173	3839425.128	823.2649
4	139	-96.642345	34.6740414	252.89	716011.2585	3839425.711	823.23209
4	140	-96.6423132	34.674046	252.84	716014.1607	3839426.289	823.06804
4	141	-96.6422796	34.6740494	252.93	716017.2309	3839426.738	823.36333
4	142	-96.6422472	34.6740522	253	716020.1928	3839427.118	823.593
4	143	-96.6422134	34.6740566	253.03	716023.2788	3839427.679	823.69143
4	144	-96.6421812	34.6740602	252.91	716026.2202	3839428.147	823.29771
4	145	-96.6421486	34.6740638	252.88	716029.1983	3839428.617	823.19928
4	146	-96.6421158	34.674069	252.99	716032.1906	3839429.264	823.56019
4	147	-96.6420824	34.6740722	252.99	716035.243	3839429.691	823.56019

LINE	STATION	WGS84_LON	WGS84_LAT	WGS84_ALT	UTM_X	UTM_Y	Elev_ft
4	148	-96.6420502	34.6740766	253.03	716038.1824	3839430.248	823.69143
4	149	-96.642017	34.6740814	253.01	716041.2123	3839430.852	823.62581
4	150	-96.6419842	34.6740864	252.92	716044.2051	3839431.477	823.33052
4	151	-96.6419516	34.674091	252.92	716047.1806	3839432.057	823.33052
4	152	-96.6419188	34.674095	252.94	716050.176	3839432.571	823.39614
4	153	-96.6418862	34.6740994	252.88	716053.152	3839433.129	823.19928
4	154	-96.6418534	34.6741028	252.84	716056.149	3839433.577	823.06804
4	155	-96.64182	34.6741072	252.82	716059.1983	3839434.136	823.00242
4	156	-96.6417878	34.6741114	252.73	716062.1382	3839434.671	822.70713
4	157	-96.6417552	34.6741158	252.71	716065.1142	3839435.229	822.64151
4	158	-96.641723	34.6741198	252.7	716068.0546	3839435.742	822.6087
4	159	-96.6416878	34.6741246	252.66	716071.2678	3839436.35	822.47746
4	160	-96.6416552	34.6741286	252.64	716074.2449	3839436.864	822.41184
4	161	-96.6416228	34.6741322	252.6	716077.2046	3839437.333	822.2806
4	162	-96.6415912	34.6741368	252.51	716080.0885	3839437.911	821.98531
4	163	-96.6415586	34.6741402	252.46	716083.0671	3839438.358	821.82126
4	164	-96.6415244	34.6741442	252.46	716086.1908	3839438.875	821.82126
4	165	-96.641493	34.674148	252.38	716089.0584	3839439.364	821.55878
4	166	-96.641459	34.6741524	252.33	716092.1627	3839439.925	821.39473
4	167	-96.6414256	34.674157	252.33	716095.2115	3839440.507	821.39473
4	168	-96.6413924	34.6741612	252.25	716098.243	3839441.044	821.13225
5	81	-96.639612	34.671433	256.69	716268.4944	3839142.247	835.69989
5	82	-96.6396144	34.671459	256.66	716268.2068	3839145.126	835.60146
5	83	-96.6396128	34.671487	256.79	716268.2806	3839148.235	836.02799
5	84	-96.6396082	34.6715136	256.88	716268.633	3839151.196	836.32328
5	85	-96.6396086	34.6715422	256.98	716268.5219	3839154.367	836.65138
5	86	-96.6396044	34.6715692	256.93	716268.8366	3839157.371	836.48733
5	87	-96.6396024	34.6715964	256.92	716268.9492	3839160.393	836.45452
5	88	-96.6395996	34.6716232	257.06	716269.136	3839163.371	836.91386
5	89	-96.639597	34.6716514	257.14	716269.301	3839166.505	837.17634
5	90	-96.6395956	34.6716786	257.19	716269.3585	3839169.525	837.34039

LINE	STATION	WGS84_LON	WGS84_LAT	WGS84_ALT	UTM_X	UTM_Y	Elev_ft
5	91	-96.6395924	34.671706	257.24	716269.5805	3839172.571	837.50444
5	92	-96.6395912	34.6717328	257.4	716269.6208	3839175.547	838.0294
5	93	-96.6395884	34.6717596	257.6	716269.8077	3839178.525	838.6856
5	94	-96.639585	34.6717874	257.41	716270.0469	3839181.616	838.06221
5	95	-96.6395834	34.671815	257.63	716270.1218	3839184.681	838.78403
5	96	-96.639581	34.6718418	257.69	716270.272	3839187.659	838.98089
5	97	-96.639579	34.6718694	257.82	716270.3835	3839190.725	839.40742
5	98	-96.6395768	34.6718964	257.83	716270.5149	3839193.725	839.44023
5	99	-96.6395746	34.6719244	257.91	716270.6437	3839196.835	839.70271
5	100	-96.6395714	34.6719524	258.02	716270.8641	3839199.948	840.06362
5	101	-96.6395688	34.6719796	258.13	716271.0316	3839202.971	840.42453
5	102	-96.6395674	34.6720076	258.23	716271.0871	3839206.08	840.75263
5	103	-96.6395654	34.6720344	258.26	716271.2006	3839209.057	840.85106
5	104	-96.639562	34.6720612	258.3	716271.4425	3839212.037	840.9823
5	105	-96.6395614	34.6720892	258.39	716271.4247	3839215.144	841.27759
5	106	-96.639559	34.672117	258.51	716271.5723	3839218.233	841.67131
5	107	-96.6395572	34.672145	258.51	716271.6644	3839221.342	841.67131
5	108	-96.6395554	34.6721718	258.6	716271.7597	3839224.319	841.9666
5	109	-96.6395534	34.6721988	258.7	716271.8727	3839227.318	842.2947
5	110	-96.639551	34.672226	258.78	716272.0219	3839230.341	842.55718
5	111	-96.6395484	34.6722538	258.81	716272.1879	3839233.43	842.65561
5	112	-96.6395464	34.6722808	258.95	716272.3009	3839236.429	843.11495
5	113	-96.6395468	34.6723092	259.04	716272.1904	3839239.578	843.41024
5	114	-96.6395446	34.672336	259.11	716272.3223	3839242.556	843.63991
5	115	-96.639542	34.6723634	259.16	716272.4893	3839245.601	843.80396
5	116	-96.6395406	34.6723904	259.28	716272.5473	3839248.599	844.19768
5	117	-96.639538	34.6724186	259.44	716272.7123	3839251.732	844.72264
5	118	-96.6395366	34.6724458	259.54	716272.7698	3839254.752	845.05074
5	119	-96.639534	34.6724736	259.6	716272.9358	3839257.842	845.2476
5	120	-96.6395324	34.6724998	259.54	716273.0142	3839260.751	845.05074
5	121	-96.6395292	34.6725274	259.66	716273.2357	3839263.82	845.44446

LINE	STATION	WGS84_LON	WGS84_LAT	WGS84_ALT	UTM_X	UTM_Y	Elev_ft
5	122	-96.6395272	34.6725546	259.65	716273.3482	3839266.841	845.41165
5	123	-96.6395244	34.6725828	259.68	716273.5315	3839269.975	845.51008
5	124	-96.6395224	34.67261	259.66	716273.644	3839272.997	845.44446
5	125	-96.6395194	34.6726368	259.66	716273.8492	3839275.976	845.44446
5	126	-96.6395202	34.6726646	259.71	716273.7036	3839279.058	845.60851
5	127	-96.6395168	34.672691	259.6	716273.9465	3839281.994	845.2476
5	128	-96.6395152	34.6727194	259.63	716274.0192	3839285.147	845.34603
5	129	-96.6395128	34.6727462	259.18	716274.1695	3839288.125	843.86958
5	130	-96.6395136	34.672774	259.25	716274.0238	3839291.207	842.09925
5	131	-96.639522	34.6728014	258.37	716273.1828	3839294.228	841.21197
5	132	-96.6395208	34.6728296	258.13	716273.2194	3839297.359	840.42453
5	133	-96.6395186	34.6728574	257.92	716273.3487	3839300.447	839.73552
5	134	-96.6395168	34.6728844	257.71	716273.4434	3839303.446	839.04651
5	135	-96.6395144	34.6729116	257.44	716273.5926	3839306.468	838.16064
5	136	-96.639511	34.672939	257.19	716273.8329	3839309.515	837.34039
5	137	-96.6395104	34.6729654	256.98	716273.8192	3839312.445	836.65138
5	138	-96.6395072	34.6729926	256.76	716274.0417	3839315.469	835.92956
5	139	-96.639505	34.6730196	256.64	716274.1731	3839318.468	835.53584
5	140	-96.6395006	34.6730484	256.46	716274.5014	3839321.672	834.94526
5	141	-96.6394978	34.6730754	256.28	716274.6877	3839324.673	834.35468
5	142	-96.639496	34.6731018	256.04	716274.784	3839327.606	833.56724
5	143	-96.6394934	34.6731292	255.86	716274.951	3839330.651	832.97666
5	144	-96.6394902	34.6731568	255.73	716275.1725	3839333.719	832.55013
5	145	-96.6394886	34.6731844	255.5	716275.2473	3839336.784	831.7955
5	146	-96.639486	34.6732114	255.27	716275.4153	3839339.784	831.04087
5	147	-96.639486	34.6732392	255.12	716275.343	3839342.868	830.54872
5	148	-96.6394834	34.6732666	254.9	716275.51	3839345.913	829.8269
5	149	-96.6394816	34.673294	254.77	716275.6037	3839348.956	829.40037
5	150	-96.6394792	34.673321	254.63	716275.7534	3839351.956	828.94103
5	151	-96.6394762	34.6733494	254.48	716275.9544	3839355.113	828.44888
5	152	-96.6394744	34.6733774	254.29	716276.0465	3839358.223	827.82549

LINE	STATION	WGS84_LON	WGS84_LAT	WGS84_ALT	UTM_X	UTM_Y	Elev_ft
5	153	-96.6394724	34.6734054	254.13	716276.157	3839361.333	827.30053
5	154	-96.6394676	34.6734314	253.95	716276.5292	3839364.227	826.70995
5	155	-96.6394654	34.6734586	253.72	716276.6601	3839367.249	825.95532
5	156	-96.639464	34.6734866	253.58	716276.7155	3839370.358	825.49598
5	157	-96.6394612	34.6735134	253.4	716276.9024	3839373.337	824.9054
5	158	-96.6394586	34.6735404	253.13	716277.0704	3839376.337	824.01953
5	159	-96.6394566	34.673568	252.89	716277.1819	3839379.403	823.23209
5	160	-96.639454	34.6735954	252.69	716277.3489	3839382.448	822.57589
5	161	-96.6394526	34.6736226	252.45	716277.4065	3839385.468	821.78845
5	162	-96.6394502	34.6736494	252.23	716277.5567	3839388.446	821.06663
5	163	-96.639448	34.6736778	252.02	716277.6844	3839391.601	820.37762
5	164	-96.6394448	34.673705	251.82	716277.9069	3839394.625	819.72142
5	165	-96.6394436	34.6737322	251.6	716277.9461	3839397.645	818.9996
5	166	-96.6394414	34.6737592	251.47	716278.0775	3839400.644	818.57307
5	167	-96.6394386	34.6737868	251.24	716278.2623	3839403.712	817.81844
5	168	-96.6394374	34.6738136	251	716278.3025	3839406.687	817.031

Appendix 11. Number of fractures from scan lines grouped in 15° strike intervals (n=357).

Strike (°)	Strike direction	Group	Number of Fractures	Percentage (%)
76-90	ENE-WSW	1	91	26
31-45	NE-SW	2	55	15
106-120	NW-SE	2	44	12
91-105	WNW-ESE	1	42	11

Appendix 12. Number of fractures from scan lines grouped in 15° strike intervals (n=357) and classified depending on their apertures

Class	Strike (°)	Strike direction	Group	Number of Fractures	Percentage (%)
No Aperture (n=214)	76-90	ENE-WSW	1	38	18
	31-45	NE-SW	2	36	17
	106-120	NW-SE	2	33	15
	91-105	WNW-ESE	1	28	13
Open Aperture (n=72)	76-90	ENE-WSW	1	27	38
	91-105	WNW-ESE	2	22	31
	31-45	NE-SW	1	20	28
	61-75	NE-SW		9	13
Filled Aperture (n=71)	76-90	ENE-WSW	1	27	38
	91-105	WNW-ESE	1	10	14
	61-75	NE-SW		10	14
	31-45	NE-SW	2	8	11

Appendix 13. Number of fractures picked manually using software B grouped in 15° strike intervals (n=131).

Strike (°)	Strike direction	Group	Number of Fractures	Percentage (%)
76-90	ENE-WSW	1	63	48
91-105	WNW-ESE	1	19	15
31-45	NE-SW	2	10	8
16-30	NNE	-	8	6

Appendix 14. Number of fractures picked automatically by software A grouped in 15° strike intervals (n=5008).

Strike (°)	Group	Number of Fractures	Percentage (%)
31-45	2	631	13
76-90	1	624	12
46-60		606	12
61-75		571	11
16-30		484	10
91-105	1	450	9
0-15		360	7
106-120	2	345	7
121-135		279	6
166-180		266	5
151-165		196	4
136-150		196	4

Appendix 15. Number of fractures picked automatically by software A with dips between 76-90° grouped in 15° strike intervals (n=280).

Strike (°)	Strike direction	Group	Number of Fractures	Percentage (%)
76-90	**ENE-WSW**	**1**	**78**	**28**
31-45	**NE-SW**	**2**	**48**	**17**
46-60	**NE-SW**		**37**	**13**
61-75	**NE-SW**		**36**	**13**
16-30	**NNE-SSW**		**24**	**9**
91-105	**WNW-ESE**	**1**	**24**	**9**

Appendix 16. Number of fractures picked automatically by software A with dips between 76-90° and roughness between 0.8-1, grouped in 15° strike intervals (n=93).

Strike (°)	Strike direction	Group	Number of Fractures	Percentage (%)
76-90	ENE-WSW	1	18	
31-45	NE-SW	2	18	
61-75			15	

This volume is the property of the University of Oklahoma, but the literary rights of the author are a separate property and must be respected. Passages must not be copied or closely paraphrased without the previous written consent of the author. If the reader obtains any assistance from this volume, he must give proper credit in his own work.

I grant the University of Oklahoma Libraries permission to make a copy of my thesis upon the request of individuals or libraries. This permission is granted with the understanding that a copy will be provided for research purposes only, and that requestors will be informed of these restrictions.

[redacted]

A library which borrows this thesis for use by its patrons is expected to secure the signature of each user.

This thesis by ROMINA MARISA PORTAS ARROYAL has been used by the following persons, whose signatures attest their acceptance of the above restrictions.

NAME AND ADDRESS DATE